Application of fluorescence light microscopy with structured illumination techniques to cell inflammatory responses

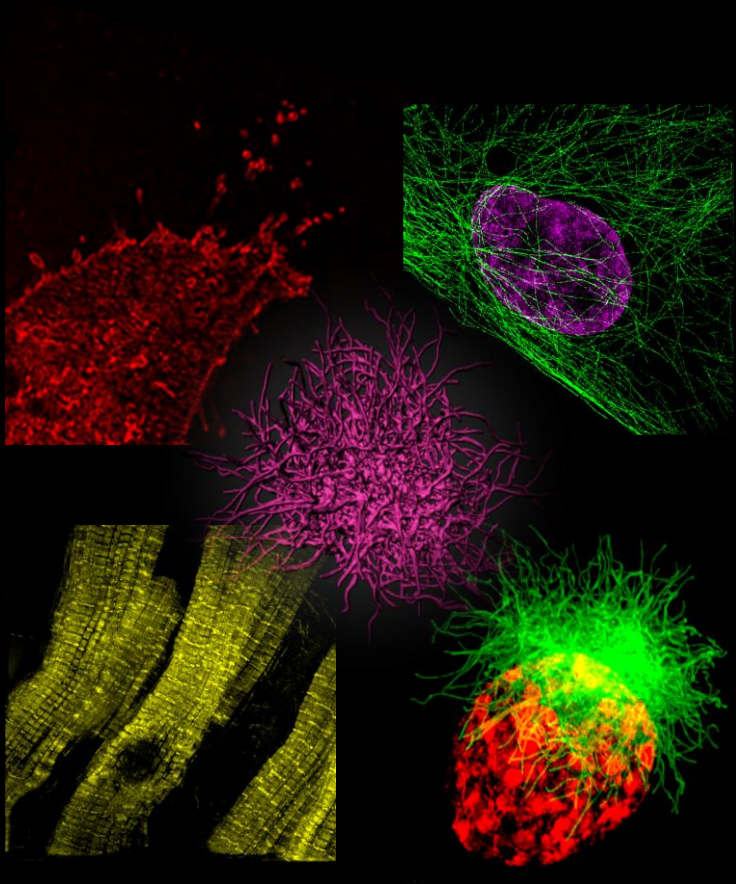

Gabriel Tung-Cheng Wang

Dissertation

Application of fluorescence light microscopy with structured illumination techniques to cell inflammatory responses

Gabriel Tung-Cheng Wang

December 2019

Biomolecular Photonics
Department of Physics
Bielefeld University

Printed on non-aging paper (ISO 9706)

Reviewers:
Prof. Dr. Thomas Huser
Prof. Dr. Francesco Peri

Summary

Advanced far-field fluorescence microscopy techniques are novel and very promising tools for live-cell imaging and the non-invasive observation of biological features in the life science researches[98][107][66]. In this work, different microscopy techniques are used to study each aspect of the cell inflammatory responses induced by bacterial endotoxins, i.e. lipopolysaccharides (LPS). The released LPS as potent pathogens are recognized by Toll-like receptor 4 (TLR4) and the co-receptors such as CD14 and MD-2 as part of our innate immune defense system [110][130][131][4]. The first contact of LPS with the cell surface is visualized under single-molecule detection using TIRF illumination and the tracing of individual fluorescent LPS molecules reveals the dynamic motion of the bound molecules as well as the transient fusion with other LPS particles. This tracked event may imply the dimerization of TLR4s after LPS was presented by CD-14 to MD-2 during the formation of a functional TLR4 receptor complex. Once the signaling complex is formed, it is internalized via the CD14-mediated endocytosis and detected in the early endosomes by SR-SIM imaging which enables the visualization of earliest vesicle formation in the vicinity of the plasma membrane. With the multiplexed colors of the organelle-specific labels, the deconvolved images show that the internalized LPS/LOS is transported en route to lysosomes where the detoxification process takes place.

The labeling technique is also key to the successful application of fluorescence microscopy. Although the fluorescently labeled LPS is commercially available, however, only one method has been proposed to efficiently perform the conjugation to LPS[137], whereas the labeling for LOS is largely unknown. Since the structural variants of LPS are already known to have different immune reactivities for cells[160][74], it is necessary to address other short forms of endotoxins such as lipooligosaccharide (LOS) and lipid A and their physiological differences to LPS. Together with the collaborators, I have thus reported the first fluorescent LOS conjugated to a near-IR organic dye, Cy7N, used in live-cell imaging on the confocal microscope[147]. The binding and cell response to LOS-Cy7N follows the same principle of LPS-induced cell activation. However, the fast internalization of the fluorescent LOS indicates that a biased signaling may exist and exerts distinct endosomal signaling far from the conventional concept established for LPS. On the other hand, small constructs from the lipid A moiety recognized by cell receptors may either block the TLR4 signaling or trigger only mild immune reactivity

and thus create potential interest of pharmaceutical use as adjuvants in vaccine development.

The transduction of receptor signaling leads to the expression of inflammation genes and starts up the second phase of LPS-induced cell responses, i.e. the generation of inflammasomes[123][70][67]. These are formed by the assembly of ASC adaptor proteins into a supramolecular complex which serves as the inflammatory cytokine production site. The development of an ASC speck was investigated by structured illumination microscopy in three dimensions (3D-SIM), which revealed the growth process of the ASC polymer into filamentous structures. Single-filament resolution was also achieved in the single-molecule localization microscopy. The application of 3D-SIM to inflammasome formation truly shows its advantage for live-cell imaging, by which the dynamic visualization of the ASC-GFP speck formation such as the elongation, branching and cross-linking of filaments were first reported in this study. To further elucidate the mechanism of the filament formation, the truncated form of ASC was used to observe the aberration of inflammasome architecture which suggests that the missing domain is crucial for cross-linking of the ASC filaments and forms the skeletal network to stabilize the speck structures.

In chapter 1 of this dissertation, I first give a brief introduction of light microscopy techniques and the underlying working principles. Special emphasis is put on superresolution microscopy, especially on the SR-SIM methodology which is heavily used in my work. The study of endotoxin-related innate immunity begins to unfold from chapter 2 on, in which the LPS/LOS/lipid A were exploited with various microscopy techniques as mentioned above, followed by the super-resolved inflammasome structure and its filament analysis in chapter 3. The application of SR-SIM should not be stopped only at the single-cell range, it is thus extended to the image acquisitions of cleared tissues and the large-scale cell sheet with multiple color labeling shown in chapter 4. Lastly, the information about the microscopic setup and materials used is provided in the appendices.

Contents

CONTENTS

Chapter 1

Theory of optical microscopy

1.1 Image formation and resolution limit

Visualization is athe most important ability among the five senses on which we rely to receive information from the outer world and interact with surroundings. Light is needed to form an image of the object in our eyes, but the quality of the image is at the same time compromised by its nature, the light diffraction, which also limits the extent to discriminate the constituent parts of the object in the image. Hence the image contrast is confounded and the resolution is limited[43][143].

Christiaan Huygens (1629-1695) invented the idea of infinite numbers of the spherical wavelets on the wavefront to describe how the light ray bends (refraction). Later on Fresnel (1788-1827) further extended this concept to explain the diffraction of light by calculating the amplitude and phases of all secondary wavelets as they propagate in a given time and interfere with each other to form the second wavefront. By doing so, he was able to display the light distribution of the diffraction patterns, thus established the theory of light diffraction. Fraunhofer (1787-1826) and Kirchhoff (1824-1887) provided mathematical formulations for the diffraction model used in nowadays optics. The collection of these studies give us the diffraction theory of light which is crucial to understand the image formation and the resolution limit[18].

The fundamental limit of optical resolution originates from the finite diameter of the imaging lens which causes the light diffracted and results in a point being imaged as a diffraction pattern of the system's aperture (Figure 1.1A). This unfaithful translation causes a point emitter to be imaged as a spread-out spot and its size is diffraction limited. The resulting intensity distribution of the spot is called point spread function (PSF), and if the circular apertures or lenses are used in the optical system, the detected image is essentially an Airy disc with concentric rings[3] (Figure 1.1B). Consider if two emitters of light are physically close to each other in an extent that their PSFs are partially overlapped in the image plane, but can still be discriminated as two identities, the distance between them is defined as the optical resolution. One can easily understand that the two-point distance is intrinsically determined by the PSF size, i.e. the sharper the PSFs are, the shorter distance can be reached. Lord Rayleigh (1896) defined the resolution criterion as the two points which are just resolved when the peak of the first Airy disk coincides with the first minimum of the other[105] (Figure 1.1C). In other words the smallest resolvable distance of two PSFs is the radius of an Airy disk, which is expressed when the two point objects are separated by the angle

$$\theta = \frac{1.22\lambda}{D}$$

where λ is the wavelength of the light, and D is the diameter of the aperture. It is reformulated after the introduction of numerical aperture (NA) in the modern form:

$$d_{xy} = \frac{0.61\lambda}{NA}$$

where NA= n·sinθ, n is the refraction index of the medium between the object and the microscope objective, θ is the half angel of the light cone that enters the objective (Figure 1.1A). As with lateral resolution, the axial resolution limit is approximated as

$$d_z = \frac{2\lambda}{NA^2}$$

Rayleigh criterion is widely accepted today, although the measure is rather subjective to human eyes. Other approaches such as Sparrow criterion $d_{xy} = \frac{0.47\lambda}{NA}$ is more often used in astronomy[127]. But the greatest benefit of Rayleigh's criterion is that he transformed the two-point resolution established by the visual interpretation into a single PSF measurement. However, the position of the first dark ring is not always easy to find and determine the radius of a PSF in the presence of

noises. Therefore, in practice the resolution of an imaging system is normally assessed by using the Gaussian function fitted to the central part of a PSF and its full-width-half-maximum (FWHM), which matches well to the Rayleigh criterion, is taken as the estimation of the resolving power of the microscopes (Figure 1.1C).

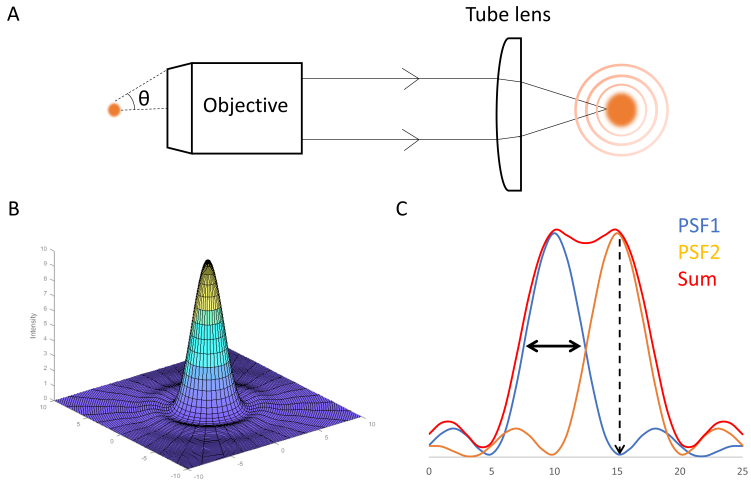

Figure 1.1: (A) Light diffraction causes a point emitter being imaged as an Airy disk pattern. In Huygens' wavelets theory, if more wavelets of greater incident angles θ are involved in the interference as light propagates to the image plane, a smaller or sharper PSF will be formed, hence the higher resolution. (B) The intensity profile of a simulated Airy disk. Courtesy of Dr. Cihang Kong. (C) Two PSFs are plotted in the distance that meets the Rayleigh's criterion, in which the peak of PSF2 falls on the first zero of the PSF1 (dashed arrow). The overlay intensity of two PSFs is also shown. A double-head arrow depicts FWHM of the PSF1, which serves as a resolution measure of the optical system.

Besides the PSF measurement, the resolving power of the microscopes is revolutionarily defined by Ernst Abbe (1840-1905), who introduced the concept of numerical aperture of the optical lenses we use in the modern microscopes[1]. Numerical aperture is a dimensionless number that quantifies the ability of an objective to capture light. Abbe first considered the object as a grid of periodic stripes which have certain frequencies. If the purpose of the microscope objective is to form an image from the diffraction pattern produced by the object, the aperture of the objective is a spatial filter to allow the maximal frequency of diffraction order entering into the objective and form the image at the focal plane. As the aperture of the objective is widened, more diffraction orders enter the microscope objective, the more details and sharper contrast that can be observed in the image

of higher resolution. The numerical aperture (NA) is an invented resolution index in analogy to the physical aperture, which virtually represents the resolving power of an objective (Figure 1.2).

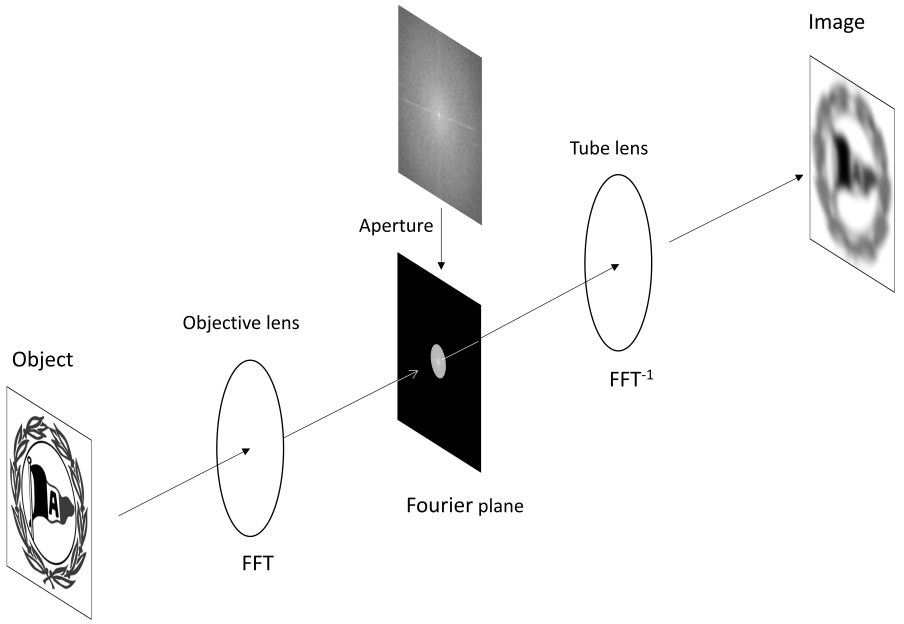

Figure 1.2: Spatial filtering: The image formation through optics can be interpreted in Fourier transform. An object of Arminia Bielefeld logo is re-imaged by fast Fourier transformed (FFT) into the Fourier plane where the high frequency components are blocked by the back aperture of the objective. Therefore, fine details and sharpness of the final image are lost after inverse FFT. The NA of an objective works conceptually as a spatial filter and determines the optical resolution.

Abbe calculated the resolution limit for incoherent emitted light as

$$d = \frac{\lambda}{2NA}$$

where d is the smallest line-to-line distance, other parameters are the same as described above. Abbe also stated clearly that light diffraction limits the resolution of an optical system at approximately 200nm, which is known as Abbe limit (1873)[1]. We can either by reducing the wavelength or by increasing the numerical aperture to get microscopic resolution improvement.

An alternative criterion to define the resolution limit is to analyze the images in the frequency domain by Fourier transformation (Figure 1.2). If an image is the superposition of a series of sine or cosine waves which have certain frequency, amplitude and phases, it can be expressed as the combination of frequency components in the same way as the rays of different diffraction orders were used in Abbe's theory. Duffieux (1891-1976) introduced Fourier transformation techniques into optics, by which the imaging capability of the microscopes is described as optical transfer function (OTF). The OTF is in fact the Fourier transformation of the PSF[150]. The resolution limit is set at where the OTF drops to zero which indicates the end of the frequency support of the microscope. This defines the resolving power in real space by back transformation of this frequency limit. But it should be noted that there is no absolute zero in practice as the end frequency is always polluted with noises which are visible after the Fourier transformation as high frequency content. Therefore, the real information needs to be isolated from the noises by certain threshold. Banterle et al.,[10] and Niewhuizen et al.,[91] introduced Fourier ring correlation (FRC) to measure the effective resolution of the acquired images in superresolution imaging. It applies to the localization microscopy in which the objects are serially imaged and the image stack is split into two parts for FRC analysis, assuming the same structure from two reconstructed images has correlation close to 1, while the Poisson-distributed noises lead to decreasing value of the correlation which reaches to the applied threshold criteria that define the achievable resolution.

1.2 Fluorescence and labeling

1.2.1 Principle of fluorescence

Fluorescence is one of the luminescence processes in which the light emanates from the excited fluorophores. A fluorescent molecule is excited upon the absorption of a photon that brings it from the ground state to a higher energy state of electronic transition in the quantised manner (Figure 1.3A). The exited molecule may loose some energy through non-radiative processes such as heat dissipation while it relaxes to the lowest vibrational level of the excited states. But shortly, in nanosecond range, the excited molecule returns to the ground state and releases the energy as the fluorescence photons. The energy of an emitted photon matches

to the energy difference between two transitional states (S1-S0). Since part of the excitation energy is lost in the form of vibration or heat dissipation, the emitted photon now has the energy less than what the molecule previously absorbed. In accordance with Plank's law of energy,

$$E = hf = \frac{hc}{\lambda}$$

where h is Plank constant, f and λ are the frequency and wavelength of the emitted photon, a fluorescent photon carrying the lower energy has thus a longer wavelength compared with the excitation one, a phenomenon known as Stokes shift. Although the energy gaps between each states are discrete, the transition can occur among different vibrational levels, leading to the distinct distributions of excitation and emission spectra (Figure 1.3B). The excited electron normally favors via the spontaneous emission to decay back to the ground state, but it is possible to be transferred through intersystem crossing to a triplet state or other dark states. In these "off states" the molecule may linger in micro-to mili-second range before it returns to the ground state and emits phosphorescent photons[141][66].

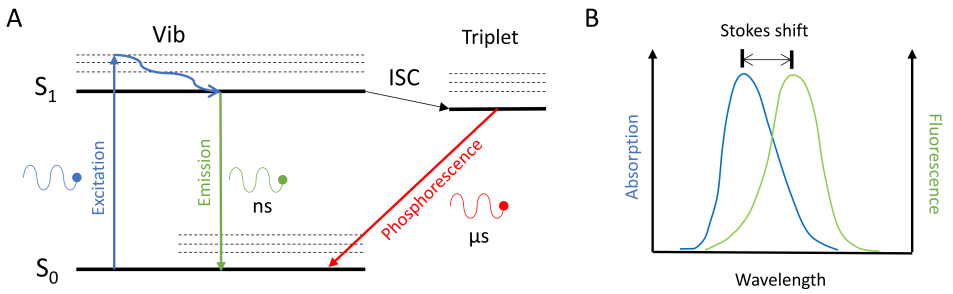

Figure 1.3: (A) A Jablonski diagram illustrates the basics of fluorescence. In this quantum mechanical system different states are drawn in the horizontal lines. They are composed of electronic states (solid lines) and vibrational/rotational states (dash lines). Each of them has different energy level plotted in the vertical axis. The bigger distance between two levels means greater energy differences. The fluorescence process begins from the absorption of a photon that carries the energy matching to the gaps between the ground state (S0) and one of the vibrational levels of excitation state (S1). The excited molecule quickly relaxes within vibration states before it returns back to S0 and releases a photon in the time span of nanoseconds. Although it's not favorable, the excited molecule can enter into triplet excited state where it stays up to miliseonds prior to the phosphorescence emission.(B) Absorption and emission spectra are schematically represented and the wavelength difference between the two corresponds to the Stokes shift.

1.2.2 Fluorophores and labeling techniques

In fluorescence microscopy fluorescent molecules typically emit light in the visible to near-infrared spectrum (400-800nm) and they are mainly composed of two types of origins: synthetic organic dyes and fluorescent proteins. The former are rhodamines (e.g. AlexaFluor), carbocyanines (e.g. Cy3/5/7), oxazines (e.g. ATTO 655) and carbopyronines (e.g.ATTO 647N). They are usually conjugated on the antibodies which have specific binding to proteins of interest. The conjugation is covalently linked between NHS ester of the organic dyes and the amine group on lysine residues. Alternatively, the maleimide group can specifically target the cysteines. Although organic dyes are of about 1 nm in size and their quantum yield are far higher than fluorescent proteins, it's difficult to assess the labeling ratio on one antibody, i.e. stoichiometrical labeling. Moreover, the dye-conjugated antibody is not permeable through the plasma membrane of the cells, hence the labeling inside living cells are prohibited. On the other hand, genetically encoded fluorescent proteins (FPs) offer selective labeling ratio by joining the DNA sequences of FP and target proteins, and via the cells' internal machinery the chimera fluorescent proteins are synthesized and ready for live-cell imaging after correct folding and relocation. Since the green fluorescent protein (GFP) from jelly fishes *Aequorea victoria* was discovered and it has been widely used to internally label the target proteins for live-cell imaging and the variants of GFP also offer a palette of colors[17]. The pioneer work was awarded with the Nobel Prize in chemistry in 2008[52]. Many experimental methods[25] can be used to introduce FPs into the cells, the entire fusion gene constructs can be carried by bacterial plasmids, called transfection, or through the retrovirus transduction when the cells are reluctant to receive the constructs via transfection, such as primary cells, neurons and macrophages in this study. These traditional methods are however prone to the overexpression of proteins of interests, thus the interpretation of the results might be misleading from true cell physiology. Recent use of CRISPR/Cas9 as a gene editing tool becomes overwhelmingly popular as it has an efficient delivery of gene sequence by inserting or "knock-in" into specific gene targets, thus permits the endogenous FP labels[104][49].

1.3 Fluorescence microscopic techniques

Fluorescence microscopy has been the most versatile tool for biomedical researchers, for its selective labeling of specific molecules while keeping the others in the dark, thus providing the contrast to visualize individual molecules for investigation of their localization on defined structures or their movement and interaction with another labeled molecules[107]. The collection of all these information help scientists understand the functions of each molecule and the working mechanism by which they are involved in particular cellular phenomena[81]. By knowing the molecular mechanisms can potentially help develop possible cures in clinical treatment on patients suffering from the diseases or syndromes. Here the conventional fluorescence microscopy and other advanced imaging techniques used in this dissertation are briefly summarized as follows.

1.3.1 Wide-field microscopy and illumination schemes

In wide-field epiflouorescence microscope, the entire field-of-view of samples is illuminated by focusing the excitation light into the back focal plane of the objective. Each excited fluorophores is collected by the same objective and spectrally separated from the illumination light by an appropriate dichroic mirror. The emitted photons are separated from the back-scattered excitation light by an emission filter before it is detected by the camera (Figure 1.4A). More than one color of fluorescence can be imaged simultaneously if additional beam splitters of certain bandpass are placed in the detection path. The major draw back of this conventional design is that the detection of all signal from theventire sample volume makes the image blurred with glowing light from the out-of-focus planes that impairs the signal-to-background ratio and also accelerates the photobleaching (Figure 1.4B). In best scenario only the signal originating from the focal plane with a defined depth-of-focus generates a sharp image.

To circumvent this difficulty, alternative illumination strategies can be used to reduce the excitation volume. This is performed by shifting the excitation beam laterally towards the edge of back aperture of the objective, which results in the formation of a sheet of light penetrating the sample tissue where the in-focus fluorescence is detected with greater signal-to-background ratio. The thickness of the

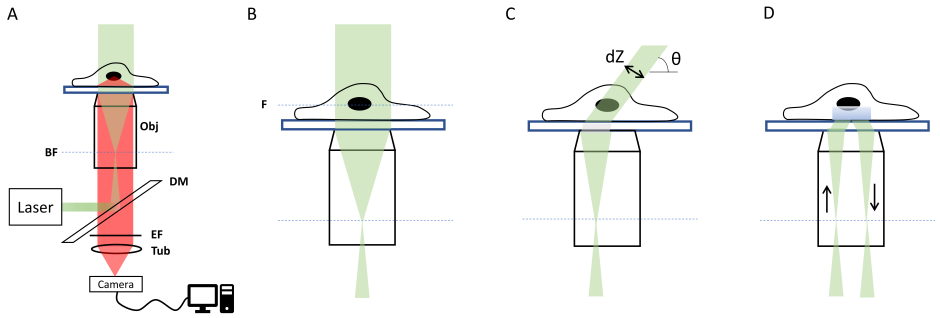

Figure 1.4: (A) Simplified drawings of the conventional epifluorescence microscope in the infinity optics design. (B-D) Variants of illumination schemes. (B) A beam of excitation light is focused onto the back focal plane which leads to form a collimated light used for wide-field illumination. (C) The shift of the focused beam from the center of the back focal plane creates a HILO sheet of less than 10 μm thickness (dZ). (D) Further increase of the incident angle to meet the TIRF condition and to generate evanescent wave close to the coverslip[98]. BF: back focal plane, Obj: objective, DM: dichroic mirror, EF: emission filter, F: front focal plane, Tub: tube lens.

excitation light sheet is defined by

$$dZ = \frac{R}{tan\theta}$$

where R describes the diameter of the illuminated area, θ is the incident angle in the specimen. The result is called highly inclined and laminated optical sheet (HILO) (Figure 1.4C)[136]. When a high numeric aperture objective (NA= 1.46, maximal incident angle= 73°) is used, then the tilting angle can be further increased to exceed the critical angle (66.9°),

$$\theta_c = arcsin\left(\frac{n_2}{n_1}\right)$$

which is defined by the refraction indices of the glass (n_1=1.52) and the sample medium (n_2=1.4). In this condition the excitation light does no longer pass beyond the interface between glass and sample, but instead is reflected from the interface. Although no light can directly illuminate the sample, an exponentially decaying evanescent radiation field of the illumination light occurs and can excite a very limited spatial range (100-200nm) of the specimen's fluorescence; typically the cell surface. The use of this illumination scheme is called the total internal refelction microscopy (TIRF)[8] (Figure 1.4D).

1.3.2 Deconvolution microscopy

Instead of using different illumination schemes to reduce the out-of-focus light or blur, the computational method called deconvolution can be applied to remove such blur from the original images. In this approach an image is first decomposed into a series of frequency components by Fourier transformation (FT) which is akin to what the optics does in the image formation (Figure 1.2), and then the in-focus information is extracted and reversely transformed back to the real space. In real space an image $D(x)$ is the convolution of the object $E(x)$ and the PSF $H(x)$, and can be symbolically represented as

$$D(x) = E(x) \otimes H(x)$$

But after FT the convolution operation becomes the multiplication product of the frequency response of the fluorescent emission $\tilde{E(k)}$ and OTF $\tilde{H(k)}$(i.e. convolution theorem)[41].

$$\tilde{D(k)} = \tilde{E(k)} \cdot \tilde{H(k)} \tag{1.1}$$

where tildes ($\sim$) is the Fourier transformation of the corresponding real-space quantities. Since we can decompose the image into separated frequency and the knowledge of OTF can be simulated or measured by using a fluorescence bead, the actual labeling frequency of the object can be isolated and inversely transformed back into real space as the deconvolved images.

$$\mathcal{F}^{-1}\tilde{E(k)} = \frac{\tilde{D(k)}}{\tilde{H(k)}}$$

But the mathematical problem comes when the OTF reaches to zero, because we cannot do division by zero value to get the labeling frequency. Therefore additional filters are applied to avoid the zero value in the division process. Wiener filtering[149], for example, includes a nonzero value which is based on the noise level in the denominator to help solve the division problem and deal with the signal-to-noise behavior of the OTF. In the commercial systems the constrained iteration approach[109][78] is used for the deconvolution processing, in which a repeating comparison between the acquired images and the guessing images blurred by the PSF is performed until the correlation of the two is high and the difference is converged to a certain constraint. It is of importance to know that the theoretical resolution of deconvolution microscopy is no difference from the conventional one.

The wide-field fluorescence images are simply cleaned up to show higher contrast which practically improves the effective resolution after deconvolution. It is particularly useful in the live-cell imaging which requires low light illumination to reduce bleaching and phototoxicity as no photons are wasted but instead reassigned to the focal planes where they belong to.

1.3.3 Confocal laser scanning microscopy

Confocal laser scanning microscopy, hereafter named confocal microscopy, is by far the most widely used microscopy method in current biological research. The word 'confocal' means that a point light source, the diffraction-limited spot on the focal plane and the detection pinhole all lie on the optically conjugated planes and, thus, are precisely aligned with each other[98]. This configuration corresponds to the confocal arrangement invented by Marvin Minsky in 1957[85], which is very different from wide-field fluorescence microscopes, in which the entire specimen is illuminated and the image is acquired frame-by-frame on the sensor chip of the camera. By contrast, in a confocal microscope, the excitation light of a point source is focused into a diffraction-limited spot and by moving the deflection mirrors the illumination spot is raster scanned across the sample to detect the emitted fluorescent photons. A point detector such as a photon multiplier tube (PMT) or an avalanche photon detector (APD) is used to convert the received photons into an electronic signal which is voltage-amplified and built up point-by-point into a complete image frame. Another great invention in this technique is to reject the out-of-focus contribution by applying a pinhole in front of the detector and, thus, it greatly enhance the contrast to obtain crisp images. By moving the illumination spot laterally as well as axially, not only the cellular structures in 2D but three dimensional structures of thick tissues or even small organ/animals can be imaged as well. It is owing to its optical sectioning capability inherent of the detection pinhole that the confocal microscope is one of the most successful instruments in the biological research market. Reducing the pinhole size can increase both lateral and axial resolution at the expense of the photon budget. The overall resolution in the confocal microscope is roughly a factor of $\sqrt{2}$ ($\sim$ 180nm) better than that in the conventional microscope ($\sim$ 250nm)[151].

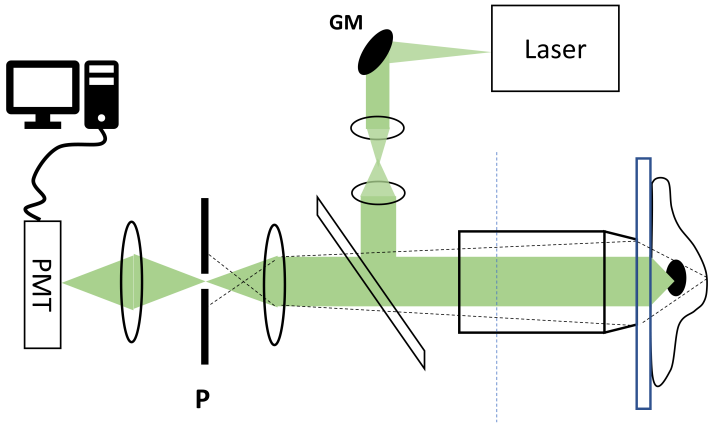

Figure 1.5: Schematic illustration of confocal detection. A point source of laser light is directed by galvonometer mirrors (GM) to fill up the back aperture of the objective and to form the excitation focus spot. While the fluorescence light derived from the focal plane will be allowed to pass the pinhole (P) and enter into the PMT, the emitted light originating from outside of the current focal position will be blocked by the pinhole (dash lines).

1.4 Superresolution microscopy

1.4.1 STED microscopy

Despite that the fluorescence emission is the typical spontaneous transition back to the ground state after the fluorophores are excited, stimulated emission is also another de-excitation pathway (Figure 1.7). Stefan Hell, Nobel laureate of 2014 chemistry, has once in an interview said he flipped around the physics book one day and found that the stimulated emission discovered by Einstein[5] could be used in his nanoscopic technique named stimulated emission depletion microscopy (STED)[45]. The optical setup is confocal microscopy-based, but two lasers are used, one for excitation and the other for fluorescence depletion. The depletion laser is delayed and modified by a phase mask in order to generate a doughnut profile with a zero intensity center where and only there the fluorophores are detected[46]. As a result the emission PSF is engineered to be a smaller spot that help detect individual fluorophores that otherwise can not be separated in the range of diffraction-limited illumination, and thus achieve superresolution (Figure 1.6).

The achievable lateral resolution of STED microscopy can be described as a modification from Abbe resolution formula:

$$d = \frac{\lambda}{2NA\sqrt{1 + \frac{I}{Is}}}$$

I is the illumination power of the depletion laser and Is denotes as the saturation intensity. In principle the resolution enhancement can be unlimited as more depletion power used leads to smaller depletion-free center that allows the fluorescence detection, but in practice high dosage of depletion laser causes serious photobleaching, albeit it is required to compete with spontaneous emission of the excited molecules. Hence, the near-infrared dyes (e.g. Atto 647N, STAR 635P) which intrinsically have a better photostability over visible ones are preferentially used for STED imaging[114]. Moreover, a far-red depletion laser has to be chosen accordingly to match to the red part of emission spectrum of the used fluorescent dyes or photoswitchable proteins in case of RESOLFT microscopy[48]. In addition to the lateral resolution enhancement up to around 50nm in practice, the axial resolution can also be improved by applying other phase modulation devices. For example, the spatial light modulator can be utilized to project the desired depletion masks on the excitation PSF and to generate a minimal emission volume in space.

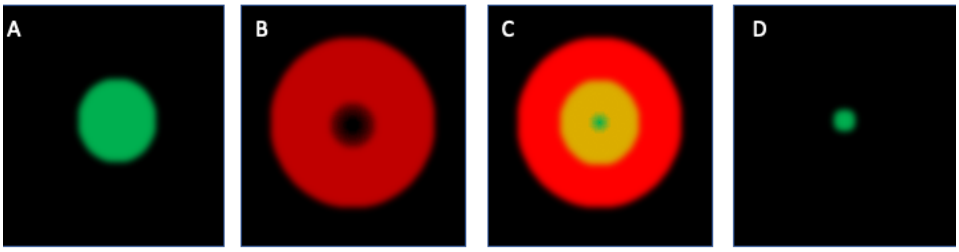

Figure 1.6: Illustration of the STED principle. (A) A Gaussion excitation beam is overlayed with a doughnut-shape depletion beam (B), as a result the excited fluorophores in the overlapped area (orange) are induced to emit photons by stimulated emission of radiation at a red-shift wavelength which are then filtered out before reaching the PMT detector (C). This allows only the fluorophores in the zero-intensity center of the doughnut are detected by spontaneous emission. Therefore, the effective PSF is smaller, thus the optical resolution is enhanced (D)[114].

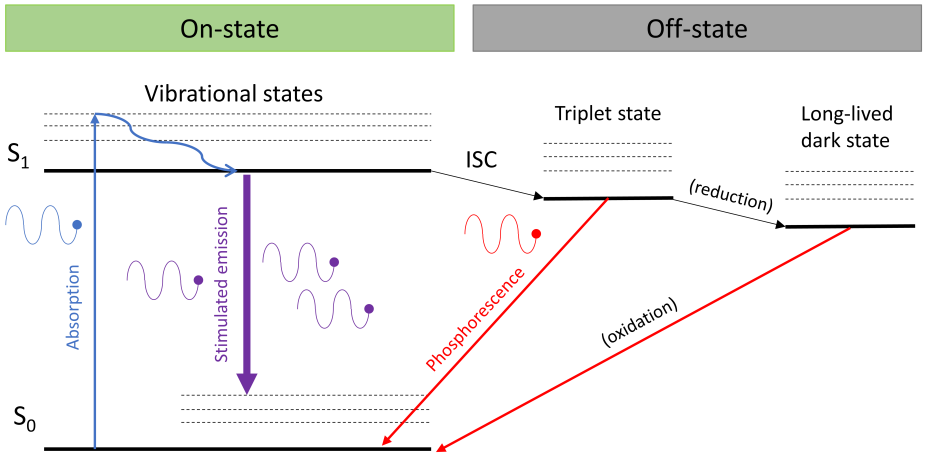

Figure 1.7: The extended Jablonski diagram shows the de-excitation pathways via stimulated emission, phosphorescence and non-radiative processes from dark state that are used in the development of STED and SMLM microscopy. In STED microscopy stimulation emission forces the excited molecules to emit photons with the same wavelength and phase as the incoming light (purple) which are filtered out from detection. As for SMLM, the triplet and dark states are "off-states" that provide the opportunity to localize the remaining "on-state" fluorophores individually[142].

1.4.2 Single molecule localization microscopy

Single molecule localization microscopy (SMLM) exploits an imaging strategy to temporally separate the otherwise spatially overlapping fluorescence molecules. The idea was fist outlined by Eric Betzig in 1995[13], longer before its realization [14][47][111]. The imaging scheme is to acquire only a subset of fluorescent emitters that are distributed in low density. This allows algorithms to detect single emitters and pinpoint its location by a Gaussian fit on the PSF and to record the coordinate of the centroid. By repeating this process to sequentially obtain numerous localization events from tens of thousands of the image frames, a localization list of all emitters can be created and used to reconstruct one super-resolved image. In this single molecule detection approach the resolution limit turns to the localization precision of a single molecule Δx which is dependent on the number of emission photons N.

$$\Delta x = \frac{\sigma}{\sqrt{N}}$$

where σ is the standard deviation of the localized positions in lateral direction. To put the concept into practice, direct stochastic optical reconstruction microscopy (dSTROM) uses organic dyes (e.g. Alexa647) to obtain temporally separated emitters through the on-off switching behavior of the dyes (blinking)[142][21]. It is achieved with a high power illumination to drive the excited fluorophores into the triplet off-state from which they emit photons with a time delay of microseconds (Figure 1.7), thereby the individual positions are discerned from another. The triplet state can be further reduced to a prolonged dark state (up to seconds) in the presence of thiol agents such as β-mercaptoethanol or β-mercaptoethlynamine, and the oxygen is additionally depleted by glucose oxidase in the imaging buffer[88][21]. The fluorophores dwelling in this states can be de-excited with the aid of UV light or oxidation, but emit no photons in the non-radiation process. With most molecules in the off-state, it is possible to detect a few molecules that are still in on-state and localize their positions by software fitting. The photoconvertable or photoactivatable proteins are used in the live-cell studies, here termed as photoactivated localization microscopy (PALM)[56]. But they are generally lack of sufficient photon emissions, therefore a small tag such as Halo or SNAP enzymes can be genetically labeled on the target proteins for live-cell SMLM imaging. The localization precision in SMLM can achieve a near-single molecule resolution of approximately 20-30nm in lateral dimension. This technique was also extended into axial resolution enhancement by introducing astigmatism to encode the axial positions in different shapes and orientations of the emission PSFs[50][145].

1.4.3 Structured illumination microscopy

As it is mentioned above that Abbe postulated the image formation as the transfer of the diffraction patterns, such as a grid, that is composed of certain frequencies. The microscopic system transfers the spatial frequency through optics and since the aperture of the lens is finite the transfer function of the microscopes is band limited. That means not all frequency information is delivered into the image formation, instead the frequency higher than the frequency support of the microscopes is lost and hence the small details are missing in the images[43] (Figure 1.2). In fact, the imaging system acts as a frequency filter to set the limit on how high the frequency can pass through the optics or how much fine structures can be represented in the images. This cut-off frequency is then denoted as the diffraction limit of the optical system. Super-resolved structured illumination microscopy (SR-SIM) refers to the

technique that partially restores those high frequency information that are beyond the frequency cut and lost in the optical systems[44][128][153].

Principle of SR-SIM

Structured illumination microscopy is based on the wide-field fluorescence detection but the sample is illuminated with spatially spaced line patterns (stripes), which encodes the originally inaccessible information into the moire fringes in the raw images (Figure 1.8A), and the fine structures of the sample are obtained after computational reconstruction to surpass the Abbe limit with double lateral resolution enhancement [44][153]. The working principle is to project the sinusoidal pattern of illumination created by two-beam interference on the fluorescent samples, of which the higher frequency information can be shifted into the detectable range of the optics that otherwise cannot be achieved in conventional microscopes (Figure 1.8B-D).

It then requires further unmixing computational procedures to extract such information during a reconstruction process. For this purpose, a series of the structurally illuminated images in varying phase shifts of the illumination pattern- 3 equivalent shifts for 2D - are acquired to help create a set of linear equations to unmix the frequency components that encode the high resolution information. The extracted high frequency information is then shifted to the correct frequency space with the knowledge of illumination pattern frequency (Figure 1.8E). Next, the illumination stripes are rotated with the different angles (0, $\pi/3$, $2\pi/3$) in order to get the isotropic resolution enhancement (Figure 1.8F). Totally 9 frames of images (3 phases x 3 angles) are recorded in 2D-SIM. Finally, the obtained data in frequency space is inversely Fourier-transformed back to a super-resolved image. Based on the incoherent sample response, the resolution power of the optical system can be achieved corresponding to the sum of the maximum illumination frequency and highest sample frequency of which the optics can collect.

$$R = \frac{1}{f(illmuniation) + f(optics)}$$

The maximum illumination frequency is again intrinsically dependent on the objective that is also used to collect the emitted fluorescence. Therefore, the theoretical resolution improvement of SIM can be at best doubled from the conventional far-field microscopy.

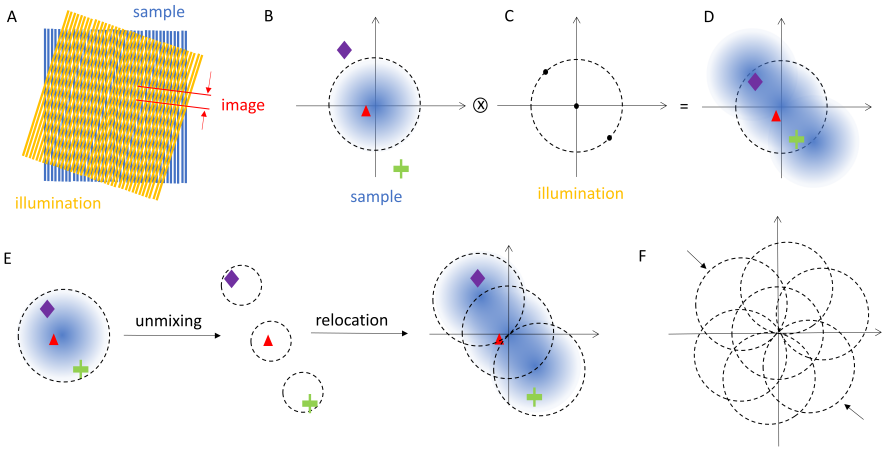

Figure 1.8: Illustration of the SIM concept.(A) The moire effect is formed when two patterns of certain frequencies were superimposed and generate a new pattern frequency that has a coarser spacing than the original one. In SIM microscopy we consider that one of the pattern is the sample containing unknown structures, the other is the excitation stripes used to illuminate the sample in purpose. The outcome would be the image which now possesses the information of unknown structures encoded in the new pattern that is now detectable in the microscope. (B) The same methology can be also exemplified in the frequency space where the sample image is Fourier tranformed into components (blue clouds) distributed within the OTF boundary of the microscope (dotted circle). Only information falling into this region (e.g. triangle) can be accessible in optics, whereas others outside this range are undetectable (e.g. diamond and cross). (C) The sinusoidal wave illumination has three distinct components which have the interspace equal to the maximal frequency support of the microscope. (D) The moire effect appears as the convolution of the sample and illumination frequency components gives rise to the displacement of sample components with three offsets in the reciprocal space. The shift of the sample frequency brings the previously undetectable information into the observable region (dotted circle). (E) However, this region is the sum of three contributions that contains not only the higher frequency of interest but also the other mixed components. Hence, the higher frequency need to be separated from the mixtures and shifted back to correct positions. As a result the frequency support is now expanded, therefore the resolution enhancement is achieved. (F) The same procedures can be repeated for the other orientations to acquire equal extended frequency support in all directions. The expanded observable region is now doubled and so is the lateral resolution enhancement of the reconstructed image after inverse Fourier transformation back to real space.

Computational reconstruction

The mathematical operation of frequency unmixing can be briefly described here[154]. As previously mentioned, equation (1.1) has the fluorescence emission of

the object $E(x)$, which is actually the product of labeled structures $S(x)$ and the local illumination intensity $I(x)$, i.e. $E(x) = S(x) \cdot I(x)$. After Fourier transformation, $S(x)$ times $I(x)$ becomes the convolution between the two, therefore equation (1) is expressed now as

$$\tilde{D(k)} = (\tilde{S(k)} \otimes \tilde{I(k)}) \cdot \tilde{H(k)} \tag{1.2}$$

For $\tilde{S(k)}$ is the sample information collected within the OTF support (Figure 1.8B). $\tilde{I(k)}$ is the three-dot components of the illumination stripes (Figure 1.8C) and can be expressed by using Euler's formula

$$\tilde{I(k)} = I_0[(\delta(k) + \frac{c}{2}e^{i\varphi}\delta(k - k_0)) + \frac{c}{2}e^{i\varphi}\delta(k + k_0)]$$

where k_0, φ, c and I_0 are the frequency, initial phase, modulation contrast and mean intensity of the sinusoidal wave pattern. Next, equation (1.2) can be rewritten as

$$\tilde{D(k)} = I_0[\tilde{S(k)} + \frac{c}{2}e^{i\varphi}\tilde{S(k - k_0)} + \frac{c}{2}e^{i\varphi}\tilde{S(k + k_0)}] \cdot \tilde{H(k)} \tag{1.3}$$

To solve the equation (1.3), $\tilde{D(k)}$ can be obtained from the raw images of SIM and $\tilde{H(k)}$ is the OTF support of the microscope, which can be estimated or measured from the system. The rest of unknown is the high frequency components encoded in $\tilde{S(k)}$, $\tilde{S(k - k_0)}$ and $\tilde{S(k + k_0)}$, which require additional information from the phase-shift images. Therefore, the sample is illuminated sequentially with 3 phase-shifts of the pattern to produce linear equations in a matrix form to resolve the sample components. After decoding, the gained information is shifted and recombined into a final resolved image.

It should be noted that although the use of pattern illumination has been conceptualized long ago, it was not realized until the mathematical solutions to the unmixing and weighted averaging approaches were provided by Heintzmann[42] and Gustafsson[38]. The reconstruction procedures (unmixing and reassembly) of the newly obtained frequency components required the precise knowledge of the illumination patterns, such as phase offset, rotation angels, modulation depth and PSF. The required information can be estimated by the FFT of the raw images or by the cross-correlation between the phase shifts[154]. The final reconstruction is

achieved by relocation of the isolated frequency components at the correction positions in Fourier space with the overlapped regions. A weighted averaging approach is used to overlay the components in combination of Wiener filter to suppress the noise contribution at the peripheries. Finally, the complete assembled components are then smoothed out by the window function (apodization) to remove ringing effects before it is inversely transformed into the final images.

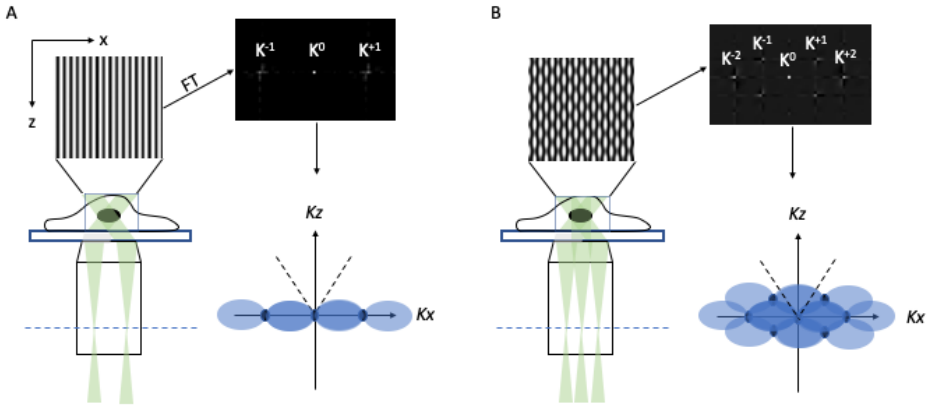

Figure 1.9: Illumination schemes of 2D and 3D-SIM. Two- (A)or three-beam (B) illumination are used to generate the respective light patterns which are displayed in axial section. (A) In 2D-SIM geometry the sample is illuminated by two beams of light, which interfered in the focal plane to form a sinusoidal light intensity profile that can be Fourier transformed (FT) into three frequency components (from left to right: *K-1, K0, K+1*). If the components are multiplied with the observable region of the microscope frequency support OTF, then the three shifted copies of OTF sit along the lateral axis (Kx). This yields twice the normal lateral resolution but suffers from the lack of frequency support on the kz axis, known as "missing cone" problem (dashed lines). (B) On the contrary, when the third beam is introduced together with two side beams, an intensity pattern is obtained with both lateral and axial structure, i.e. a 3D pattern. In frequency space this illumination structure appears as seven dot-like components, but two of them in the lower part are shared by pairs of intensity components. Therefore only five transfer functions/phase shifts, namely *K-2,K-1, K0, K+1, K+2*, are required for reconstruction in 3D-SIM. Note that the missing cone region is now filled up by the shifted OTFs of the first-order and thus the axial resolution is doubled as well as the lateral one[39].

Resolution enhancement in three dimensions

Since the optical setup of 2D-SIM is based on wide-field fluorescence microscopy, it is also confounded by out-of-focus light coming from outside the focal plane that causes the periodic reconstruction artifacts (i.e. honeycomb patterns)[20]. This

drawback can be explicitly shown on the frequency space, in which the lack of frequency information near the axial direction is called the missing cone problem (Figure 1.9A). The OTF attenuation can be optionally used during the reconstruction process to help minimize the artifacts, as well as the Richard-Lucy-based deconvolution are used to filtered out the background contribution[100]. Other illumination schemes employed the increasing incident angles of the two interference beams to have the grazing-incidence (GI-SIM)[35] or TIRF-mode illumination (TIRF-SIM)[71] that aims to receive only in-focus fluorescent light.

Alternatively, three-dimensional SIM (3D-SIM) can provide another solution. The adapted illumination pattern in 3D is generated by three-beam interference which can not only provides the axial information to fill up the missing cone, but the resolution improvement can be also extended to the axial direction. The illumination strategy is to use the 0-order diffraction beam from the grating in combination with the two 1st-order side beams, forming three-beam interference that gives rise to extra patterns in the axial axis (Figure 1.9B)[39][28]. In practice, the sample structures are illuminated with 3 rotations and 5 phases in each focal planes (Figure 1.10A and B), then repositioned to the next axial position with a stepwise of 125nm to meet Nyquist's sampling criterion and repeated for the rest of the Z-stack volume. It is worth noting that the later spacing of the illumination pattern is doubled so the stripes appear clearly in the raw images of 3D-SIM, which is however not visible in the 2D scheme. The result after the computational reconstruction described previously is a resolution enhancement by a factor of two in both lateral and axial direction (Figure 1.10C). SR-SIM has been widely shown as a powerful tool to study the 3D structure in finer details[118][44][39] and is also the major microscopic technique used in this dissertation.

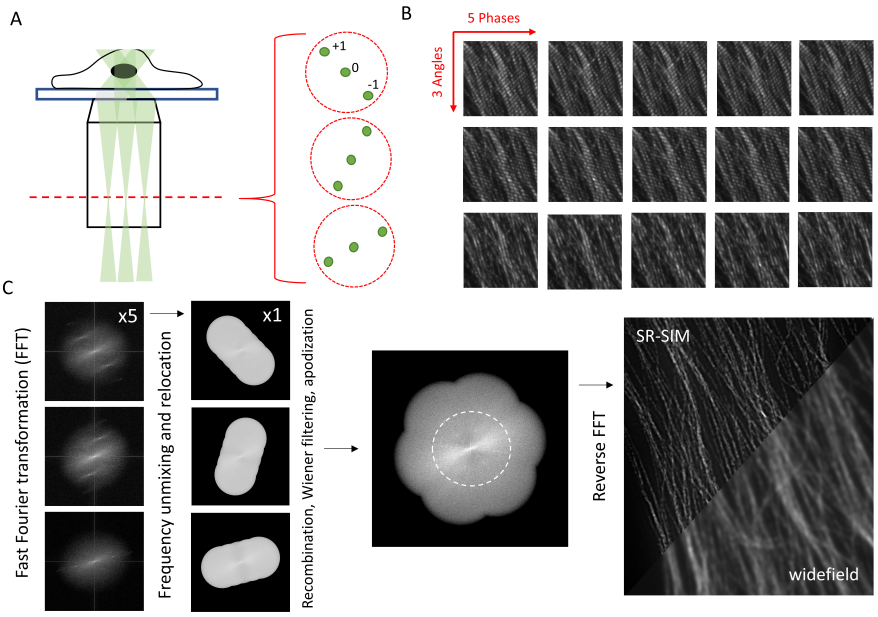

Figure 1.10: Image acquisition and reconstruction in 3D-SIM.(A) Three diffraction rays (-1, 0, +1) from the grating device are focused into the back focal plane of the objective to generate a three-beam interference in the sample plane as shown in B. The rotation of the 3 beamlets is directed by the corresponding galvonometer-driven mirrors onto one of three beam paths and thus creates the angular orientations. 5 shifts of the pattern are produced by using a delay prism placed on the light paths of the two first order beamlets (see Material and methods). The 3D volume of the specimen is recorded by the moving the stage up and down. (B) Raw images of 15 frames are thus produced by the phase-shifts and angular orientations of the illumination patterns. The representative raw images were recorded by a cell sample immunolabeled with the anti-β-tubulin with Alexa 488. (C) Representative images of each orientation are converted to the spatial frequency components, of which the high/SR frequencies are separated the lower one with the information acquired at 5 different phase positions of the SIM stripe pattern, and shifted to the correct locations in frequency space. They are rejoined, filtered and processed by the apodization function to produce an isotropic expansion of the observable range wider than wide-field microscopy (dotted circle). Finally, the data are inversely Fourier transformed into the real space, thus producing a resolution-doubled image compared with the wide-field fluorescence image. The intermediate and final images are processed and reconstructed from the raw images in B by fairSIM[87].

Chapter 2

Fluorescence microscopy of bacterial endotoxins

2.1 Introduction of endotoxins

Ever since we were born, our body fight against the microbes or pathogens every day and every minute. Our skin could be considered as the first barrier preventing the intrusion of microorganisms from the environment. But once the bacteria penetrate our body, the immune system would act to recognize, remove them to reduce the damages caused by the pathogens. The human immune system consists of two defending mechanisms: the innate and the adaptive immunity[86]. The former is crucial for fast responses to pathogenic infections while buying time for the adaptive approach (e.g. antibody production) to take effects on the specific targets.

In case of bacterial infection, lipopolysaccharide (LPS), also called endotoxin, is recognized by our innate immunity system[148]. LPS plays a dominant role in sepsis or septical shock resulted from the uncontrolled release of proinflammatory cytokines from white blood cells in inflammation. The massive production of inflammatory cytokines ultimately leads to fever, pain and multiple organ failure (e.g. lung, kidney and heart)[16]. In the US, one-third of patients who die

in a hospital have sepsis[106][40]. It is thus of great importance to understand how the picograms of endotoxin induces the cellular immune responses and how it transduces the signal into the expression of genes involved in inflammation.

2.1.1 Molecular structure of bacterial endotoxins

Endotoxin or lipopolysaccharides (LPS) are glycolipids embedded in the Gram-negative bacterial outer membrane. It is composed of three distinct regions: the lipid A, the core and O-antigen. The lipid A consists of a bisphosphorylated disaccharide with glucosamine backbone linked by various number of fatty acid chains that inserts into the bacterial membrane. Attached to the lipid A is the core region of short oligosaccharides, which is further extended with a carbohydrate chain of distal part of LPS, the O-antigen (Figure 2.1). This is the composition of smooth type of LPS, it ,however, varies among different bacterial species and strains. In some bacteria strains the endotoxins produced without O-antigen are called rough-type LPS or lipooliogosaccharides (LOS)[148].

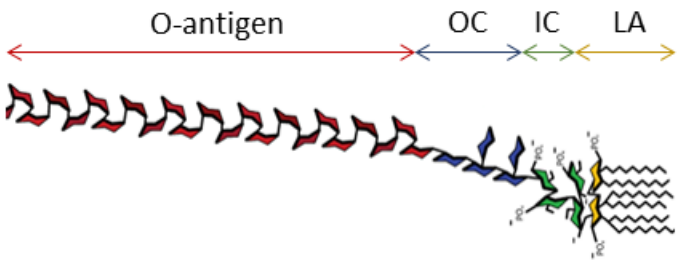

Figure 2.1: Schematic illustration of LPS structure. OC: outer core, IC: inner core, LA: lipid A. It is adapted from Wikipedia: en.wikipedia.org/wiki/Lipopolysaccharide.

2.1.2 Formation of TLR4 receptor complex

One of the multiple response mechanisms of the innate immune system is to use the cell receptors to recognize various conserved molecular structures stemming

from microbes. The molecular pattern of LPS is recognized by Toll-like receptor 4 (TLR4), which, upon activation, conveys the downstream signal to trigger cytokine release and attract immune cells to clear the pathogens. However, CD14 was the first proposed corresponding surface receptor reactive to LPS with high-affinity binding[115]. Although CD14 also exists in soluble form (sCD14), it has a GPI-linked form that anchors to the cell membrane (i.e. mCD14). However, the latter form has no intracellular domain to transduce the signal inward, which suggested that additional protein(s) might mediate signaling across the plasma membrane to the cytoplasm. This led to the discovery of new candidates on the genetic deficiency mice which were shown resistant to LPS administration[6]. Toll-like receptor 4 (TLR4) was later found to play the main role of initiating the signal transduction as researchers found that the TLR4 gene-knockout mice were resistant to LPS-induced sepsis model and their macrophages expressed no genes in response to LPS[130].

As mentioned above, LPS is derived by the intruding bacteria. After entering into our circulation system, LPS is first transported to the cell surface by the sequential action of LPS-binding protein (LBP) and CD14. It binds to LBP which acts to transfer LPS monomers out of the LPS aggregates to a binding site on either soluble or membrane-bound CD14. The LPS-CD14 complex then facilitates LPS transfer to its receptor TLR4, which, needs MD-2 to receive LPS and forms TLR4/MD-2/LPS complex. MD-2 belongs to the family of lipid recognition, it has a large hydrophobic pocket to which the lipid A moiety inserts. In particular, five of the six acyl chains in lipid A insert into MD-2 cavity whereas the sixth acyl chain help the interaction with another TLR4/MD-2/LPS counterpart and thus completes the entire receptor complex(Figure 2.2)[95][112]. Taken together, CD14 and MD-2 were identified as key molecules essential for LPS recognition, whereas TLR4 is responsible for inducing LPS signal transduction.

2.1.3 Signaling transduction of endotoxins

The molecular mechanism by which endotoxin exerts its immunological actions is briefly described here. Once the dimerization of TLR4 is formed, LPS initiates two independent signal pathways[110][4] the MyD88-dependent pathway, which starts at the cell membrane with the formation of the Myddosome[72], a macromolecular signaling complex formed by MyD88 and IRAK members leading to NF-κB activation and the production of inflammatory cytokines, such as tumor necrosis

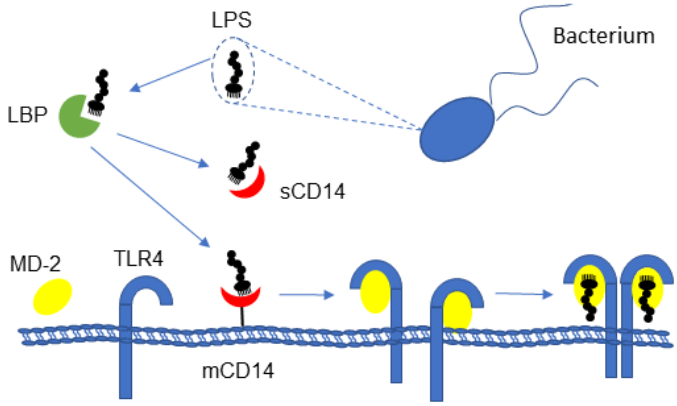

Figure 2.2: Schematic representation of LPS being transferred from Gram-negative bacteria to the formation of TLR4 receptor complex.

factor α, IL-6 or pro-IL-1β. Alternatively, the TRIF-dependent pathway, which originates from the early endosomes, is activated and leads to the formation of the supramolecular Triffosome complex to drive type I interferon production (IFN) and delayed NF-κB activation[131].

Detail descriptions of signaling transduction are written as follows and also shown in Figure 2.3. Upon the ligand detection, the signal generated from the TLR4 will be transduced to downstream effectors, such as MyD88 and TRIF. But the intracellular domain of TLR4 cannot directly interact with them, it instead requires adaptors to bridge over the signaling. TLR4 uses its highly conserved cytosolic part called TIR (Toll-like/IL-1 receptor) domain to recruit TIR-adaptor proteins (TIRAP). In the case of proinflammatory signaling, TIRAP recruits the downstream effector, MyD88, and the members of IL-1R-associated kinases (IRAKs). These proteins are like building blocks which conduct self-autophosphorylation and oligomerize themself into a signaling complex named Myddosome[30][31]. Next, the tumor necrosis factor receptor-associated factor 6 (TRAF6) binds to the Myddosome and activates downstream kinases which help to release the NF-κB (i.e. the p50/p65 heterodimer) from IκB and thus entering into the nucleus to initiate the gene expression of inflammation-inducing cytokines[32].

On the other hand, MyD88-independent signaling is generated after the internalization of TLR4 into the early endosomes, it is therefore often referred to as

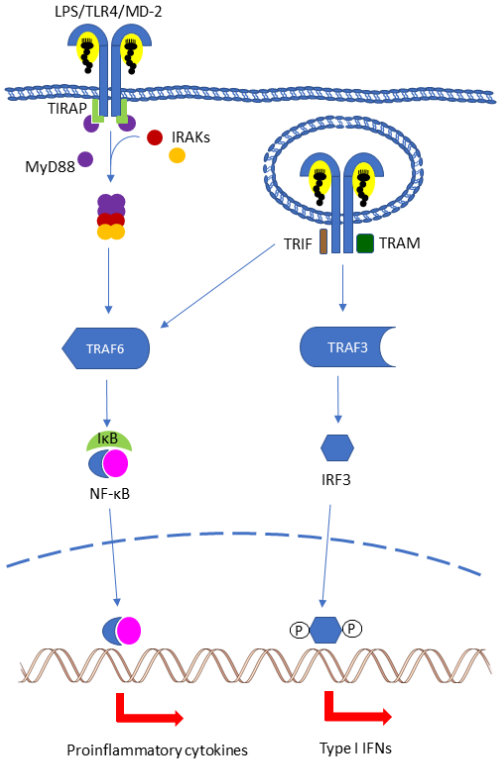

Figure 2.3: Schematic illustration of two LPS signaling pathways generated from the plasma membrane and the early endosome.

endosomal signaling. It is mediated through the binding of TRIF-related adaptor molecule (TRAM) and TIR-domain containing adaptor inducing interferon-β (TRIF)[29]. Both of them act as the adaptors and are together known as Triffosome, which activates TRAF3. In the aid of effector kinases, TRAF3, in turn, induces the phosphorylation of interferon regulatory factor 3 (IRF3), which gains the access to the cell nucleus and turns on the expression of type-1 interferon genes. In addition, TRIF was shown to interact with TRAF6[54], thus enabling to cross-activate the NF-κB signaling in a delayed fasion[59]. It is worth noting that by the nature of receptor endocytosis which takes minutes, it is logically assumed that the endosomal signaling is produced later than the Myddosomal one which is generated

upon TLR4 activation on the cell surface. It is also the explanation for the delayed NF-κB signaling driven by TRIF coming from the endosomal pathway.

2.2 Fluorescence imaging of LPS

Lipopolysaccharide (LPS) acts as a potent inflammatory inducer which can cause a life-threatening pathogenesis of sepsis and septic shock[93]. To prevent such immune disorder, it is important to remove the receptor-binding LPS from the cell surface by internalizing it into the cells and to degrade them in the lysosomes[51]. The molecular mechanism, however, requires better understanding with microscopic techniques of higher spatiotemporal resolution. We observed the fluorescent LPS uptake events on the established cell model with the use of deconvolution, structured illumination microscopy (SIM), and single-particle detection under total internal reflection fluorescence (TIRF) illumination in the following subchapters. All images were acquired on the DeltaVision deconvolution microscope and OMX 3D-SIM, which has the aforementioned imaging modalities (see Materials and methods).

2.2.1 Deconvolution microscopy of internalized LPS

Nowadays the fluorescently labeled LPS are available with a variety of colors, owing to the previous efforts done on the improvement of chemical conjugation approaches[137]. This makes the visualization of LPS in contact with its surface receptors and the subsequent cell uptakes possible on the fluorescence light microscopes. However, to observe the presence of LPS in single cells, simply treat the immune cells such as macrophages with up to micrograms of fluorescent LPS is not enough. The emitting signal is still below the detection level of the microscopes, albeit picograms of LPS permits the cell activation and secretion of pro-inflammatory cytokines. Instead, additional expression of the coreceptor, CD14, is required to visualize the LPS, for its high binding affinity to LPS and presentation of LPS to TLR4/MD2 heterodimers[69].

Therefore, we constructed cell models using the human embryonic kidney cells (HEK) or human osteosarcoma cells (U2OS), which were transiently expressed TLR4 and MD-2, as well as CD14. Cells were first transfected with expression

plasmids of hTLR4-Venus fusion protein and hMD2/CD14, for 48 hours and then treated with LPS-Alexa 568 (LPS-A568) for 5-30min followed by a brief wash with fresh medium prior to acquisition under the deconvolution microscope. In accordance with the previous reports, the cell surface-bound LPS can be observed within a few minutes, as revealed by its staining on the sheet of cell membrane, lamellipodia and filopodia (Figure 2.4). On the other hand, cells transfected without CD14 usually take overnight incubation to internalize LPS via the macropinocytosis by which the fluorescence appeared wrapped up inside the vesicles rather than surface staining of the vesicles (data not shown).

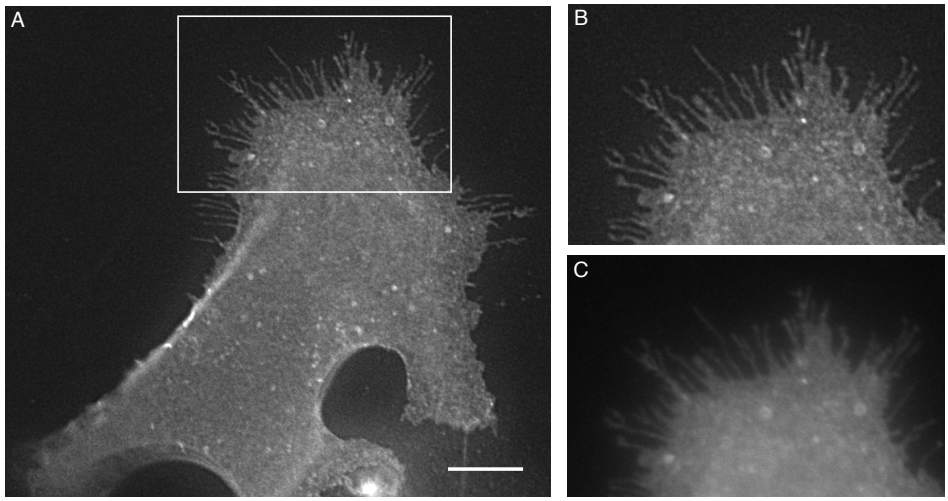

Figure 2.4: Deconvolution image of a CD14-transfected HEK cell treated with LPS-A568. (A) Single slice of deconvolution image was first acquired in z-stack under wide-field and then deconvoluted by built-in algorithm. (B) The magnified region cropped from white box in A showing the staining pattern of fluorescent LPS, as compare with the blur in the wide-field image (C). Scale bar= 10 μm.

Next, we'd like to confirm the presence of internalized LPS in endocytic vesicles as they undergo receptor-mediated endocytosis. Cell treatment with LPS-A568 was conducted together with live-cell compatible dyes which preferentially bound to particular organelles (Figure 2.5). In the cotreatment experiment, the presence of LPS was first found along the cell margin, and a few numbers of LPS-positive vesicles resulted from the invagination or pinching-off from the plasma membrane appeared as spot-like objects in the vicinity of plasma membrane (Figure 2.5A and B). Some of them moved gradually toward the nucleus and grew in size as they

might self fuse and thus revealed the void of vesicles (Figure 2.5C). As expected, the LPS was colocalized with Dextran, which is also a polysaccharide and widely used as an endosome marker (Figure 2.5D). This suggests that the LPS is internalized via the endocytic pathway and transported toward the lysosome or Golgi apparatus[51]. But it would never found to fuse with mitochondria (Figure 2.5B), yet perfectly overlaid with another Cy5-conjugated LPS (Figure 2.5E). The images obtained in this experiment were used to evaluate the colocalization between LPS and the individual markers (Figure 2.5F). The result showed a high score of LPS-A568 colocalization with LPS-Cy5 and Dextran, but surprisingly only a baseline score with hTLR4. The overall expression of hTLR4 in the cytoplasm could be the main reason attributed to the low score of colocalization with internalized LPS.

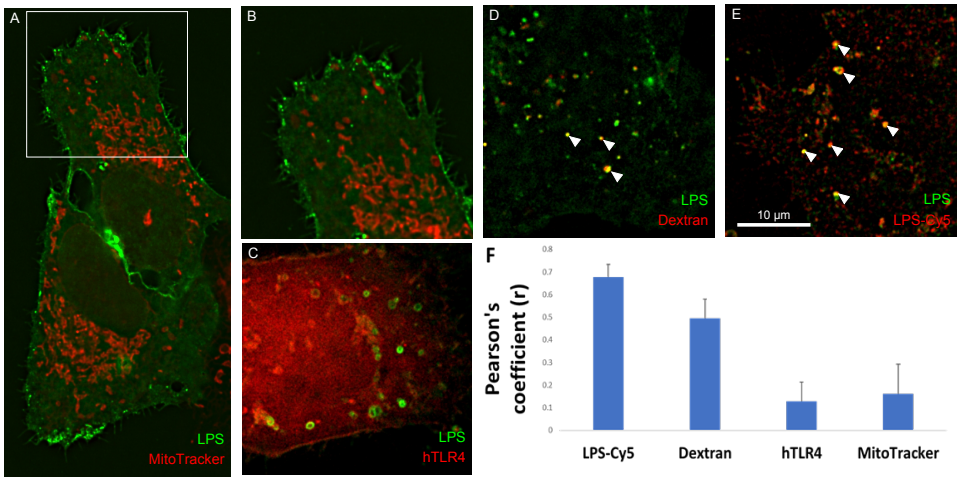

Figure 2.5: Subcellular localization of LPS-A568 was observed by cotreatment with indicated markers on the transfected U2OS cells (A-E), except hTLR4 was expressed as fluorescent fusion protein, Venus. Note that B is the enlarged view from the inbox in A. The colocalized vesicles were marked with arrows and all images were shown as a single optical section after the 3D deconvolution process and were further analyzed with ImageJ plugin tools, Colocalization Finder (F). Scale bar= 10 μm.

2.2.2 Structured illumination microscopy of endosomal LPS

To visualize how the surface-bound LPS was internalized into the cytoplasm, I turned my focus on the LPS-labeled vesicles in the vicinity of the plasma membrane where they are initially formed. 3D-SIM was used to resolve the vesicular struc-

ture of the smallest early endosomes given by the resolving power of the system. As compare with the wide-field image which always contains out-of-focus blur that deteriorates the quality (Figure 2.6A), the 3D-SIM, on the other hand, can substantially remove the unwanted light contribution after computational reconstruction (Figure 2.6B). This gives a clean background as the first benefit received from SIM techniques. It is in fact attributed from using the 3-beam illumination that ultimately fills the missing cone in the axial direction and thus performs the optical sectioning similar as one can obtain by confocal microscopy in which the physical pinhole is utilized to reject the out-of-focus light. Second, the lateral resolution is undoubtedly improved as well. In a single slice, the spot-like vesicles can now be clearly seen as circular rings which are formed by the CD14-mediated endocytosis after the LPS was bound to the mCD14 on the cell surface (Figure 2.6C).

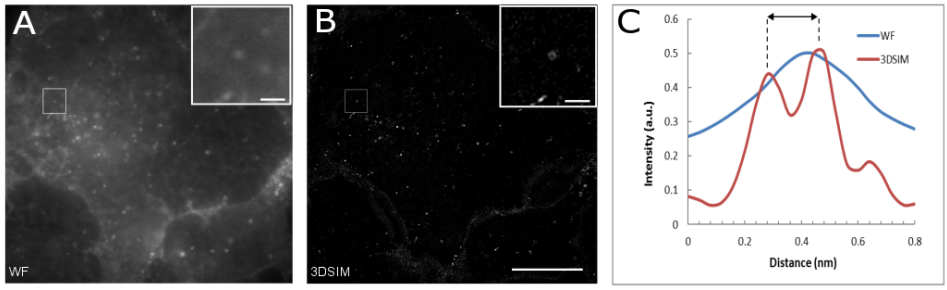

Figure 2.6: 3D-SIM technique improves the imaging resolution from conventional wide-field imaging (WF). CD14-transfected HEK cells treated with LPS-A568 were imaged on the basal layer of the plasma membrane. Single slices from z-stack images of wide-field (A) or SIM reconstruction (B) are shown, respectively. Insets are zoom-in micrographs of the boxed regions to highlight the single vesicle. (C) A line profile of intensity drew over the same vesicle in the insets indicated the size of the vesicle is approximately 200 nm. Scale bar= 10 μm. Inset bar=1μ m

2.2.3 Single-molecule tracking of membrane-bound LPS

Since the formation of the LPS endosomes starts from the binding of LPS on the cell surface, it is interesting to know more about the membrane biology of LPS, for example, how is the distribution of the bound LPS on the plasma membrane before they are internalized into the early endosomes. Do LPS molecules tend to cluster into microdomains (lipid rafts) where TLR4 and CD14 locate? In an attempt to understand more on this perspective, TIRF illumination is the microscopic technique widely used to visualize the fluorescent labels on or close to the

basal membrane while the rest part of the cell is not excited[8]. This is a selective illumination approach to gain effectively clear background and thus higher contrast imaging on the plasma membrane. Moreover, one can also record the movement of single fluorescent particles in living cells. The methodology is called single-molecule tracking, which allows hundreds or thousands of individual molecules to be visualized within living cells at sufficiently high spatial and temporal resolution that they can be observed and tracked over a period of several seconds[79].

For the visualization of single fluorescent LPS particles on the basal cell membrane, U2OS cells were transfected with CD14 for two days and on the day of measurement, cells were briefly treated with LPS-A488 for 5 minutes and rinsed with fresh medium. TIRF illumination was used to image LPS bound to the cell surface (Figure 2.7). Typically, the density of LPS labeling is always too high at the initial frames of acquisition for the analysis tool to identify individual LPS particles. A bleaching step is thus generally needed to lower down the density to clearly separate individual diffraction limit-spots. Moreover, some LPS molecules tend to gather as clusters on the cell surface. Their identity was checked by comparing to the corresponding wide-field image which revealed that they are essentially the internalized vesicles locating beneath the plasma membrane, and therefore were excluded for single particle analysis (data not shown). A successful tracking is presented in Figure 2.7 where the detected particles were simultaneously tracked and their trajectories were recorded. Each point-spread-function spots was identified as a diffraction-limited spot with a designated ID. The identified objects were traced in the time sequence by using simple LAP Tracker (Trackmate, Fiji) (Figure 2.7A) to yield individual particle trajectories (Figure 2.7B). The information on time, lateral coordinates and fluorescence intensity were stored for post-processing analysis in which the short-lived particles can be filtered out to reveal those particles of longer tracks (Figure 2.7C,D) and to monitor their intensity fluctuation (Figure 2.7E). Note that the movement of the LPS can only be recorded when the fluorophore is in the on-state and remains in the range of evanescence field. However, if single particle emitter is floating near the basal membrane of the cells rather than directly bound on the cell surface, it will appear only in a few consecutive frames and therefore be rejected from the applied filters in the tracking analysis.

The single-molecule tracking relies highly on the contiguous movement of a spot-like object, the exposure time is thus preferentially kept in less than 50ms, which in turn requires enormous excitation power to get a fairly good signal. This causes inevitably photobleaching of the single emitters at the end of individual tracks.

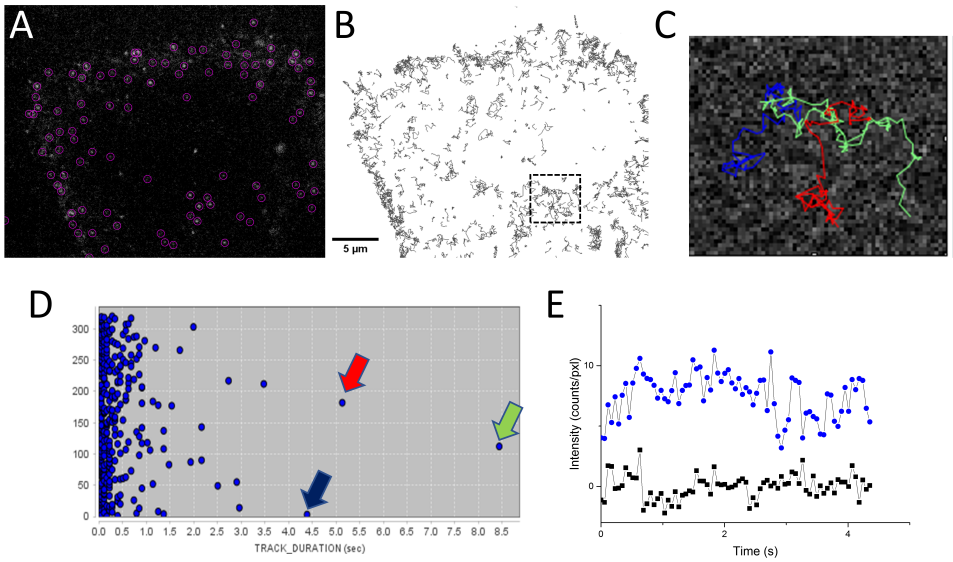

Figure 2.7: Single-molecule tracking on a single HEK cell transfected with CD14 and treated with LPS-A568 in TIRF mode. (A) A single frame (50ms) with the identified single particles marked with purple rings. (B) A total 829 tracks of moving LPS identified from the cell recording. (C) Tracks are isolated from the ROI box in B and filtered for the long-lived particles shown in colors. (D) A plot of all tracked particle IDs versus time duration (sec). Note that three arrows indicate the individual tacks in C with the corresponding colors.(E) An intensity profile of a single particle trace (blue) is plotted together with the background noise measured in a non-fluorescent neighboring region (black).

Therefore the recording time of single-molecule tracking is not long enough to observe, if any, the clustering of LPS molecules in a restricted region where they are later incorporated into the cells as endosomal vesicles. However, a short interaction between two single particles was indeed observed when they fused and split from each other, which may imply the pursuit of TLR4 receptor complex formation via the dimerization of two receptor monomers (Figure 2.8).

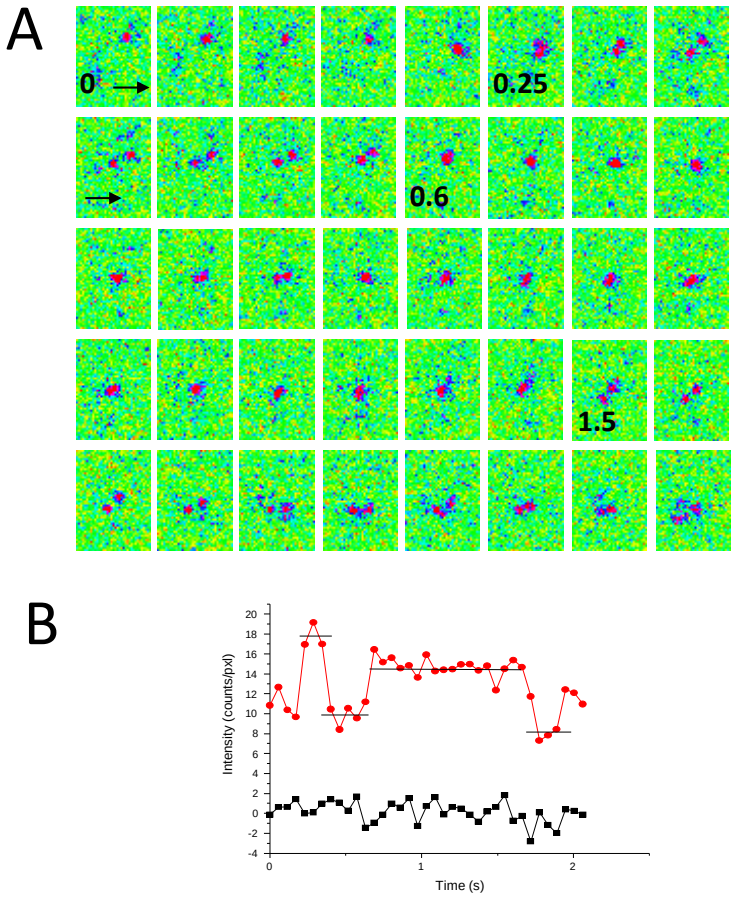

Figure 2.8: (A) Dynamic visualization of two LPS molecules reversibly switched states between singlet and doublet. A total of 40 consecutive frames are shown in top-to-down rows (50ms per frame), the tracing started with one molecule which was joined with the second one at 0.25s and the they split temporarily apart, but reunited as one for ∼0.9s until they separated again and both disappeared from detection in the later time frames (not shown here). (B) Intensity profile of a single particle (red) to show the intensity doubling upon merging. Note that the signal was increased or reduced in a step-wise manner.

2.2.4 Discussion and outlook

Single-molecule fluorescence imaging is widely used to study the localization and dynamics of single protein in living cells. By SMLM, TLR-4 has been shown already pre-clustered in the unstimulated primary human macrophages[90] and gliomas cells[160] in the diameter of 50 nm. Although no higher order of TLR4 clustering was found in HEK293 cells, ∼58% of TLR4 are dimerized in the presence of MD-2 and CD-14, and the ratio between monomeric and dimeric states changes depending on the LPS chemotypes[64]. These elegantly conducted experiments were, however, based on the fixed cells. In attempt to visualize the dynamic process of clustering by fluorescent LPS probes, I chose the single-molecule tracking approach. Unfortunately, it is sensitive to photobleaching and photoblinking. The former limits the tracking duration in the time scale of seconds and the latter simply breaks the continuity of tracing. Hence, it would be very valuable to allow single-molecule tracking in an extended timescale. For instance, the longer recording of bound LPS movement on the plasma membrane should help understand if they cluster in a particular region where they are brought in contact with TLR4 and facilitate the dimerization of receptor complex before the internalization occurs. A reducing-plus-oxidizing medium implemented for cells under low dissolved oxygen might help suppress the photobleaching/blinking events and extend the tracking period[139], or the use of quantum dots for LPS labeling is also an alternative for extended recording.

As for the TLR4 labels, the introduction of tag proteins (Halo[75] or SNAP[62]) that fuse to targets of interest has been useful tools for live imaging. These are the small enzymes which catalyze the fluorescent substrates that can diffuse into the living cells. Given that the labeling ratio is restricted to kinetic activity of the enzymes, therefore the incomplete labeling can result in the selective observation of single fluorescent molecule tracking. In addition, light-induced photoactivated or photoconvertible fluorescent proteins[73] were reported for single-molecule tracking, called sptPALM. In the case of using mEOS3.2, they originally emit photons in green color prior to the photoconversion via UV light. By illuminating with UV in the first step of repetitive recordings, the emission spectrum is shifted to orange and a fraction of such emitters can be imaged with reasonably well-separated PSFs until they are bleached or switched to off-state. The entire acquisition scheme can be repeated to image another subset of molecules from the entire population. This is the temporal approach to record single fluorescent molecules under reduced

density for tracking. Indeed, the mEOS2 was introduced to visualize the TLR4 dimerization in response to different LPS chemotypes[64]. In combination of the above mensioned labeling techniques, it might be possible to simultaneously localize the TLR4 receptor and the fluorescent LPS and is thus able to address the receptor-ligand interaction *in situ*.

2.3 Fluorescence imaging of LOS

*This section is largely based on the peer-reviewed publication[147].

The application of fluorescent LPS on various microscopic techniques have been shown in the previous chapter, it is proved that a well-conjugated ligand can be a powerful tool for imaging. However, it is not the same case for LOS which lacks the O-antigen part of LPS to which the fluorophores normally tagged. Hence the labeling on LOS is still undocumented and should otherwise provide useful complementary information. We decided to use cyanine-based fluorophores widely used in protein labeling for microscopic imaging[157] and in particular Cy7 derivatives known for their fluorescence in the near-infrared region (NIR), where they provide excellent contrast on biological samples[6]. The cyanine fluorescent scaffold has already been used for a number of imaging applications including intracellular pH determination or ion sensing[36][129][163], as contrast agent for surgery[92], and for cancer detection and therapy[83][124][155]. However, Cy7 dyes suffer some inherent drawbacks, such as a very small Stokes-shift, which makes imaging experiments more difficult.

Here, we explored the possibility to exploit the far-red fluorescence emission of the aminoheptamethine fluorophore (Cy7N), featuring a larger Stoke-shift (Δ= 3440cm^{-1}), where the intense fluorescence of Cy7N is emitted in the far-red to NIR and consequently enables the bioimaging experiments in the optically transparent spectral window where absorption and scattering of incident light is minimal[55][99].

2.3.1 Synthesis of Conjugatable CDE-Cy7N.

The Cy7N fluorophore was designed by introducing sulfonate functions to optimize their solubility in biological media, while the rigidity of the heptamethine skeleton was ensured by a tertbutylcyclohexenyl framework to reduce the fluorescence losses by nonradiative deexcitation [96]. The synthesis of the reference aminoheptamethine Cy7N (4) and carboxyldiethylenglycolamine (CDE)-functionalized Cy7N (6) was carried out using classical conditions [99][97]. Briefly, the preparation starts from 2-Chloro-l-formyl-3-hydroxymethylenecyclohexene (1) reacting with indolinium salt (2) and gives rise to the base of chloroheptamethine dye (3), which in turn was substituted in the presence of n-propylamine or 2-[2-(2-

aminoethoxy)ethoxy]acetic acid (5) in DMF to synthesize dyes 4 and 6 as blue solids in 45% and 25% yields, respectively (Figure 2.9).

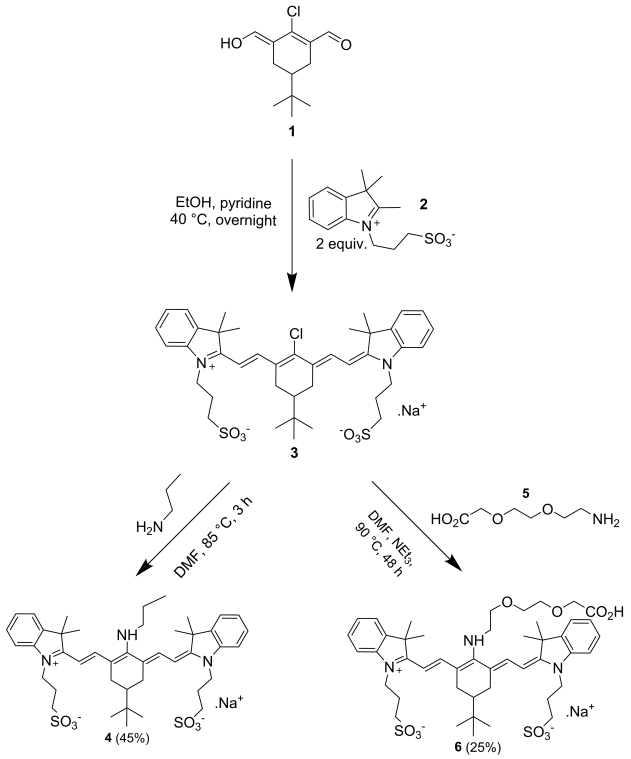

Figure 2.9: Scheme 1: Synthesis of the reference amino-heptamethine dye (Cy7N, 4) and the corresponding functionalized analogue (CDE-Cy7N, 6; MW =880.4).

The photophysical properties of this type of cyanine dyes were investigated in the reference fluorophore Cy7N (4), and its absorption and fluorescence spectra were recorded in water (Figure 2.10A). The chromophore presents a broad absorption band centered at 605 nm and an emission in the far-red range, characterized by a particularly large Stokes shift (ca. 3440 cm^{-1}). The fluorescence quantum yield is however noticeably decreased in water, as it was already reported for analogous polymethine derivatives[96]. The introduction of functional group on CDE-Cy7N 6 has no influence on the optical properties which gains the opportunity of two-color labeling in combination with Cy5 (Figure 2.10B) [34]. This is the benefit from its design that its fluorescence trespasses beyond the Cy5 emission spectrum, it thus

permits a useful approach to collect both cyanine dyes with a single excitation line, for example, a Helium-Neon laser at 633nm.

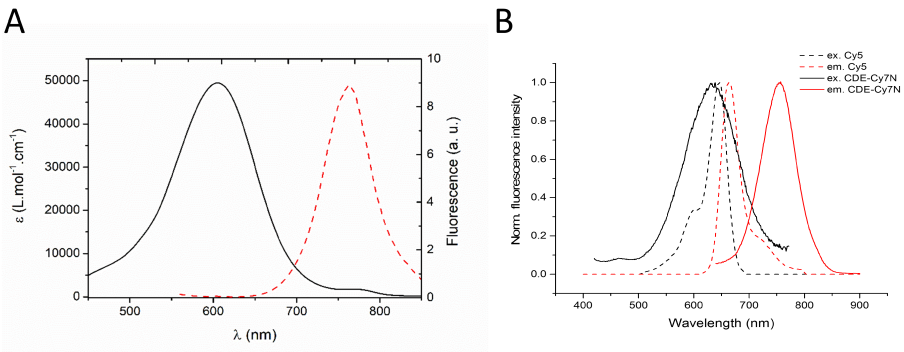

Figure 2.10: (A) Absorption (black, plain line) and fluorescence (red, dashed line) spectra of 4 in water. λabs = 605 nm; λem = 764 nm; ϕfl = 0.06. (B) Spectral comparison between Cy5 and CDE-Cy7N. The former spectra were adapted from SpectraViewer (ThermoFischer) and the latter were acquired by the fluorometerVarian (Darmstadt, Germany)

2.3.2 Bioconjugation of CDE-Cy7N to LOS.

In this study, we used the approach of click chemistry to conjugate the CDE-Cy7N onto LOS extracted from the *E. coli* strain, MG1655 (Figure 2.11). The carboxyl group of CDE-linker was joined with the amines of LOS, in the aid of two catalysts, 1-ethyl-3-(3-(dimethylamino)propyl) carbodiimide (EDC) and sulfo-Nhydroxysuccinimide (sulfo-NHS). In brief, 10mg of extracted and purified LOS (1 equiv.) was dissolved in imidazole/HCl buffer (pH = 6.2). CDE-Cy7N 6 (5 equiv.) was added together with the condensing agent, EDC (5 equiv.), and a catalytic amount of the acyl-transfer catalyst NHS. The mixture was stirred overnight at room temperature, then extracted with dichloromethane and the aqueous phase was proceeded to recover the conjugation product, LOS-Cy7N.

2.3.3 Stoichiometry of CDE-Cy7N to LOS.

The attachment of CDE-Cy7N to LOS has been designed to be site-specific on the ethanolamine groups on KdoII or HepI phosphates (Figure 2.12). To pre-

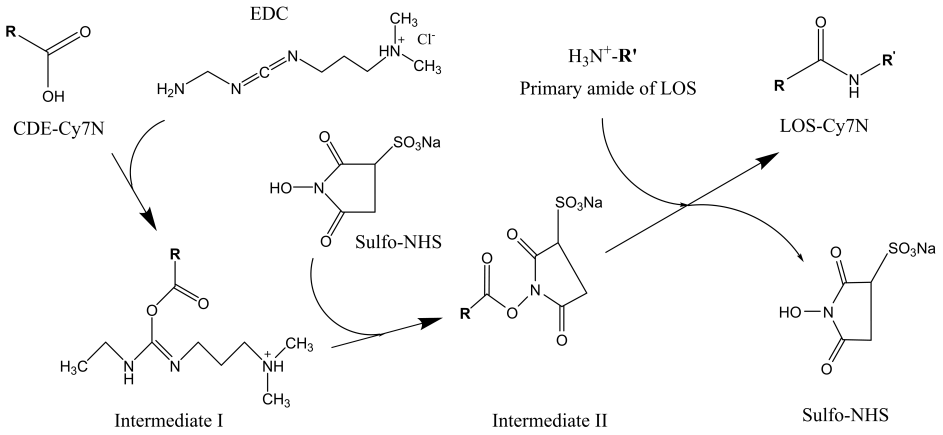

Figure 2.11: Scheme 2: EDC-NHS chemistry for dye conjugation. The CDE-Cy7N has a carboxyl linker to react with EDC, forming the first intermidiate which may react with sulfo-NHS, yielding an amine-reactive NHS ester as the second intermediate. The NHS-ester is prone to react with amines on the suger backbone of LOS (see Figure 2.12), it thus facilitates the EDC-mediated Cy7N-LOS coupling reaction.

cisely understand the stoichiometry of dye conjugation (i.e. one or two Cy7N dyes conjugated per LOS molecule) in our final product, we performed the following purification steps to clarify the question. The analyte from the aqueous phase of the overnight reaction was purified by chromatography using two consecutive PD-10 columns. The purity of the conjugate was assessed by SDS-PAGE (Figure 2.13A and B). From the gel electrophoresis analysis, we have obtained evidence of one or two Cy7N-labeled constructs based on the identification of the higher molecule weight shifts after eluting from the first column (Figure 2.13A). However, the eluent was still contaminated with input LOS which may potentially interfere with Cy7N-conjugated ones, especially for the biological applications performed later. Hence, the eluent was further purified with the second column to totally remove unconjugated LOS from the final conjugate, LOS-Cy7N (Figure 2.13B). It is, however, at the expense of losing double-conjugated product as only single-labeled conjugate was collected at the end of the second purification.

To further investigate the stoichiometry of the LOS-Cy7N conjugates, the effective attachment of one CDE-Cy7N to the core saccharides (OS) has been determined by MALDI mass spectrometry (MS) analysis of the LOS-Cy7N in com-

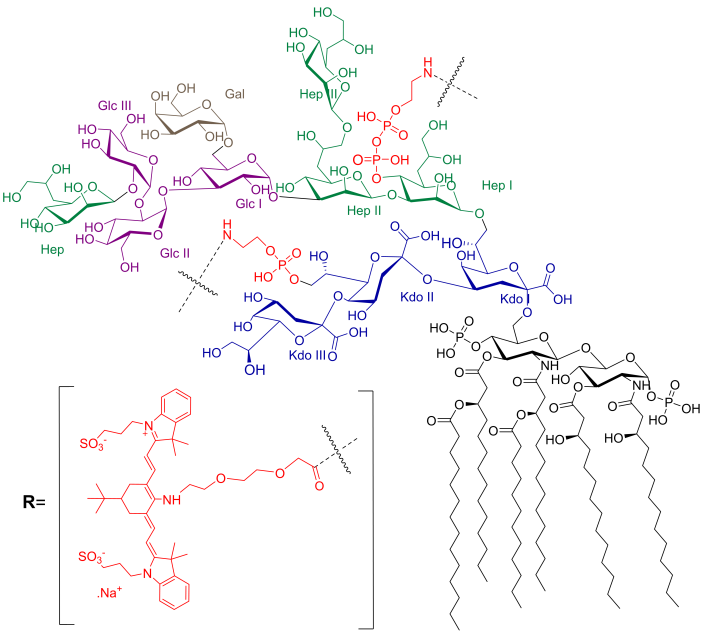

Figure 2.12: Chemical structure of LOS revealing two conjugation sites for attaching the CDE-Cy7N to the monophosphoethanolamine of either Kdo II or Hep I.

parison with the underivatized *E. coli* LOS (Figure 2.13C). In both spectra, the typical ion peaks of core OS and lipid A, originated from the cleavage of the labile glycosidic bond between Kdo and the lipid A moiety, were clearly detectable. The observation in the spectrum of the LOS-Cy7N (Figure 2.13C, bottom) indicated an additional peak at m/z 3264.1 corresponding to molecular weight of the OS plus one unit of CDE-Cy7N, thereby verifying the successful dye conjugation on LOS in 1:1 ratio.

2.3.4 Photophysical property of LOS-Cy7N

Since the chemical property of the conjugation has been fully assessed as mentioned above, we would like to know its photophysical property as well, especially

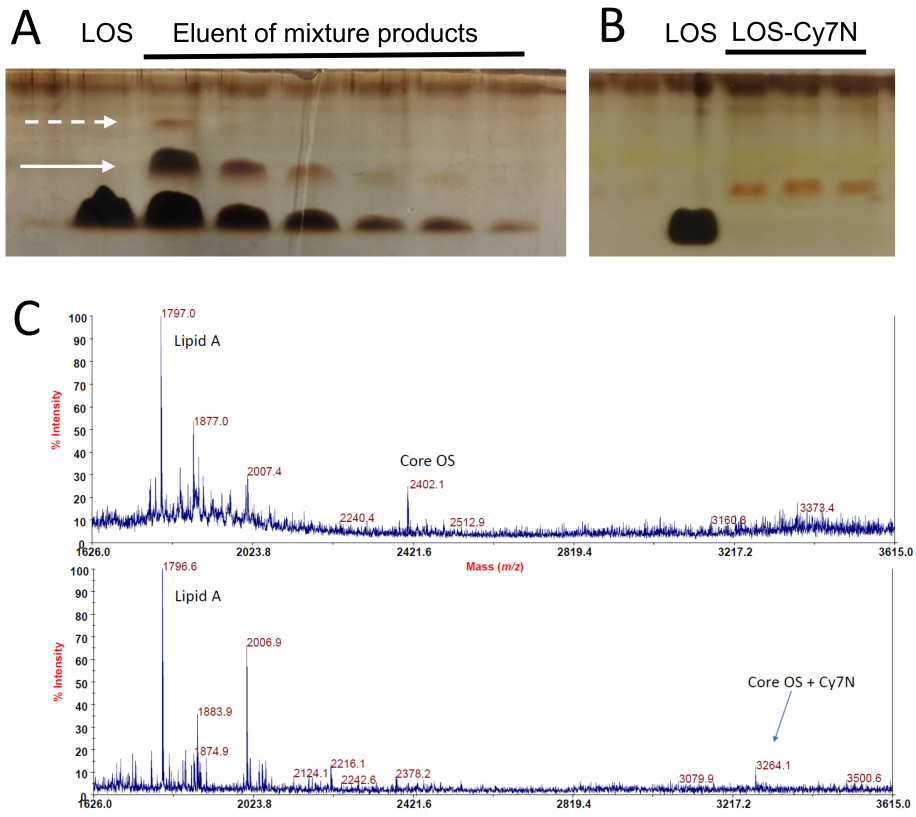

Figure 2.13: Gel electrophoresis of the eluent from the initial (A) and second (B) chromotagraphy revealed by silver staining. Note that the LOS was loaded as the control to show a single band on the first lane, followed by a serial collection of eluent fractions which contain not only the unconjugated LOS, but also single-(solid arrow) or double-labeled LOS-Cy7N (dashed-arrow). The mixture eluent in A was cleaned up with the second PD-10 column (B), and analyzed by MALDI mass spectrometry. (C) Top: Zoom of the negative ion MALDI MS spectrum of native LOS showing the peaks corresponding to the lipid A and core OS species, while the spectrum of the LOS-Cy7N shows the additional peak of single-labeled LOS-Cy7N conjugate.

when it applies to the biological specimens. We thus used spectral scanning capability of the confocal microscope, in which the combination of supercontinuum laser and the spectral detection was exploited to characterize the excitation and emission spectra of the final conjugate, LOS-Cy7N (Figure 2.14) from the living cells. Surprisingly, the emission spectrum obtained from cell-bound LOS-Cy7N was blue-shift approximately 50nm as compared with unconjugated free dye. This

can be explained by its sensitivity to acidity change as some cyanine-based fluorophores are designed as the pH sensors[129]. Therefore, the emission spectrum of LOS-Cy7N may be slightly different when they are taken into cells and reside in the endosomes or lysosomes where the acidity rise in favor of the enzyme activity.

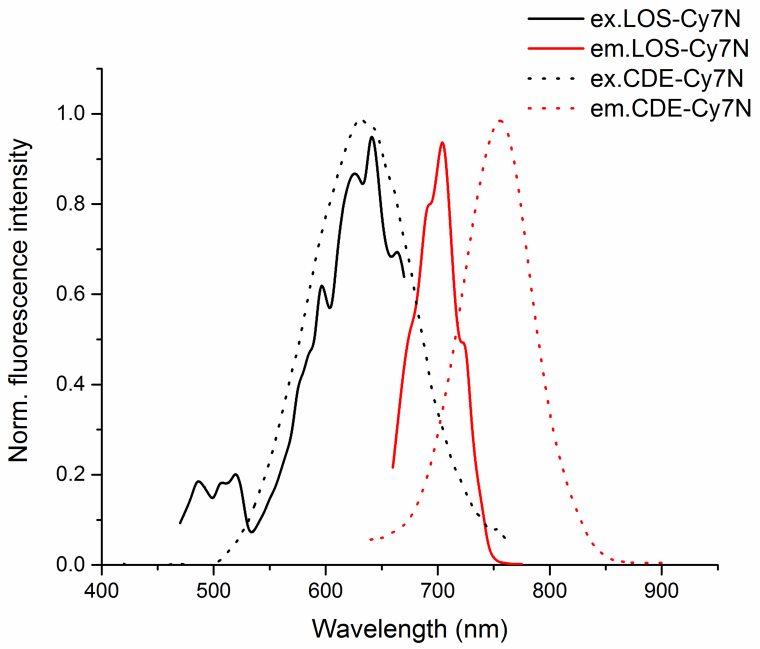

Figure 2.14: Normalized excitation (ex) and emission (em) spectra of CDE-Cy7N and Cy7N-LOS bound to living cells. 1mg/mL of CDE-Cy7N solution was used to measure the excitation and emission spectra on a spectrophotometer. On the other hand, the spectra of Cy7N-LOS were assessed directly on the confocal scanning microscope. The excitation curve was obtained by changing excitation laser lines (470-670nm) in constant power mode while the fluorescence signal (690-800nm) was detected in the photon-counting mode of the hybrid detector (HyD) with pinhole size set to 2 Airy disk units. The emission plot was obtained with a fixed 633nm laser line and the signals were collected by 5nm stepwise movement of detection sliders and the intensity was corrected by the quantum efficiency of the HyD.

2.3.5 Evaluation of LOS-Cy7N Bioactivity

The bioactivity of LOS-Cy7N in terms of its capacity to activate TLR4 was assayed on HEK-Blue hTLR4 reporter cells. This cell line provides stable ex-

pression of all proteins of the TLR4 receptor complex, namely, TLR4, MD-2, and membrane-bound CD14, and an inducible secreted embryonic alkaline phosphatase (SEAP) reporter gene placed under the control of transcription factors NF-κB and AP-1. The activation of TLR4/MD-2/LOSCy7N induces the activation of NF-κB and AP-1 leading to production and secretion of SEAP in the cell culture media. The levels of SEAP can easily be determined by incubating the enzyme with the substrate, para-nitrophenyl phosphate (pNPP).

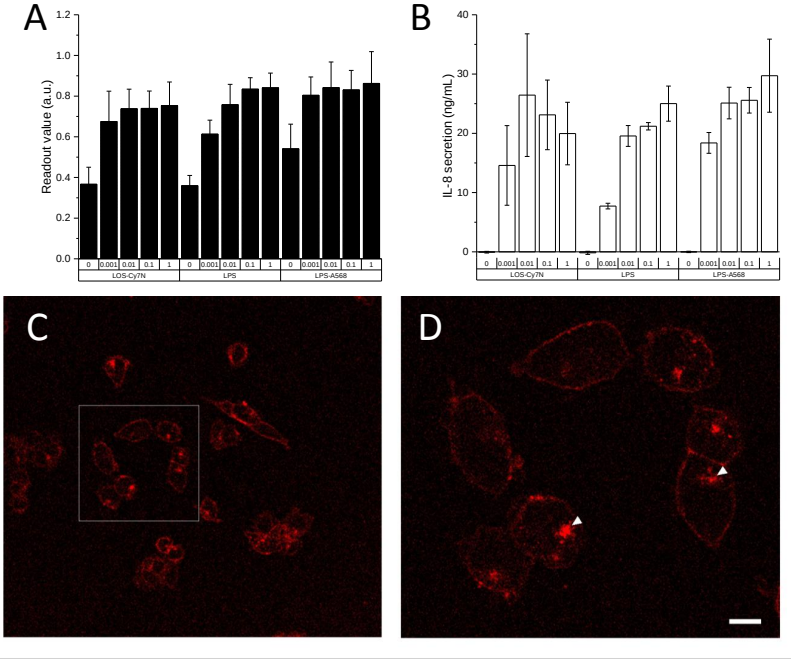

Figure 2.15: (A,B) Immunoreactivity of LOS-Cy7N, LPS-A568 and native LPS were assessed by using the HEK-blue reporter cells. Secretion of the reporter enzyme, pNPP, (A) and interleukin-8 (B) were determined by light absorption. (C,D) Confocal microscopy images of LOS-Cy7N-treated HEK blue cells. (C) Fluorescent signal of single optical section was detected and the cells of typical staining patterns are highlighted in the outlined box and shown in (D). Note that the uptaken fluorescent LOS was observed in the juxtanuclear area (arrowheads) of the cells. Scale bar= 10 μm.

Cells were treated with increasing concentrations (10^{-3} to 1μg/mL) of LOS-Cy7N together with the commercial available ultra-pure LPS and Alexa 568-labeled LPS, and the SEAP levels were quantified after 16 h of incubation (Figure 2.15A).

The result showed comparable dosage-dependent trend of increasing gene expression driven by endotoxin-induced transcription factors, which represents the immunotoxicity of individual endotoxins. Alternatively, the cell activation can also be evaluated by the detection of cytokine secretion. In this study, the interleukin-8 was analyzed by enzyme-linked immunoasorbance assay (ELISA) (Figure 2.15B). The presence of interleukin-8 released after cell exposure to individual endotoxins proved once again that the potency of our LOS-Cy7N to induce immune responses is retained after chemical conjugation.

Furthermore, the fluorescent signal of LOS-Cy7N was found not only on the plasma membrane but particularly concentrated in the perinuclear area, which is presumably the Golgi apparatus (Figure 2.15C and D). Similar results were obtained with purchased LPS-Alexa 568, and the binding specificity of LOS-Cy7N was also tested by incubating cells with excess of free Cy7N dyes, which showed only weak noises (data not shown). The results suggest that the Cy7N near-infrared dye is for the first time successfully conjugated to the bacterial LOS and demonstrated that they are useful for the microscopy study of the endotoxin uptakes in cells.

2.3.6 Endocytosis of Cy7N-Labeled LOS.

LOS-Cy7N was tracked in cells through confocal fluorescence microscopy. To observe the presence of LOS-Cy7N, we transiently expressed CD14 in HEK-293T cells because the introduction of CD14 in this cell type was required for cell binding of fluorescently labeled LPS[69][51] and also for the subsequent endocytosis that starts the inflammatory cascade[159][132]. Within 1 h of incubation, the fluorescent signal of LOS-Cy7N was found in CD14-positive cells which were immunolabeled with the corresponding antibody, but not in the cells which did not express CD14 after transfection (Figure 2.16A). This observation strongly suggests that LOS retains its ability to bind CD14 after conjugation with cyanine and the internalization of the LOSCy7N is CD14-dependent. At a single cell level, LOS-Cy7N was noticeably found on the plasma membrane, although primarily in the internalized vesicles (Figure 2.16B). This suggests that CD14 promotes the uptake of LOS-Cy7N into the early endosomes.

For comparison to previously reported fluorescent ligands, we used Alexa488-labeled LPS as a control, with which the cells were treated in the same conditions as LOS-Cy7N. Although the binding of LPS-Alexa488 was also found on the CD14-

expressing cells, it was mainly localized at the cell surface, without entering into the cells (Figure 2.16C), whereas LOS-Cy7N was readily taken up by the cells and internalized (Figure 2.16B).

Therefore, a striking difference of the localizations between fluorescent LOS and LPS was found, indicating that LOS-Cy7N appears to be internalized faster than LPSAlexa488 upon cell treatment. To directly compare the uptake events of the two fluorescent endotoxins, we then treated the cells with both fluorescent endotoxins and observed their interactions with the cells by the time-lapse imaging. Within a short period of incubation, LOS-Cy7N was partially translocated into the cells in contrast to the cell surface localization of LPS-Alexa488 (Figure 2.17A), which was then slowly internalized at later time points (Figure 2.17B). The cotreatment experiment thus indicated that while both fluorescent endotoxins followed the same steps toward cell internalization, the endocytosis of the LOS-Cy7N took place earlier than that of LPS-Alexa488. This may imply that different uptake mechanisms are used for each type of endotoxin molecules.

Finally, we are also interested in understanding the vesicle transport of internalized LOS-Cy7N. It is known that once LPS is internalized it undergoes the endocytic pathway to be processed and degraded in lysosomes, and this step is important for signal termination[51]. To see if LOS-Cy7N follows the same route, cells were treated with LOS-Cy7N and LysoTracker Green (Figure 2.17C). Here, we also identified that a subset of the endocytosed LOS-Cy7N was indeed colocalized with the lysosomal marker, which indicates that they were sorted to lysosomes for detoxification.

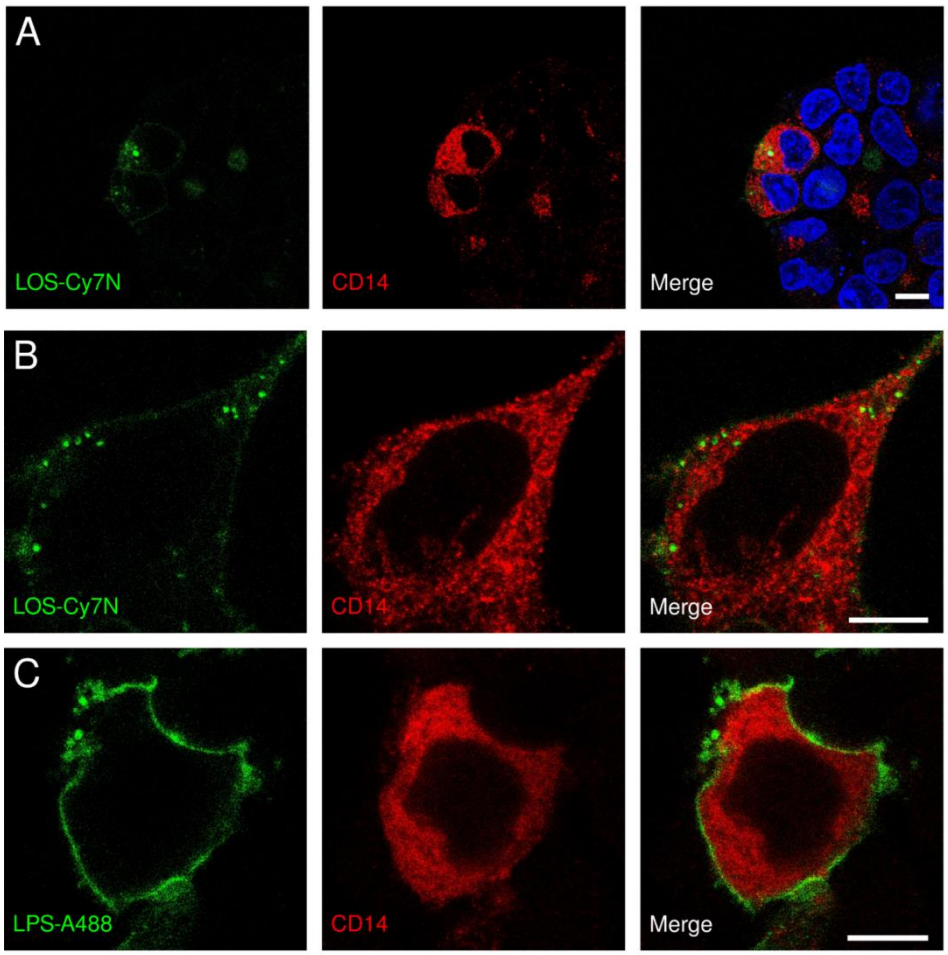

Figure 2.16: Specific binding of LOS-Cy7N and LPS-Alexa488 to CD14-transfected HEK-293T cells imaged by confocal fluorescence microscopy. (A) Cells were treated with LOS-Cy7N for 60 min, fixed, immunostained with anti-CD14 antibody, and counterstained with DAPI. Note that LOS- Cy7N is visualized on two CD14-expressing cells whereas it is absent in other cells revealed by DAPI staining of the nuclei. (B) Same treatment as in A, but with higher magnification on a single cell. The cell surface-bound LOS-Cy7N is found rapidly internalized into the CD14-immunopositive cells as endosomal vesicles. (C) Cells treated with LPS-Alexa488 for the same incubation time showed fluorescence signal mostly resided on the plasma membrane and formed extracellular vesicles via possible exocytosis. Scale bar = 10 μm.

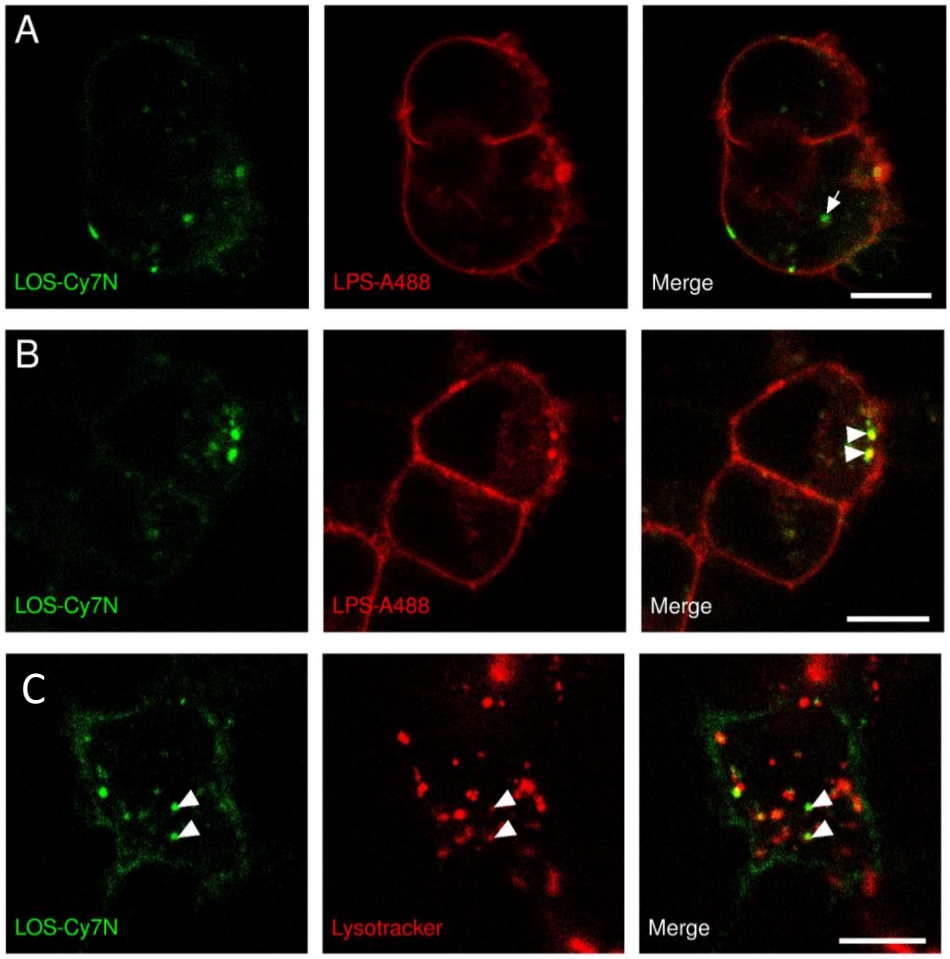

Figure 2.17: Confocal microscopic images of the transfected HEK-293T cells cotreated with LOS-Cy7N and LPS-Alexa488 for 30 (A) and 120 min (B). (A) LOS-Cy7N appeared to be faster internalized in the absence of LPS-Alexa488 (arrow). (B) However, LPS-Alexa488 can be later found in cells with prolonged incubation and they, if not all, colocalized with LOS-Cy7N in vesicles just beneath the plasma membrane (arrowheads). Note that fluorescent ligands are not homogeneously distributed on the cell surface, they instead appear as organized domain structures which are more pronounced for LOS-Cy7N. (C) Subcellular localization of the internalized LOS-Cy7N. Cells were first treated with LOS-Cy7N for 60 min, briefly washed with PBS, then incubated 5 min with the lysotracker before imaging. The arrowheads depict the colocalization of LOS and lysosomes. Scale bar = 10 μm.

2.3.7 Discussion and outlook

Since only a minute amount of LPS can induce a violent reaction in the immune system, it is of importance to understand the physiological reactions of LPS by which it affects the biological function of the infected cells and tissues. Several labeling approaches have been used, among which the fluorescence probes were shown its usefulness on detection of the LPS receptor binding and molecular interactions of the cofactors by cell cytometry[156][138][137] or the microscopic observations of LPS distribution in cells[135] and mice[26]. Despite that many fluorescent organic dyes have been reported to achieve the aforementioned studies, they typically fluoresce in the visible range where fluorescent signals are often suffered from autofluorescence existing in the biological specimens. By contrast, quantum dots produced in nanometer-range size offer far more intense and photostable signal, but they are labeled by hydrophobic interactions between the metal surface of nanoparticles and the lipid A part of LPS[12][84]. This conjugation strategy is not based on the covalent binding, and in case of dissociation from the ligands the nanoparticles may not only fail to report the location of LPS, but also exhibit the intrinsic toxicity to cells and organs. A new fluorophore which can practically circumvent the application problems is thus urgently needed. Moreover, the conjugations of fluorescent agents were reported so far only on LPS, by which the fluorophores were chemically attached to the hydroxyl groups of O-antigen which is absent in LOS, therefore the labeling on LOS is still undocumented before this study.

In the present study, Cy7N was functionalized with a carboxyl diethylenglycolamine (CDE) linker to label LOS endotoxin through the reaction with a nucleophilic phosphoethanolamine group on LOS to obtain the fluorescently tagged LOS-Cy7N conjugate for in vitro microscopy studies. Cy7N was chosen for its particularly interesting photophysical properties[157][37] such as featuring sulfonate side-chains that provide good solubility in aqueous media which is a critical parameter for imaging. Importantly, the central amino substitution confers optimal optical properties such as a significant Stokes shift and strong emission in the biologically transparent spectral window, which are highly beneficial to improve imaging contrast with the possibility to functionalize the central cyclohexene moiety with linkers containing terminal reactive groups for subsequent bioconjugation.

The use of Cy7N-labeled LOS enables us for the first time to explore its cell binding, internalization, and vesicle transport in single cells and compare it with fluorescent LPS. We have found the faster internalization of LOS compared with

LPS (Figure 2.18). The molecular mechanism of the CD14-mediated endocytic pathway is, however, less well understood: tyrosine kinase Syk and PLCγ2 are involved as downstream effectors for LPS-induced endocytosis of TLR4[132]. Both clathrin and dynamin were proposed for the formation of LPS-internalized vesicles [51][63]. It remains to be investigated if the abovementioned mechanisms also apply for LOS or if other molecular events facilitate the internalization of LOS faster than LPS.

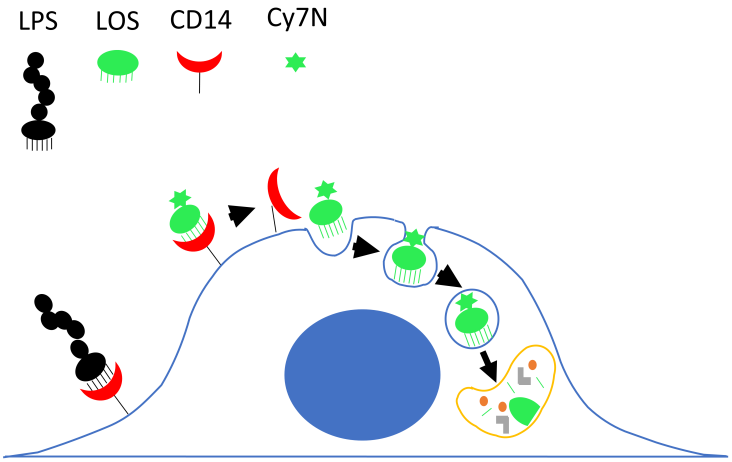

Figure 2.18: Schematic illustration of the CD14-mediated cell surface binding and internalization of LOS which is eventually detoxified in lysosomes.

Interestingly, the formation of internalized endotoxins in early endosomes provides a second signaling source other than the MyD88-dependent pathway, initiated by the assembly of adaptors TRAM and TRIF[58][133]. These adaptors mediate the activation of the transcription factor interferon regulatory factor-3 (IRF3), which regulates type I interferon (IFN) expression[4]. Since the LOS-Cy7N could be detected intracellularly, while LPS remained in the plasma membrane, the timing of signal triggers may result in different cell responses upon stimuli. For instance, LOS-induced cytotoxicity may largely rely on endosomal signaling rather than MyD88- dependent signaling and thus promotes different cell reactions in the initial phase of cell activation (Figure 2.19). In fact, different modes of actions taken between two types of endotoxins have shown that the LOS can activate inflammasomes in dendritic cells in the absence of other accessories which are otherwise required for LPS[158].

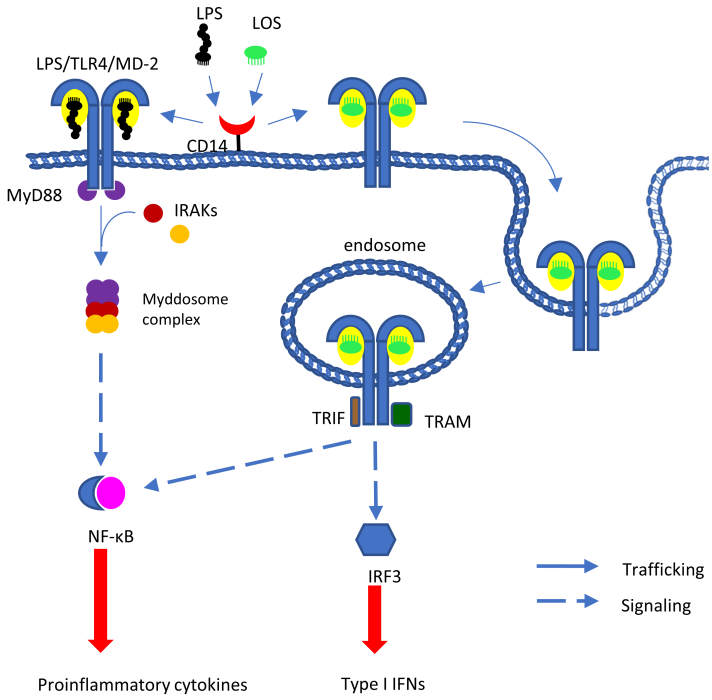

Figure 2.19: Proposed cell signaling preferences between LPS and LOS based on their individual trafficking pathways in the early stage of cell activation. Endotoxin ligands (i.e. LPS/LOS) initiate cell signaling through the binding of CD14 on the cell surface, which facilitates the delivery of LPS/LOS to individual TLR4/MD-2 receptor complex. In this study, the LPS receptor complex may transduce early response through the MyD88-dependent recruitment of IRAKs and form the myddosomes which relay downstream signal to promote cytokine production. In contrast, the rapid uptake of LOS may suggest the signaling mainly comes from the internalized receptor complex in endosomes where TRIF and TRAM are required for interferon expression and the delay of NF-κB activation.

Ectopic expression of CD14 in HEK-293T cells proved to be essential for both surface binding and subsequent internalization of LOS-Cy7N, of which the non-transfected cells are not capable. We did not observe co-internalization of both CD14 and LOS-Cy7N, most likely because CD14 was predominantly produced in the soluble form in the cytoplasm. We assume that only a limited amount of CD14 was linked to the glycosylphosphatidyl inositol (GPI) linker to be anchored to the plasma membrane, where its presence is overwhelmed by cytoplasmic CD14

and thus beyond the detection of a single optical section as seen by confocal microscopy. Therefore, TIRF microscopy might provide a better contrast to visualize the mCD14 and its colocalization with fluorescent endotoxins can be clearly determined. Interestingly, a similar study was conducted by introducing mCD14-EGFP to U373 cells, where its expression occurred predominantly at the cell surface. The authors found, however, that the internalized BODIPY-LPS did not colocalize with mCD14-EGFP, suggesting that mCD14 did not accompany LPS during endocytic movement[144]. Such a phenomenon would likely depend on the specific cell types because LPS-induced CD14 internalization was previously shown in macrophages by flow cytometry[132]. However, the question of whether mCD14, at least in imaging-based studies, is internalized together with the TLR4-LPS receptor complex or not, requires further investigation.

2.4 Fluorescence imaging of lipid A

2.4.1 Lipid A moiety as immunomodulators

As mentioned above that bacterial endotoxins act as molecular signals of microbial invasion. The signal is generated upon the recognition by TLR4 which triggers innate immunity response in the host, creating the cytokine cascades that regulate the behavior of the phagocytic cells to counteract the infection. However, researchers also discovered that the antagonistic LPS extracted from *Rhodobacter sphaeroides* can bind to TLR4 monomers but prevents them from forming receptor dimers, thereby blocks the TLR4 signaling[74]. To this sense, one can modulate the immunoreactivity with agonists/antagonists that structurally resemble the endotoxin. Particularly for the small molecules designed to mediate the TLR4 activation, they have great therapeutic potential as vaccine adjuvants or anti-inflammatory agents[101].

In fact, the lipid A part of bacterial endotoxins are ideal candidates for this purpose as they can solely activate the TLR4-induced immune defense. The response is highly dependent on the structural features of lipid A, such as the number of phosphate groups on GlcN disaccharides as well as the number and length of the acyl chains. Therefore, the structural mimicry of lipid A has been used to modulate the TLR4 signaling. Among which the semi-synthetic lipid A derivatives are

proposed to be a new type of adjuvants to elicit an enhanced and long-lasting immune response to vaccines[19]. They are thus termed immunoadjuvants that were used together with toxicity-reduced pathogens in boosting the immune response to generate antibodies against pathogens that our body may confront later in life.

2.4.2 Fluorescent labeling of lipid A moiety

In this study, the lipid A with two phosphates are potent immunoactivator of TLR4, whereas the monophosphoryl lipid A is considered as a nontoxic immunoadjuvant with a mild immunostimulatory effect[19]. Both were tagged with the fluorophores, nitrobenzofuranzan (NBD) for the fluorescence light microscopy imaging. The general structure of lipid A was obtained starting from an optimized fed-batch fermentation procedure for the gram-scale production of lipid A from *Escherichia coli* K4 and a suitable phenol-free protocol for its purification, and then site-specific synthesis was performed to achieve the designated modification of lipid A as a result of the monophosphoryl and diphosphoryl lipid A, hereafter termed as LAMP and LADP, respectively (Figure 2.20). Both are tagged with a nitrobenzofuranzan (NBD) fluorochrome through a suitable linker on the C6 position of the GlcN II. We aim to observe the staining of two fluorescent lipid A in the cells on the deconvolution microscope.

2.4.3 Deconvolution images of fluorescent lipid A

Two cell lines were used to test if the fluorescent lipid A can bind and reactive to the immune cells. The first one is the HEK blue cells which are commonly used in the immunological studies and they have the complete receptor complex (TLR4/MD-2/CD14) in response to the LPS stimuli. Cells were grown on glass-bottom chamber slides and were incubated with the indicated concentration for one hour before they were fixed with paraformaldehyde and kept in PBS prior to the imaging on the deconvolution microscope. LPS conjugated with Alex568 was used as a positive control to reveal the membrane staining and also the punctate structure which indicated the uptake of fluorescent LPS in the endosomal vesicles (Figure 2.21A). Two types of fluorescent lipid A , LAMP and LADP, were individually applied on cells (Figure 2.21C, D respectively), while the NBD fluorophore was used for negative control (Figure 2.21B). Please note that with the same amount of

NBD, approximately 176 KDa, the dosage of the dye is ten times more than that of individual lipid A, yet it shows minimal background noise. On the other hand, both types of lipid As show positive staining on the HEK cells but most surprising is that the LAMP form has far strong signals found in the cytolasm of nearly all treated cells, while the LADP has weaker intensity in overall cell population but still a few cells were found to be preferentially reactive. Moreover, the same results were also obtained from another cell line, J774 macrophages (data not shown).

2.4.4 Discussion and outlook

The results indicates that both types of lipid As are reactive to the tested cells, though the LAMP has a relatively higher binding affinity, which can be possibly explained by the higher conjugation ratio revealed on the MALDI-TOF mass spectrum (personal communication). Although the LAMP has brighter staining, the fluorophore, NBD, was fast bleached by the LED illumination during the image acquisitions. It would be technically difficult for the superresolution microscopy in which the fluorophore will be bleached even faster by laser excitation. To exchange the current fluorophore with other photostable dyes would be beneficial for further imaging of live-cell recording and more applicable for SR-SIM. Nevertheless, the preliminary data showed the potential of using small lipid A constructs to act as the immunoadjuvants that help stimulate the cell immunity for vaccine generation useful in clinical applications.

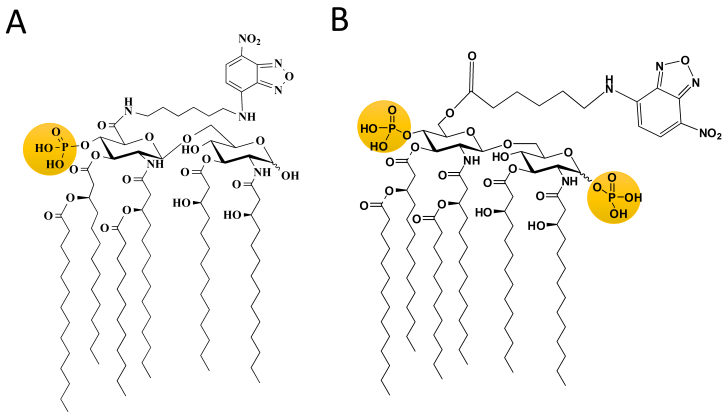

Figure 2.20: Chemical structures of NBD-labeled LAMP (A, MW=1993.68) and LADP (B, MW=2074.61). Two lipid A derivatives were semi-synthesized. One of them has single phosphate on the sugar back bone of lipid A (LAMP), while the other has two phosphate (LADP). Both of which are conjugated with a NBD fluorophore through a linker onto the sugar base of lipid A. Drawing modified from Dr. Marcello Ziaco.

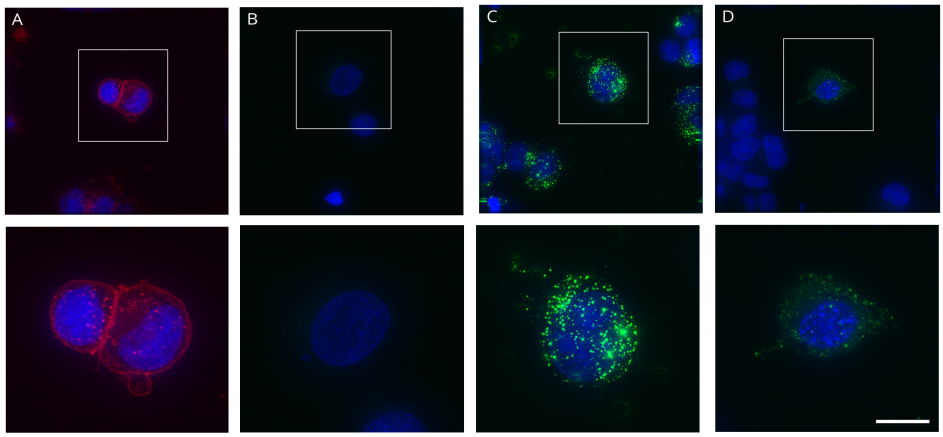

Figure 2.21: Deconvolution microscopy images of HEK-blue cells treated with various fluorescent endotoxins: 1μg/ml LPS-Alexa568 (A), 2μg/ml NBD (B), 2μg/ml LAMP-NBD (C), 2μg/ml LADP-NBD (D). Micrographs are maximum projection fromthe deconvolved 3D-stack images. The boxed regions are magnified to display the fluorescent lipid A moieties in single cells (lower row). Scale bar= 10 μm.

Chapter 3

Superresolution microscopy of inflammasome formation

3.1 Introduction of inflammasomes

In the previous chapter we have described an effective defense mechanism that warns neighboring cells when immune cells detect bacterial endotoxins. This mechanism leads to the release of pro-inflammatory cytokines that recruit other defender cells to the infection sites and eliminate the pathogens[11]. To take the action effectively, a cell needs to organize the signaling machine to generate a number of kinases and proteases within a short time. This task is attributed to the formation of a multiprotein complex named the inflammasome, which serves as a central signaling hub that regulates innate immunity. Since the discovery of inflammsomes was first reported in 2002[67], it sparked intensive research on its biochemical components, the control of caspases release and subsequent cell death, called pyroptosis[27][11]. Meanwhile it has also attracted our attention to investigate the formation of such supracomplex structure with superresolution optical microscopy. Our SR-SIM study here aims to provide insights into the mechanisms by which the formation of inflammasome is triggered in the activated macrophages and to resolve the architecture of the inflammasome formation with modern imaging analysis tools.

3.1.1 Inflammasomes and cell pyroptosis

Macrophages are the defender cells in our immune system, their main tasks are to detect the microbes or pathogens, "swallow" and disintegrate them into non-harmful materials, and thus to clear out the infected tissue. In the meantime, they also release the cytokines to induce a local inflammation site that speeds up the clearing of pathogens and the initiation of repair after tissue damage[11]. Two-signal model has been generally proposed to induce the release of inflammatory cytokines: First, activation of the Toll-like receptor (TLR) activator (e.g. LPS) leads to cellular priming and upregulation of NLRP3 and pro-IL-β expression, whereas the second signal comes from the assembly of an inflammsome where the caspase-1 is locally activated and able to process the pro-IL-β into active form. Meanwhile, the Gasdermin are also produced to form pores on the plasma membrane that not only facilitate the release of cytokines but ultimately leads to pyrotoptic cell death (Figure 3.1). Taken together, the formation of an inflammasome leads to three key cellular events: caspase-1 activation, IL-1β release, cell pyroptosis and none of these occurs without the inflammasome formation.

3.1.2 Structural assembly of inflammasomes

The structure of inflamassome is a complex assembly of the adapter proteins called ASC (apoptosis-associated speck-like protein containing a caspase recruitment domain). Prior to induction, ASC is diffusely located throughout the nucleus and cytoplasm. Once the inflammasome activity is initiated, nearly all ASC molecules are oligomerized into a single perinuclear aggregation. Because it appears as a shining spot under the diffraction-limited microscopes, it is thus named ASC specks[82]. ASC acts as building blocks of the inflammasome, the size of which is typically 1-3 μm in diameter. Moreover, the ASC aggregates, depending on their size, form rapidly within a few to tens of minutes until all free molecules are depleted from both the cytosol first and later from the nucleus[27]. Figure 3.2 shows an example of inflammasome formation in a macrophage cell expressing ASC-GFP in a time-lapse observation on the wide-field microscope. With regard to the fluorescence microscopic techniques for inflammasome study, not only the micron-size of single ASC speck is challenging the spatial resolution of conventional (or even confocal) microscopes, the rapid assembly also requires sufficient time resolution to monitor the entire process.

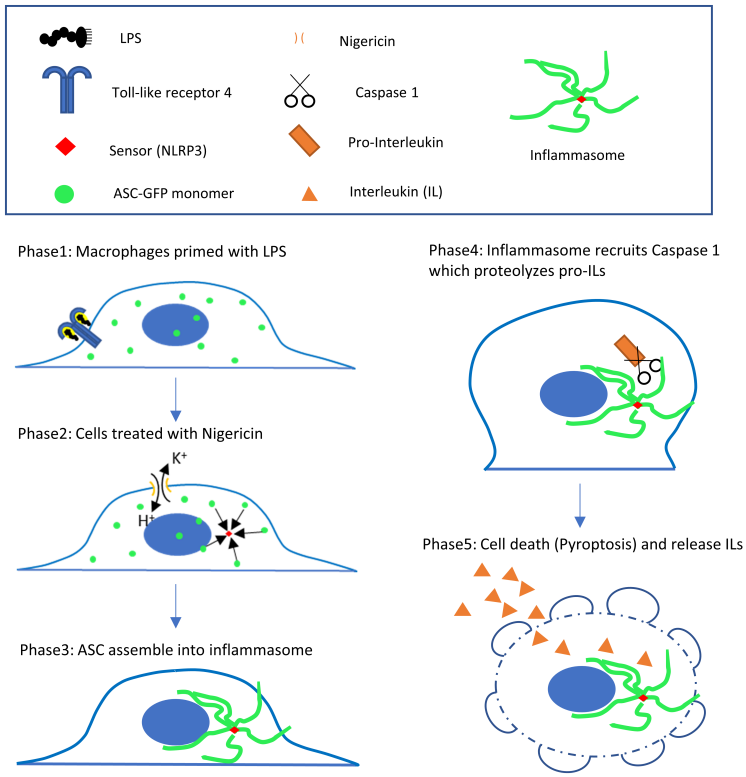

Figure 3.1: Schematic illustration of processes inflammasome formation which leads to the pyroptosis of macrophages. Macrophages were first primed with LPS for hours to overnight incubation before they are treated with nigericin which is another bacterial toxin that induces the efflux of potassium ions and the formation of inflammasome by a not-yet-understood mechanism. The assembly of the inflammasome is formed by the polymerization of soluble ASC molecules and it recruits caspase-1 which promotes IL-1β cytokine maturation and their release upon the pyroptotic cell death facilitated by the Gesdermin-aided disintegration of the plasma membrane.

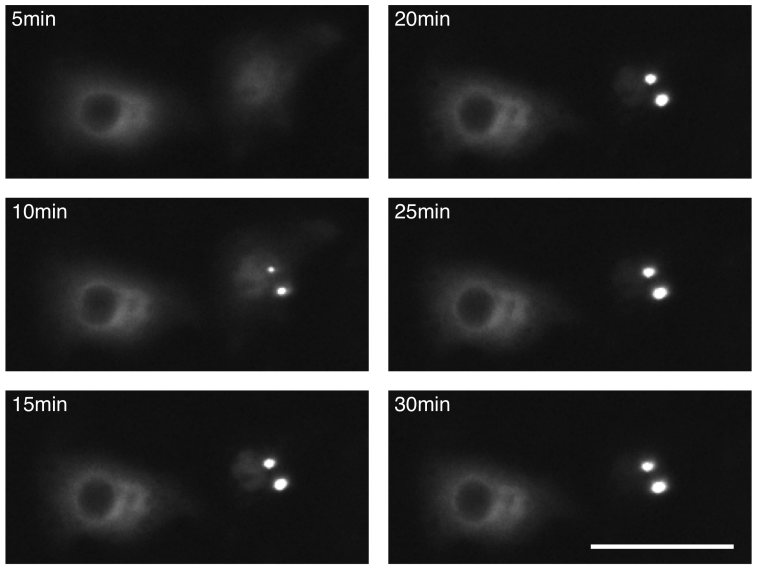

Figure 3.2: Wide-field time series recording of ASC-GFP speck formation. In some occasions two specks are developing simultaneously in one cell. The cytosolic signal started to fade away as the molecules are recruited into the growing specks till they are depleted from the cytoplasm, followed by the disappearance of ASC in the nucleus. Meanwhile the fluorescence intensity on the other cell does not decrease during the recording, indicating that the decay of fluorescence in the speck-forming cell is not the result of photobleaching. Time frames designated as minutes post-treatment of 5nM nigericin. Scale bar= 10μ m.

3.1.3 Architecture of ASC specks

The adaptor protein ASC bridges the sensor proteins and capase-1 to form ternary inflammasome complexes. ASC has two domains, the N-terminal pyrin domain (PYD) and the caspase-recruitment domain (CARD) in the C-terminus. Upon detecting foreign substances or danger signals the inflammasome sensor molecules nucleate the polymerization of soluble ASC into large helical filaments by facilitating PYD-PYD self-interaction. The CARD domain of ASC then recruits and activates pro-caspase-1 which is assembled around the ASC filaments[24]. Activate caspase-1 in turn induces the maturation of IL-1 family cytokines and also mediates their release into extracellular space[123]. Thus, ASC has an adaptor function that helps transduce the signals detected by the sensors to the downstream effector caspases. Since ASC is the major component of speck structure, its molecular conformation has been extensively examined by means of NMR, cyro-EM and X-ray crystallography [77][117]. The ultrastructure of ASC polymerization into long helical filaments revealed that the backbone of single ASC filaments (9nm) can be solely formed by its PYD-PYD homotypic interactions, while the CARD is exposed outward yet connected with a link hanging to the filament core in order to facilitate the interaction with effector caspases (Figure 3.3).

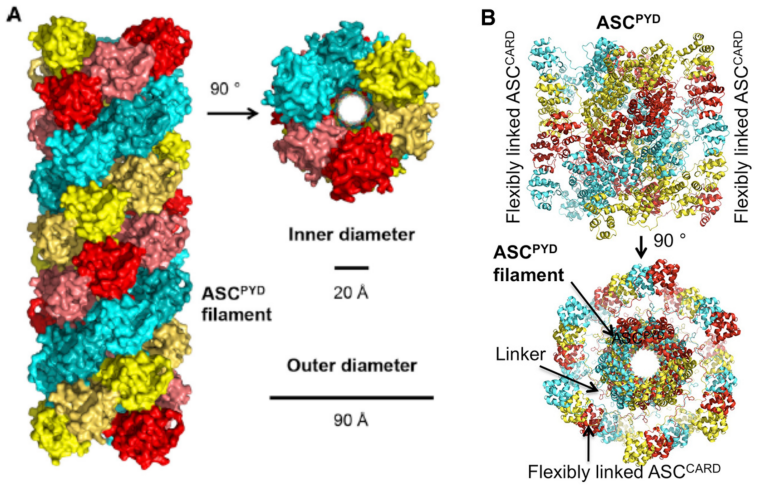

Figure 3.3: Illustration of ASC filament oligomerization as obtained by cyro-EM. (A) Helical arrangement of ASC^{PYD} filament. (B) Full-length ASC structure resolved by NMR shows the outward located CARD with flexible links to PYD core filament. Adapted from publication [77]

3.2 Superresolution of fixed ASC specks

Although a body of research results has already provided significant insight regarding to the structure of inflammasomes, it was so far revealed largely based on experiments conducted only by *in vitro* polymerization of ASC filaments or in cultured cells overexpressing single domains (either PYD or CARD) of ASC molecules. Their presence therefore requires further confirmation from real immune cells, we thus employed superresolution microscopy to study the speck structure in macrophages stably expressing ASC tagged with fluorescent proteins.

3.2.1 Cell model used for SR imaging

To determine the structure of ASC specks in living cells, mouse bone marrow-derived macrophages were transduced with full-length ASC-GFP or -tagRFP fusion proteins for the visualization of inflammsome activation by superresolution optical imaging. As shown in Figure 3.1, cells were first primed with LPS overnight, followed by the nigericin (NIG) induction on next day which causes potassium efflux and triggers the formation of ASC specks. In the typcial case of ASC-GFP cells, the first speck can be detected within 10-15 min after nigericin treatment and more specks continue appearing in the cell population (i.e. the onset of speck formation is not synchronized among cells) in the next 30 min till all specks generally complete after one hour of incubation. During this time, the plasma membrane also shows swelling and rupture which are characteristics of pyroptotic cell death (Figure 3.4).

3.2.2 3D-SIM resolved ASC specks

In this particular ASC-GFP cell line, the number, size and the morphology of specks in single cells can substantially vary from one to another, but a single speck in diameter of 1-20 μm is typically observed close to the nucleus (Figure 3.5A). To carefully examine the development of growing specks, LPS-primed and nigericin-induced specks were fixed at different time points after nigericin treatment and imaged first by wide-field fluorescence microscopy. The speck sizes were determined by measuring the largest diagonal distance across the 2D structures and the result indicates a significant increase of speck size at later fixation time points

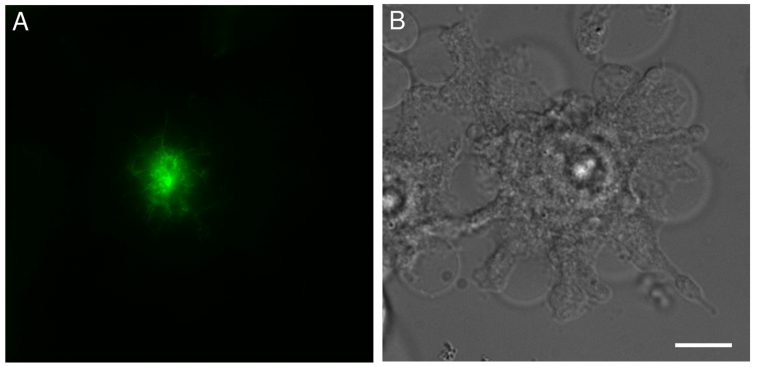

Figure 3.4: Representative images of pyroptotic cell death after LPS prime and NIG induction of inflammasome. (A) Fluorescence wide-field image of ASC-GFP assembly forming a "medusa"-like speck. (B) Same field-of-view was acquired by differential interference contrast to reveal the membrane swelling/blebbling characteristic of pyroptosis. Scale bar= 10μ m.

(Figure 3.5B). The same trend of growing specks was obtained when the z-stack of specks were imaged by 3D-SIM and processed by a semi-automated segmentation tool (ilastik)[126] to obtain the increased volume information (Figure 3.5C).

Specks of 1-2 μm in size are difficult to discern their inner structures after reconstruction of 3D-SIM, mainly because the core of specks is densely packed with ASC filaments which is in line with the previous report[121]. On the other hand, a typical topology of a gigantic speck can be well-resolved to clearly show the entanglement of filamentous structures extending from the inner core toward the periphery. Interestingly, this symmetrically spherical architecture of speck resembles the head of mythical goddess Medusa[113] (Figure 3.6). Here, the diameter of the individual filaments is limited by the lateral resolution of SIM. The full-width-half-maximum (FWHM) of single ASC filament is approximately 110 nm, as opposed to the physical size of approximately 24 nm, considering 20 nm of ASC filament plus 4 nm of GFP. Fourier ring correlation was carried out to assess the overall image resolution at 126 nm by the cut-off criterion (1/7) used frequently in localization microscopy (Figure 3.6)[10], other thresholds[91] were also applied but gave similar results (data not shown).

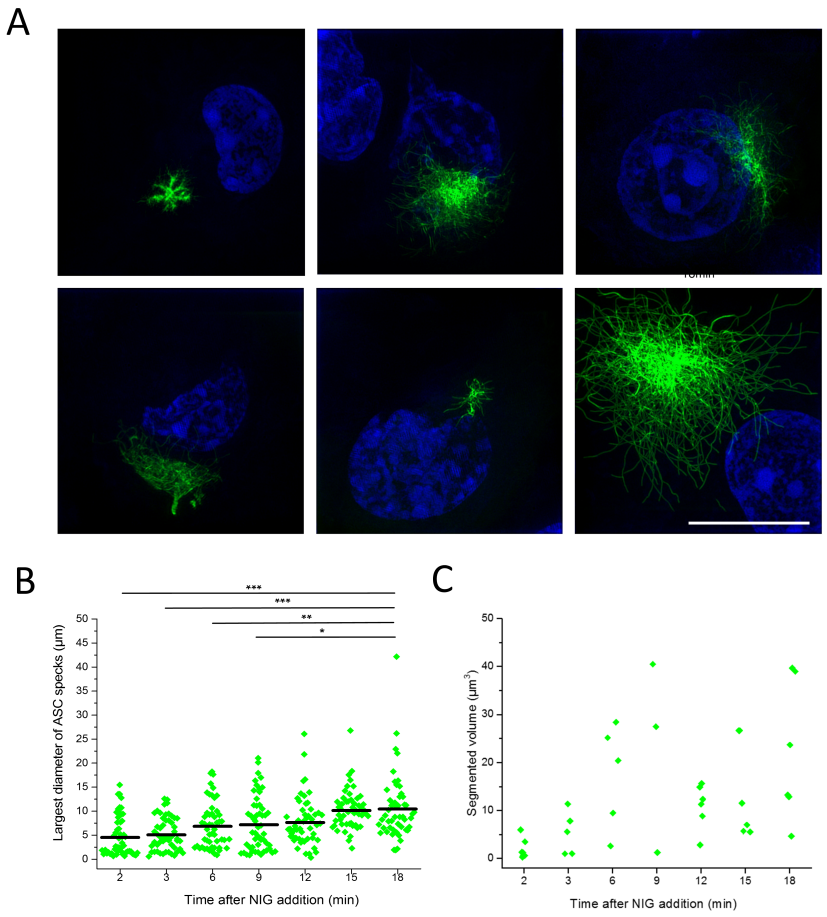

Figure 3.5: (A) Multiple phenotypes of ASC-GFP specks are imaged by 3D-SIM and shown in maximum projection. Specks are generally located nearby the cell nucleus. Scale bar= 10μ m. (B,C) Specks grow in size as the incubation prolongs. ASC-GFP cells were incubated overnight with LPS and administered with nigericin (NIG) next day for indicated time prior to PFA fixation. Specks were randomly selected under wide-field (B, n=50 per time points) or 3D-SIM imaging (C, n= 38 in total), and assessed for their size by measuring the largest diagonal distance of specks in 2D or the segmented volume in the 3D stack, respectively. Statistics were obtained by one-way ANOVA. ***p<0.001, **p<0.01, *p<0.05.

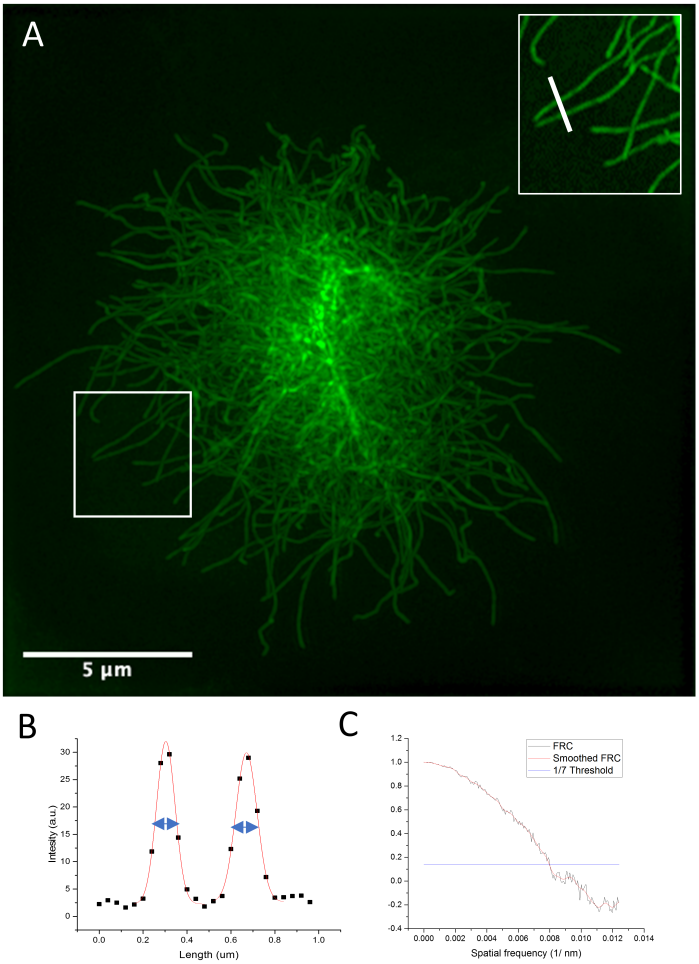

Figure 3.6: A Medua speck revealed by 3D-SIM. (A) Maximum projection view of the entire z-stack of 10 μm shows the topology of Medusa's head. Gamma function is applied to image visualization to even out the intensity variation across the speck. Inset displays a zoom-view of the boxed region. (B) Line profile of two ASC filaments from the inset in A are fitted with Gaussian and the FWHM is 99.7 and 113.7nm, respectively. (C) FRC is computed from two independent acquisitions of identical Medusa specks as shown in A, raw values are smoothed and drops down to a fixed threshold value 1/7=0.1428 as the cut-off frequency of resolution determination.

3.2.3 dSTORM imaging of ASC specks

In the previous section we have seen that the diameter of single ASC filaments is limited on the effective resolution of the 3D-SIM in terms of wavelength and numerical aperture of the objective. In a pursuit of resolving single ASC fibers in further detail, I also use localization microscopy to achieve even higher spatial resolution. To meet the criterion of on-off switching/blinking of single emitters in SMLM, ASC specks were immunolabeled with the corresponding primary antibody (Ab) and a secondary Ab conjugated with Alexa 647 which is widely used in dSTORM measurements. The fidelity of the anti-ASC antibody was first successfully verified by applying it to ASC-GFP specks which serves as the ground truth of successful immunostaining. The SIM reconstruction showed almost perfect colocalization of immunolabeled ASC with the GFP-tagged structure (Figure 3.7A). After this confirmation, the immunolabeled structure was then imaged by dSTORM (Figure 3.7B-D).The FWHM and FRC measurement of single filaments obtained from the reconstructed images is 63 and 54 nm, respectively (Figure 3.7E and F). The physical diameter is estimated at 52nm after two antibodies, adding 14nm in size per IgG, were subjected to the ASC filaments. Therefore, the use of dSTORM truly revealed the physical identity of single ASC filaments. Here we showed that superresolution microscopy is suited to address the fine architecture of ASC specks which are otherwise be resolved by the wide-field imaging.

3.3 Localization of sensor and effector in specks

One can speculate how the inflammasome is generated in the form of specks, especially what the driving force or the mechanism is to initiate the oligomerization of ASC molecules that originally scatter across the entire cell but are quickly recruited into this amazing structure within minutes after activation. In fact, our innate immune system employs a diverse set of sensors to detect the presence of infection or cell damage. Prior work has found certain sensor proteins responsible for the assembly of inflammasomes, such as the NOD-like receptor (NLR) family members (e.g. NLRP1/3, NLRC4) or AIM2 (absence in myeloma 2) in response to a variety of microbial agents[70][123]. We, therefore, are highly interested in knowing the location of the sensor (NLRP3) and effector (caspase-1) molecules relative to the ASC speck structure.

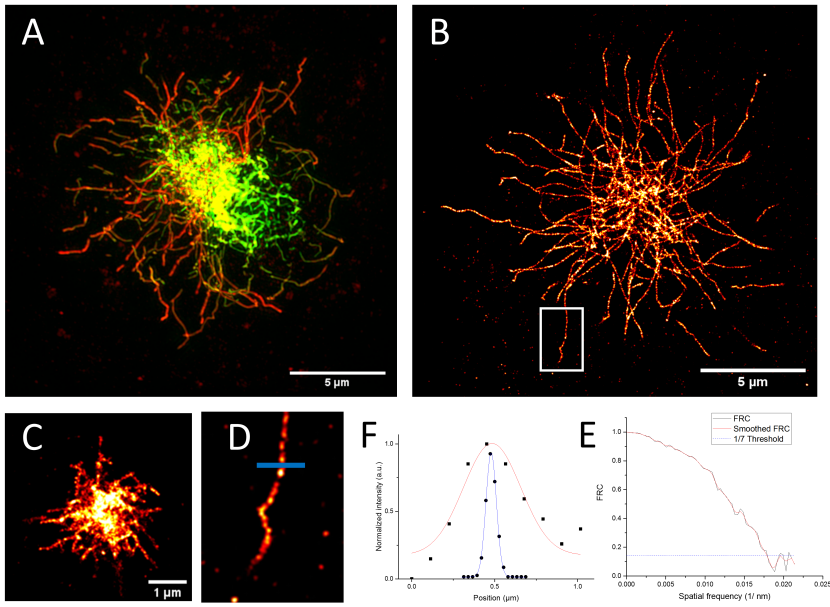

Figure 3.7: (A) Maximum projection imaging of 3D-SIM data. Antibody labeling of ASC (red) shows identical staining pattern as opposed to GFP-tagged structure (green), except limited access of the antibody to the inner core of the speck and regions close to the nuclear envelope. (B,C) Representative dSTORM images after reconstruction by thunderSTORM (courtesy of Anders Engdahl). (D) Higher magnification of box region in B which shows a single filament, of which a line measurement was Gaussian-fitted to determine the FWMH= 63 and 407 nm for dSTORM and average wide-field microscopy images, respectively (F). (E) Localization events obtained in B were split into two parts (odd and even frames) for the FRC analysis which estimates the resolution of the cropped image D at 54nm.

3.3.1 NLRP3 sensor in ASC specks

In the beginning, our collaborator constructed a mouse macrophage cell line expressing double-labeling fluorescent proteins: NLRP3 fused with SkylanS and ASC with tagRFP. In addition, to prevent the unwanted self-assembly of the specks triggered by other environmental stress stimuli, the expression of NLRP3 is engineered to be "Tet-on"[33] by the addition of doxycycline to the cell medium overnight. We aimed at resolving the structure of ASC speck with the precise location of NLRP3 sensor by 3D-SIM. However, the expression of NLRP3 is rather low and it is transgenically modified with reversibly switchable fluorescent protein, SkylanS, which switches to off-state quickly by its design[162]. Therefore high power of 405nm and

488nm excitation was applied to constantly excite and readout the SkylanS which inevitably caused the cross-talk signal from the red channel that spilled into the green spectrum. We thus obtained identical structures from both labeled molecules (data not shown). To avoid the cross-talk that leads to misinterpretation, cells expressing NLRP3-SkylanS alone were used to perform the inflammasome study in combination with anti-ASC antibody. By means of indirect labeling with secondary antibody conjugated with Alexa 633, we were free to present the ASC in a more red spectrum to tackle the cross-talk problem. Indeed the localization of ASC was faithfully reported on tiny spots close to the nuclei under the examination of deconvolution microscope (Figure 3.8). Some of these ASC specks were found colocalized with NLRP3 in higher magnification, however, the size of which were restricted in approximately 1 μm in diameter that is impossible to locate the precise position of NLRP3 relative to the whole ASC speck.

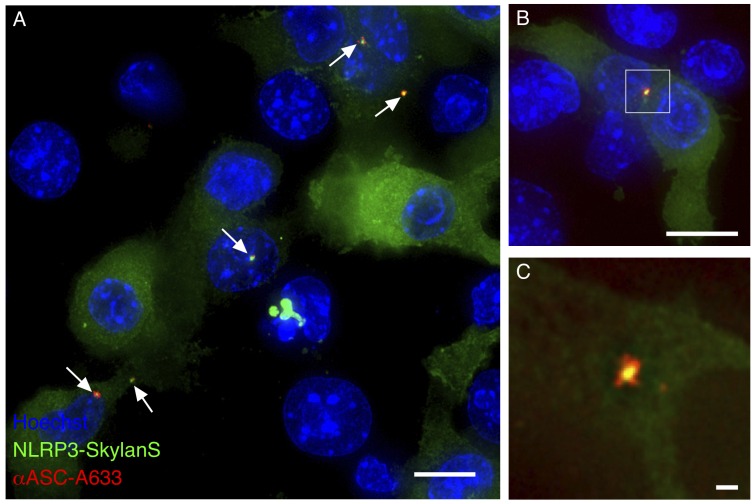

Figure 3.8: Localization of NLRP3 fluorescence proteins in ASC specks by deconvolution microscopy. Mouse macrophages expressing SkylanS-tagged NLRP3, primed by LPS overnight, induced by nigericin to form ASC specks which were immunostained with α-ASC antibody and revealed by secondary Ab conjugated with Alexa 633. Cell nuclei were counterstained with Hoechst 33342. (A) Low magnification micrograph (20x) shows many ASC specks forming in the juxtanuclear positions, where the expression of NLRLP3 were also colocalized (arrows). (B) Higher magnification of an NLRP3 inflammasome forming cell. Boxed region is further digitally zoomed and displayed in (C), but lack of resolution to see the detail of colocalized structure. Scale bar= 10μ m in A and B, 1 μm in C.

Hence, the 3D-SIM was utilized to give more insight into the structural com-

position of ASC specks (Figure 3.9). It actually showed promising resolution to unravel the central positioning of NLRP3 in the speck, indicating its nucleation ability to initiate the ASC filament formation that is in line with the current model[161][77][24]. However, we also noticed that the immunolabeling of ASC revealed a punctated structure rather than a filamentous network of speck. The bulky immunoglobulin may prevent from densely labeling of ASC filaments that results in the discontinuity of linear structures. Therefore, more efforts were put on creating cell lines expressing both NLRP3 and ASC molecules tagged with fluorescent proteins. Two macrophage cell lines were thus generated, one derives from a wide-type genetic background, the other derives from an NLRP3 knock-out cell line. Both of them have the labeling of NLRP3 with tagRFP, while ASC was labeled with GFP. The results further confirm the centroid of NLRP3 within ASC speck even though its weak intensity suffered heavily from photobleaching during the acquisition of multiple frames of phase shift, rotation and z-slices (Figure 3.10A). The general structure of NLRP3 is point-like spot but short filaments stemming out from nucleation point can be occasionally observed, which is in accordance to the findings of reconstituted NLRP3 filaments in cryo-EM[77]. In addition, the introduction of NLRP3-tagRFP seems to be a gain-of-function feature because the presence of NLRP3 was often found in the cells possessing multiple tiny specks (Figure 3.10B).

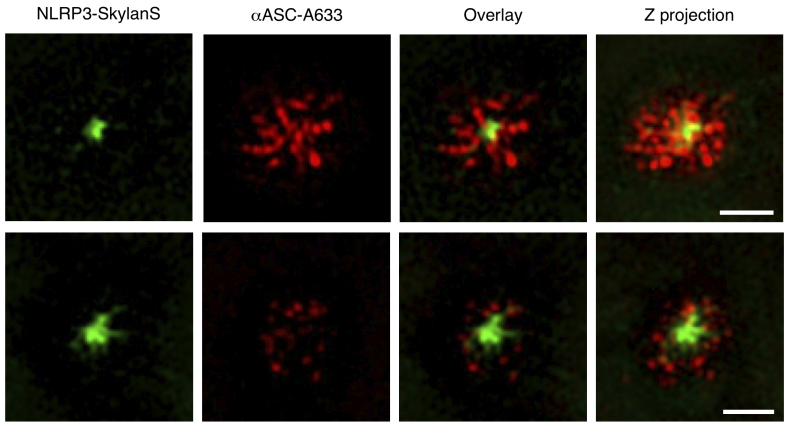

Figure 3.9: Center position of NLRP3 in super-resolved ASC speck. Cell samples were prepared as in Figure 3.8 but imaged by 3D-SIM. Here two examples are shown in single plane section as well as Z projection in the rightest column. Note that the ASC structure seems to be punctates rather than filaments. Scale bar= 1μ m.

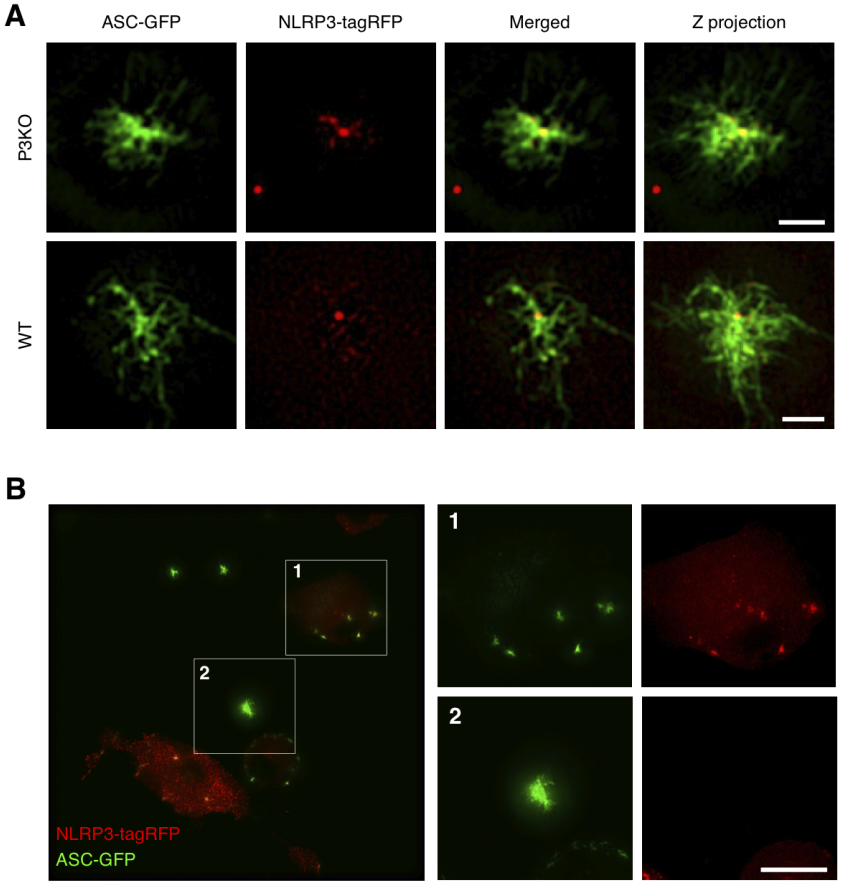

Figure 3.10: Cell lines transduced with dual fluorescence fusion proteins to reveal the location of NLRP3 within ASC specks. (A) Each of the cell lines were created with indicated fluorescence fusion proteins in either NLRP3-knock out (P3KO) or wildtype (WT) parental macrophages. (B) Deconvolution imaging of the NLRP3-KO cells expressing virus-transduced fluorescent proteins. It is quite often to find multiple tiny specks existing in NLRP3-expressing cells (cell No. 1), while single and relatively bigger speck is present in the absence of NLRP3 expression (cell No. 2). Scale bar= 1μ m in A, 10 μm in B.

3.3.2 Caspase-1 effector in ASC specks

As of the effector, the activated caspase-1 was tagged with fluorescently tagged YVAD motif that interacts with the catalytic domain of caspase-1. Therefore the labeling is specific to activated form of caspase-1 and it also allows live-cell staining. The initial step was performed on live-cell staining of caspase-1 and then the cells were fixed for immunofluorescence labeling of ASC (Figure 3.11A). The labeled structure of caspase-1 appeared to be cover over the entire speck structure which is consistent with the current concept that the caspase-1 also polymerizes around the ASC filaments via the contact of CARD domain[24][121].

However, the ASC molecules were identified as fragmented filaments extending outwards. Since we had experienced incomplete labeling by using the anti-ASC antibody, the faithful representation of speck structure was put into question. We thus turned to use the transgenic cell line once again to verify the observations from the immunolabeling of ASC assembly. The results turned out to be substantially different from the previous results. The caspase-1 share almost identical staining pattern as ASC fluorescent fusion protein, suggesting that the caspase-1 was recruited and built around the ASC filaments (Figure 3.11B). It is thus concluded that the physical hindrance of the dense speck structure does not allow the labeling in the inner core where the hidden epitopes were far from the reachable range of the antibody. Therefore, the transgenic fusion protein provides sufficient labeling density on the ASC specks for SR imaging.

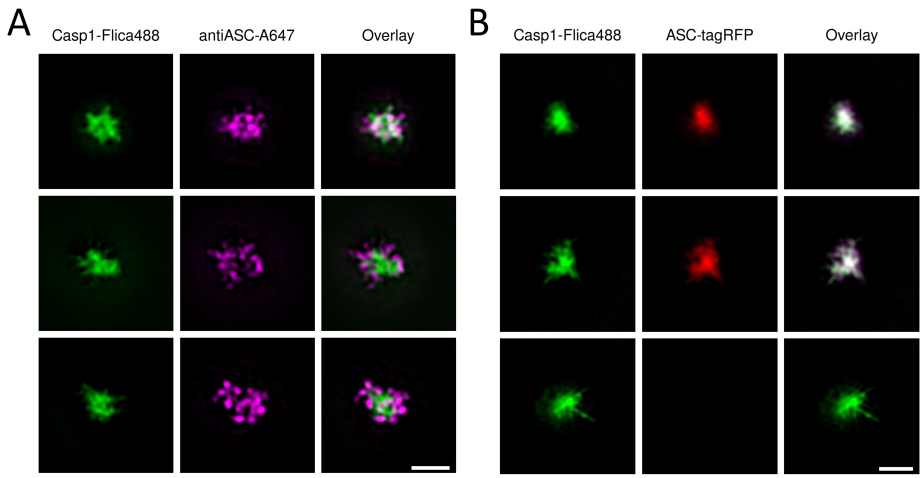

Figure 3.11: Single plane representation of reconstructed SIM images. (A) Three representatives of ASC specks were first labeled with caspase-1 by the commercial kit (FLICA488) in living cells and then fixed for immunostaining with anti-ASC antibody and the secondary Alexa 647-conjugated antibody. Scale bar= 1μm. Activated caspase-1 are visualized on ASC specks, whose central part is missing from the immunolabeling. (B) Cells transduced with RFP-tagged ASC fusion proteins were live-stained with FLICA 488 kit. Cells in the top and middle rows represent totally overlapped localization, whereas the bottom row shows the accumulation of caspase-1 in absence of ASC speck, which indicates no cross-talk contribution from FLICA 488. Scale bar= 1μ m.

3.4 Living speck imaging by 4D-SIM

One of the best-known advantages of structured illumination microscopy is the application on live-cell imaging, for it is not dependent on particular types of fluorophores which are generally needed in SMLM and STED microscopy, it is thus capable of long-term observation with much less illumination power (10-100W/cm^2)[44][119]. We, therefore, apply 3D-SIM on time-lapse recording of individual growing ASC specks in an attempt to understand the overall development of inflammasomes and the dynamic processes of ASC filament formation.

3.4.1 Time-lapse recording of growing specks

As the complete formation of inflammasomes can be finished in the range of 3-10 minutes depending on its size, it is challenging to capture the very starting point of speck formation, besides the onset time is not synchronized among the cells and the focal plane needs to quickly set with proper stack volume to cover the expansion of growing specks. However, some representative recordings of specks were obtained after tedious works and patience (Figure 3.12A). The time-dependent intensity distribution is shown in a line profile measurement, which indicates that the soluble ASC monomers were recruited rapidly in the speck core as the periphery filaments also stretch outward (Figure 3.12B). But this approach is limited in one angle, we therefore further analyzed the radial distribution (Figure 3.12C). It is calculated by first summing up the z-stack into 2D images on which numerous concentric circles, from the center to periphery, were applied to collect the mean pixel values along the perimeters and thus to gain the radial distribution of specks. Furthermore, the 3D volume of developing speck was isolated by image analysis tool (Imaris) and quantified the growing volume and the surface area of the segmented structure (Figure 3.12D). In summary, the features of the growing specks obtained from the living cells are investigated for the first time by using 4D-SIM method. The results are essentially attributed to its applicable advantages on live-cell imaging. Moreover, the two-fold resolution enhancement leads to clear images of the filamentous structure of the inflammasomes, which is otherwise a bright spot on the confocal microscope. Our 3D-SIM technique truly revealed the speck structures with single-filament resolution that enable us to extract the information of growing inflammasome and the spatial distribution of speck filaments.

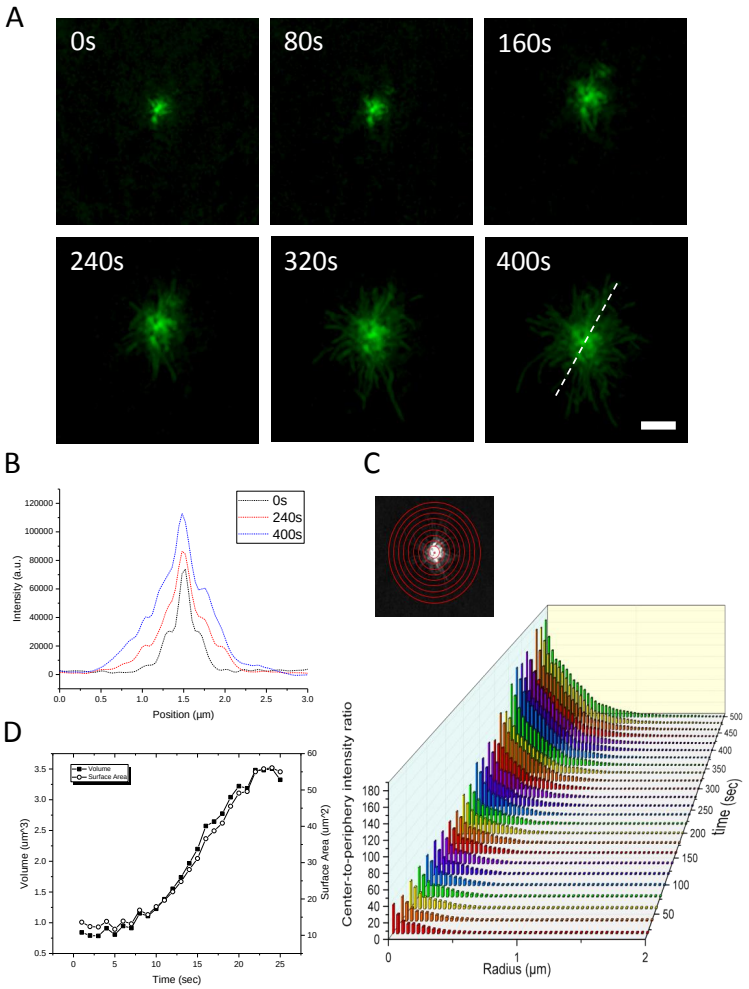

Figure 3.12: Time-lapse recording of a growing ASC speck. (A) Sum projection of the SIM reconstructed 3D-stack images from representative time frames. The acquisition interval is 20 sec in a total time of 6 minutes recording. Scale bar= 1μ m. (B) Line profiles drew diagonally across the speck of indicated time frames reveals the increasing intensity of the core and the speck expansion in space. (C) A sample picture depicts the concentric circles used to analyze the radial intensity distribution of the speck and plotted as a function of time. (D) Volumetric measurement of the speck development. ASC structure was analyzed by Surface segmentation in Imaris software, therefore the surface area of the segmented compartment is also quantified.

3.4.2 Dynamics of filament formation

Besides the general observation of the overall structure and intensity distribution, specific details on the filament formation were also available over the time period of acquisition. In the case of macrophages which were genetically modified by tagging RFP onto the N-terminus of ASC sequence, the speck formation had been visualized as the ASC molecules polymerized into filamentous structures (Figure 3.13). Some remarkable features are highlighted here: the increasing size of speck is resulted not only from the elongation of existing filaments but also the new filaments branching out from the original ones. Prior to the branching, a higher fluorescent signal was often found at the branching site where the diameter of the filaments is slightly enlarged, suggesting that ASC was first recruited locally to establish a structural foundation for branching. The increasing length and branching of filaments greatly increases the dimension of ASC specks and thus offers more contact area for interaction with the downstream effector, caspase-1, and in turn, facilitate the catalysis of more active cytokines. The same features of elongation and branching were also verified in ASC-GFP cells (Figure 3.14), along with an additional discovery, the cross-linking of filaments. With the aid of 3D visualization software, cross-linking of the filaments via direct contact is surprisingly identified, and this phenomenon is assumed to help consolidate the ASC filaments into a single speck[57]. This observation can also answer why the speck center is so compacted where numerous filaments are interconnecting and resulted in such a sophisticated structure that is hard to discern, particularly in a micron-sized speck. Nevertheless, the development of inflammasome formation was for the first time reported by live-cell imaging of 3D-SIM which shows the extension, branching and cross-linking of the filaments that have never been reported before.

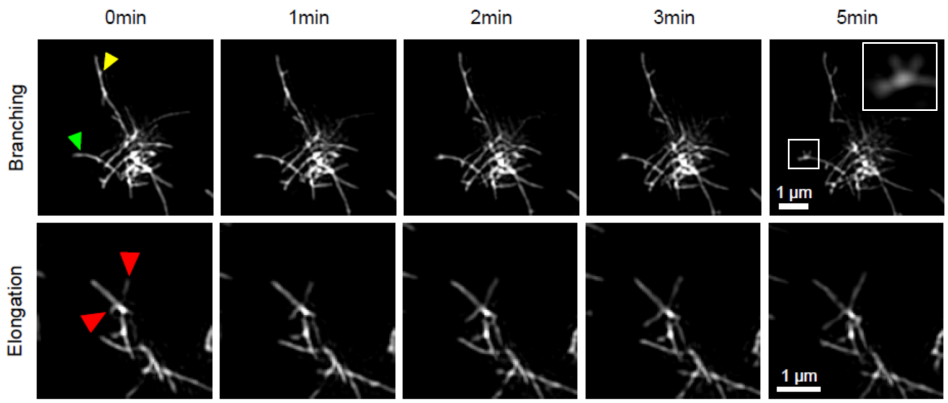

Figure 3.13: Filament branching and elongation in the development of ASC-tagRFP specks. (Upper row) Yellow and green arrowheads depict the budding of newly growing filaments. Before a new filament branches out from the existing one, the enlargement at the branch points was frequently visualized, suggesting that local recruitment of ASC was first established before the new filaments appeared. Normally one side branch grows out from original filament (yellow arrowhead) but two may occur in rare cases (green arrowhead and inset). (Lower row) The length of two side branches (red arrowheads) were extended as ASC molecules polymerized at the tips of filaments.

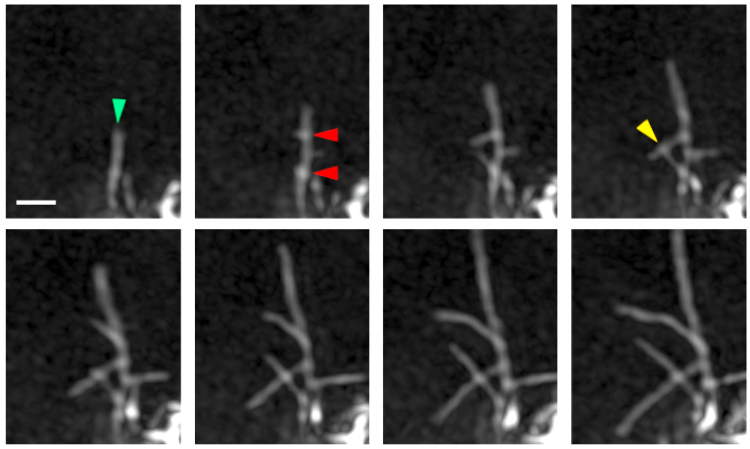

Figure 3.14: Extension, branching and crossing events in the development of ASC-GFP speck. While single filament (green arrowhead) grows upward with increasing length, two branches (red arrowheads) appeared simultaneously and extended till they physically in close contact (orange arrowhead) and kept growing in same directions, thus forming a cross. The cross-linking point was confirmed in 3D view. The time interval between each frame is 20 sec. Scale bar= 0.5μ m.

3.5 Structural analysis of the ASC specks

Based on the observation that growing filaments tend to connect with each other, we wonder what the underlying mechanism is responsible for cross-linking. Schmidt *et al.* have proposed that the filament cross-linking is mediated by the interaction of CARD-CARD between adjacent filaments which can be blocked by the nanobody that chelates the interface between CARDs[120]. To confirm this hypothesis, another cell line expressing the truncated form of ASC molecules was used for the structural study. In this cell line, ASC molecules are lack of CARD at the periphery of ASC filaments which is built solely by polymerization of PYDs. To quantify the structural difference between full-length (ASC^{FL}) and truncated form (ASC^{PYD}) of GFP-tagged specks, imaging analysis tools were used and described as follows (Figure 3.15).

3.5.1 Analysis tools and methods

To analyze such molecular complex, the filamentous structures were first isolated from the reconstructed stack images of 3D-SIM. The segmentation step was done by either applying a proper intensity threshold or by using a trainable multiple algorithms-assisted network to help identify the filamentous 3D structures (ilastik). The binary images were then sent into the trimming process that transforms the 3D structures into pixel-wise skeletons (Skeletonize, Fiji plugin). The last step is to identify the position of every single pixels relative to the others and classify them as either endpoint, filament branch or junction (Analyze Skeleton, Fiji plugin)[7]. This identification is done by knowing how many neighbors one voxel has in its 26 surrounding voxels. If there's no neighbors but a single voxel, then it is considered to be just noise and filtered out in post-processing. With only one neighbor, it is considered as the filament end. Exactly 2 neighbors would be considered as part of filament branches, whereas more than 2 neighbors would be defined as the junction point, respectively. Lastly, the final classification of each pixel are color-coded and the structurally analyzed specks can be presented again in three dimensions. When applied this analysis, the topology of individual specks can be better understood, particularly the networks of ASC filaments resulted from cross-linking. It should be noted that the accuracy of skeleton analysis is highly dependent on the image quality. Optimized imaging conditions (e.g. immersion index of oil) should be met to reduce the artifacts such as ghosting or hatching that could be potentially

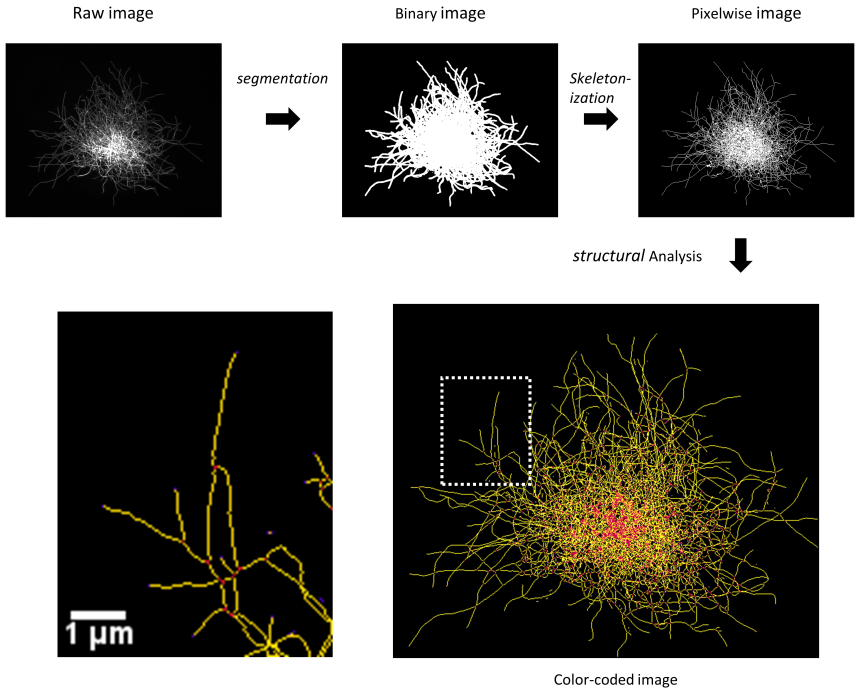

Figure 3.15: Schematic workflow of image analysis of the inflammasomes. Reconstructed 3D-SIM stacks were used as input data as shown in representative pictures. The entire processes were performed on individual z slices but they are here presented as maximum projection for better visualization. The end product after the skeleton analysis can be interpreted as free-end (purple), junction (red) or filament branches (gold) pixels of the speck structure.

misinterpreted as real structures.

In the next step, the 4D image sequence shown in the figure 3.14 was put into the workflow of structural analysis in order to get the structure information from the growing speck (Figure 3.16A). The structural analysis of the time-lapse recording also helps easier to trace the filament growth and to visualize the branching or cross-linking events. Quantitative analysis shows that while the speck expanded the territory by extending and branching the filaments, the number of junctions was increased accordingly, whereas the number of free-ends was not substantially increased. It is suggested that the majority of the newly formed filaments were cross-linked to form the junctions, especially in the inner core of the speck (Figure 3.16B). To further analyze the junction sites, one can visualize the number of

branches extending from a single junction (Figure 3.16C). A triple junction linking to three branches can be the result of the bifurcation of new filament (Figure 3.13) while those that have four interlinking branches could be formed by cross-linking of two filaments as we have seen in figure 3.14. This is the first time that the sophisticated structure of ASC speck is revealed by a structural analysis on the 4D-SIM recorded inflammasome formation.

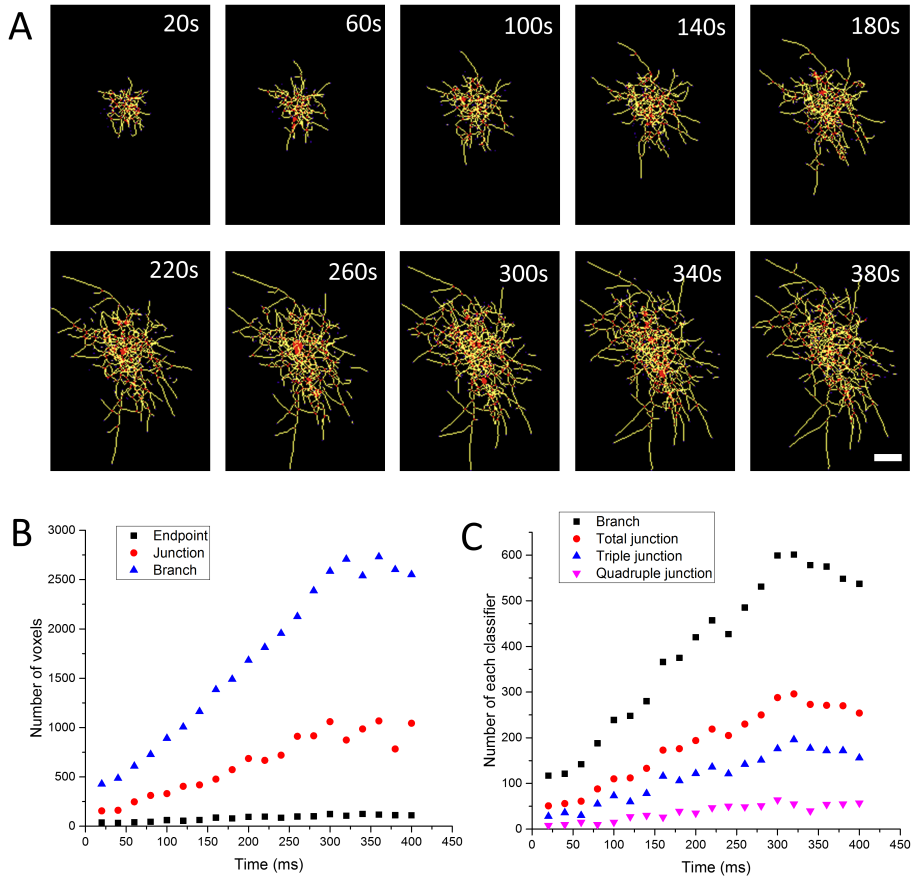

Figure 3.16: Skeleton analysis shows the structural compositions of a growing speck. The images are superimposed from 3D-stack. (A) Representative frames of the skeletonized speck after structural analysis. Scale bar= 1μ m. (B) A plot of voxels of the individual classifiers. (C) The result of another analyzed example is displayed as the number of total branches and junctions, as well as the junctions which connect to three (triple points), or four (quadruple points) branches.

3.5.2 Structure of ASC^{PYD} specks

Previous in vitro studies reported that full-length ASC assembles into highly cross-linked filaments, while PYD-containing only molecules assembled into long, linear fibrils[24][77]. Indeed, we observed the cells expressing ASC^{PYD}-GFP formed long, unbranched filaments (Figure 3.17A), as opposed to densely packed full-length ASC specks that are mainly comprised of short branches because of cross-linking and branching (Figure 3.17B). Some of the ASC^{PYD} filaments are rather thick with brighter signal, suggesting more than one filaments may likely to align parallel to form fibrils, albeit they cannot join through CARD-CARD interaction. Although the ASC^{PYD} inflammasome consists of long filaments without obvious branching, most of them are found broken into shorter fragments (Figure 3.17C). Assuming this is not a fixation artifact, the breakage of filaments may reflect the fragile structure due to lack of CARD domain to cross-link the filaments and to stabilize the inflammasomes. This is also supported by the key feature that the widely scattered structure contains fewer junctions compared to ASC^{FL} specks (Figure 3.17D). To summarize, we have visualized the integrity of ASC^{PYD} inflammasome is compromised without the presence of CARD subunits to cross-link the filaments. It has thus resulted in the distribution of widely scattered filaments without interconnections and the break down of filaments is also revealed by the SIM technique.

3.6 Discussion and outlook

Microbes or danger signals trigger inflammasome sensors, which induce the polymerization of the adaptor ASC and assembly of a perinuclear ASC speck. ASC specks recruit and activate caspase-1, which promotes IL-1β cytokine maturation and pyroptotic cell death[123][70]. The first discovery of the geometry of sensors involved in the inflammasome structure was one of the NLR family member, NLRC4[161]. The subnanometer resolution of cryo-EM experiments showed that 9-11 monomers of NLRC4 can self-propagated into a wheel-like structure, on which the ASC dimers starts to assemble into one inflammasome. Similar structure of NLRP3 inflammasome was later revealed, but prior to the formation of a disk-like structure, another key factor NEK7 must first binds to earring-shape NLRP3 monomer, induce the conformational change which allows the oligomerization with

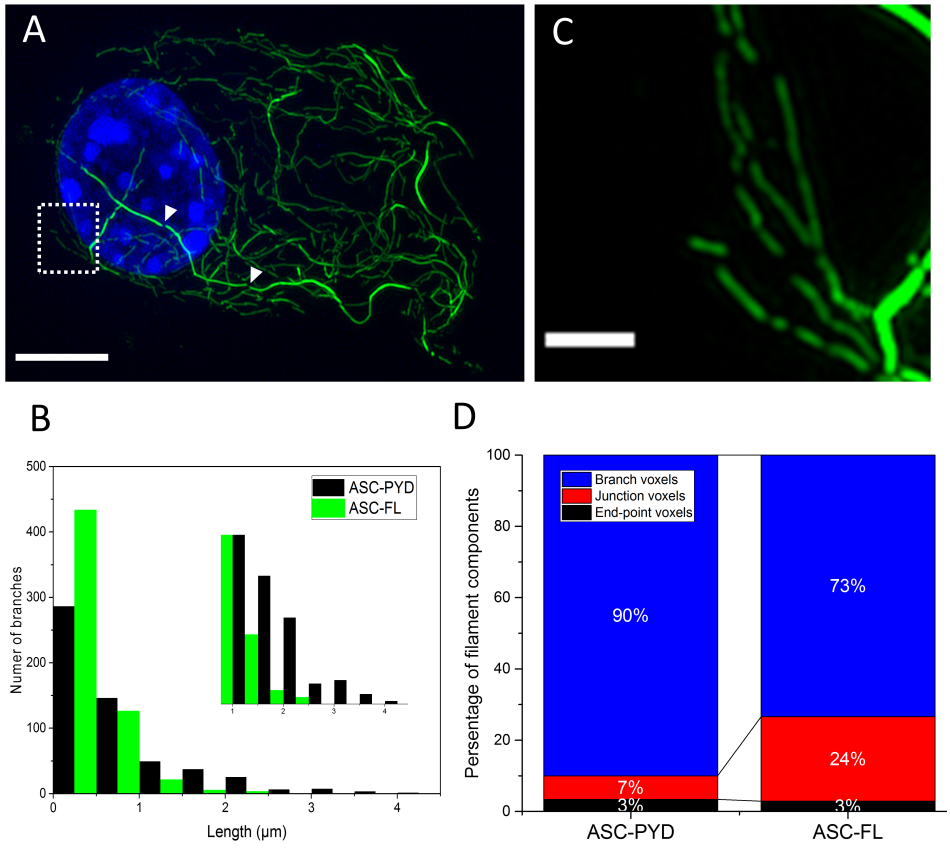

Figure 3.17: Aberrant structure of inflammasome composed of ASC^{PYD} filaments. (A) Maximum projection of 3D-SIM reconstructed image. The ASC filaments were distributed across the cytoplasm rather than assembled in a perinuclear speck. Thick fibers extend in long-distance but were broken into fragments as depicted by arrowheads. Scale bar= 5μ m. (B) Inflammasome structures of single ASC^{FL} or ASC^{PYD} cells were analyzed and filament length of each cell type is plotted in the histogram. Inset is the highlight of the longest filaments from both cell types. (C) is the dotted box in A to show the short fractions of broken filaments. Scale bar= 1μ m. (D) Structural analysis of single ASC^{FL} or ASC^{PYD} cells reveals the voxel numbers of filament branches, junctions and free-ends plotted in percentage. Cells of each type have an equivalent amount of total skeleton voxels but the percentage of junctions is much less in ASC^{PYD} which corresponds to more longer filaments.

adjacent NLRP3 proteins to complete the nucleation of inflammasomes and initiate the ASC filament formation[122]. Our colocalization study generally supports this notion as we have seen the NLRP3 locates right in the core of specks, whereas

caspase-1 is distributed around the ASC filaments and appears to be filamentous. However, this is different from the *in vitro* EM study that the caspase-1 organized on its own filaments and arranged in the star-like structure of the AIM2 inflammasomes[77]. Interestingly, ASC molecules normally assembles into one discrete speck per cell. But the transduction of NLRP3-tagRFP into the immortalized macrophage lines led to multiple specks formation. This could be interpreted as the elevated expression level of NLRP3 induces the speck formation at multiple sites simultaneously. These specks are typically smaller than one micron as one can expect that the total amount of ASC is distributed into several specks. This gain-of-function result, together with the center positioning of NLRP3 in the specks, indicates the sensoring and nucleation function of NLRP3 at the onset of speck formation[70][123].

ASC filament branching and cross-linking are first identified by SR-SIM in living cells expressing full-length ASC adaptors. Branching can rapidly increase the contact area for caspase recruitment and in turn amplify the inflammation signaling through the production of mature cytokines. Local recruitment of ASC molecules on the branching sites are repeatedly observed in the initial phase. The formation of branches can be built solely by the recombination of the bipartite characteristics of ASC adaptors or other accessory molecules may be involved. Branching of the filaments in close vicinity also creates cross-linking among the growing filaments and thus forms the junctions of filament network that helps condense the inflammasome into the speck. CARD domain of ASC was suggested to play an important role in the formation of a dense speck core via CARD-CARD interaction of adjacent filaments. In agreement with other reports[24][77], ASC^{PYD} loses the ability to form such structure, its filaments instead had relatively longer length running throughout the cytosol, although parts of them are broken into fragments that are visible by SIM. In addition to structural difference of inflammasomes, ASC^{PYD}cells are free from pyroptosis and unable to generate or IL-1β/-18 in response to AIM or NLRP3 activators[24]. The authors further showed that point mutations on the surface residuals of CARD also disrupt the speck formation with the appearance of long filaments and inflammasomal signaling is impaired. Taken together, our microscopy analysis supports the model in which the CARD domain is crucial for the filament crosslinks and to construct a functional ASC inflammasome.

In our volumetric analysis of single growing speck, the growing curve appears to be a sinusoidal shape, which differs a lot from the *in vitro* polymerization results using various stoichiometry combinations between AIM2/NLPR3 and ASC^{PYD}[77].

We believe that our super-resolved images provided the direct evidence of bona fide inflammasome formation that can not be achieved by using reconstituted proteins. Another kinetics study of ASC assembly has proposed a simple diffusion manner [15]. However, the result is based on the time-lapse confocal microscopic recording, which has drawbacks of less sensitivity and the dynamic range of PMT detectors. On the other hand, fluorescence correlation spectroscopy (FCS)[102] might be a better method to determine the local concentration of ASC reduction in the cytoplasm and to infer how they integrate individually into existing speck surface. Other mechanisms such as active transportation of ASC dimers could be considered and therefore the kinetic process of ASC assembly would be an interesting study to follow.

Chapter 4

Other SR-SIM projects

4.1 Optical clearing for tissue sections

Imaging in thick tissues is always challenging in microscopy mainly due to the issues of the light scattering, optical aberrations, absorption, and autofluorescence of the tissue itself[108]. The first obstacle is light scattering. This phenomenon gives the tissues milky appearance because the light is largely scattered. This argument stays true for microscopy as the labeled molecules are not efficiently excited by the focus of the light, and the emitted light is scattered again and does not form a sharp image on the detector. This is also the reason that the biologists use often the thin tissue sections rather than the whole mount of the intact organs to avoid the scattering effects on the microscopic images. The fundamental principle of scattering is the absorption of the photon by the electrons of the interacting matters, which gains the energy but not high enough to lift the molecules to the excitation states. Thus, the absorbed energy is re-emitted as light again with the identical wavelength (and frequency). This is called Rayleigh scattering and it has the emitting intensity inversely proportional to the fourth power of the wavelength of the incident photon, which means the blue light is much prone to be scattered than the red light. Therefore, the infrared is preferentially used in the two-photon excitation microscopy for deep tissue imaging. This problem gets even worse in the biological samples that contain the inhomogeneous distribution of scatterers (i.e.

proteins, lipids, carbohydrates and of course water) that have different refraction indices. The overall outcome is the higher orders of scattering which causes the light to and from the fluorescent labels bent and deteriorates the images.

The second problem is the spherical aberration that originates from the lens manufacturing. When the surface curvature of a lens is produced in spherical instead of parabolic shape, the light rays that pass through the edge of the lens do not converge with rays passing through the center of the lens. This leads to a spread of focus spot not restricting to a single plane. To date, all the high-end objectives (or in conjunction with the tube lens) are corrected for spherical aberration, and an axial PSF should have a symmetrical hourglass appearance. But the spherical aberration appears and the shape of PSF is distorted in an inhomogeneous samples that have refraction index (RI) (RI=$\sim$1.45) different from that of the immersion media (e.g. RI of oil=1.515). Since the reconstruction of SR-SIM requires the default OTF which is derived from the PSF recorded directly from the system with matching refraction index, any imperfections of the PSF resulting from the wavefront distortion in the sample would cause the reconstruction artifacts[20]. Here I demonstrate that the altered PSF can be easily reproduced by imaging a 100 nm Tetraspeck bead embedded in agarose gel with an oil objective (Figure 4.1A). The RI mismatch between the bead and oil reshapes the axial PSF into an extended lobe with the side-lobes facing to or away from the glass. The alteration of the PSFs is further deepened on the beads away from the coverslip (Figure 4.1B). To deal with the adverse effect induced by RI mismatch, several approaches can be applied. First, use the immersion medium that has the RI close to that of the sample medium (Figure 4.1C). In the case of the embedded beads, the water objective would be the best choice whereas other objectives tend to introduce various degrees of spherical aberrations. As for the fixed sample of cells or tissues embedded with the mounting medium such as Vectashield (RI= 1.45), the objectives using glycerol or silicon oil as immersion media would be on the top of selections. Second, one can also use the correction collar built on the objectives to compensate the RI mismatch (Figure 4.1D), although its design is meant for the compensation to the coverslip thickness not equal to 170 μm. Last but mostly used, the RI of the used oil need to be optimized for specific specimens and even for a limited range of axial depths and emission wavelengths if the RI mismatch is inevitable for specific applications[9]. For example, the higher NA of an oil-immersion objective is always preferred for superresolution imaging on the living cells where they are kept in the medium which has the RI close to water.

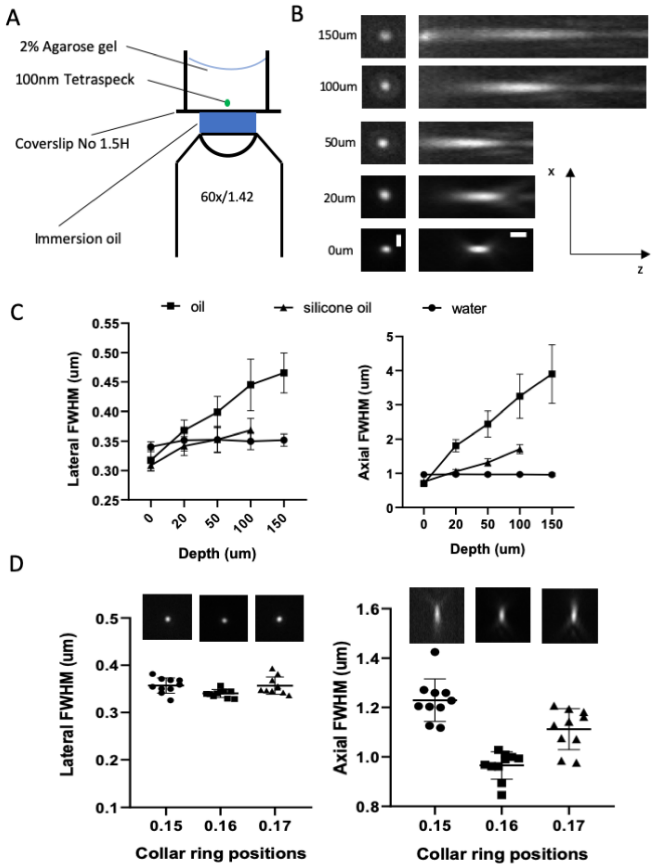

Figure 4.1: (A) Schematic illustration of the sample preparation and the imaging condition. Tetraspeck beads are embedded in the agarose gel which has RI close to water (i.e. 1.33) and excited by 642nm laser to record in z volume under wide-field illumination with the oil objective. (B) Lateral and axial PSFs of the beads from different z positions are indicated by the distances away from the bottom glass and the representative micrographs are shown in the corresponding focal depths. Note that the PSF which locates at the glass surface (0μm) has the sharpest contrast and symmetric profile, whereas those locating deeper in the gel are heavily distorted into a long shape and the contrast of which are also degraded. Scale bar= 1μm. (C) PSFs are recorded in the same illumination scheme as in A but recorded with different types of immersion objectives. The measured PSFs in various depths are shown in FWHM. The use of water objective gives consistent PSFs over the entire depths. (D) The optimization of the correction collar on a water objective compensates the variation of the glass thickness.

The adaptation of immersion oil to the samples has its limitation on the trade-offs between focal depth and color labels, and matching the RI to individual specimens requires the experience and tedious works of trial-and-error[20]. Another methodology which replaces the sample substances with RI matching material is called optical clearing[108][125]. Here I chose SeeDB2S as the clearing reagent which has the excellent translucent capability for superresolution imaging in brain tissues[61]. It also has the RI of 1.518 that matches the RI of the immersion oil and the borosilicate glass (BK7, $\sim$1.52), and thus it reduces the scattering and spherical aberration and keeps the fluorescent labels intact during the substitution process. First, I applied the SeeDB2S reagent (70.4 %of iohexol) onto the agarose gel overnight in order to let the reagents infiltrate into the gels. Subsequently, the PSF of the beads was assessed in different focal depths in comparison with those in native gel that did not have the clearing step. The results showed that the beads embedded in the SeeDB2S-cleared gel have the PSFs that are substantially restored from the spherical aberration (Figure 4.2A and B), which can be also translated into a better modulation contrast of the SIM pattern forming inside the cleared gel (Figure 4.2C).

After the successful application of the clearing reagent on the artificial samples, I turned to use the mouse brain as the next clearing targets, because we and our collaborators would like to use the SR-SIM to uncover the intricate neural networking of the hippocampus which is crucial for memory formation[103]. The procedures of the published protocol was thus conducted on one half of the dissected mouse brain while the other half was kept intact. The results clearly showed that the entire olfactory bulbs and the cranial part of the brain up to 2 mm from the surface were turned transparent compared to the uncleared counterpart in two days of preparation (Figure 4.3, upper panel)[61].

We aimed to use the clearing technique to image the hippocampus which is deeply embedded inside the brain (Figure 4.3, middle panel). However, the antibody labeling has to be applied before clearing with SeeDB2, but unfortunately that an antibody can only penetrate the tissue in 300-400 μm[125], therefore the hippocampus is not reachable. Due to this reason, the hippocampus tissues were first obtained from cryosectioning. The whole slide of mouse brain was horizontally sectioned on a cryostat in 20um thick, post-fixed with 4 %PFA. It was then immunostained with anti-neurofilament M, a neuronal marker, and the secondary Ab conjugated with Alexa647, and the nuclei were counterstained with Hoechst33342. The image was stitched from more than 200 subimages captured by a 10x objec-

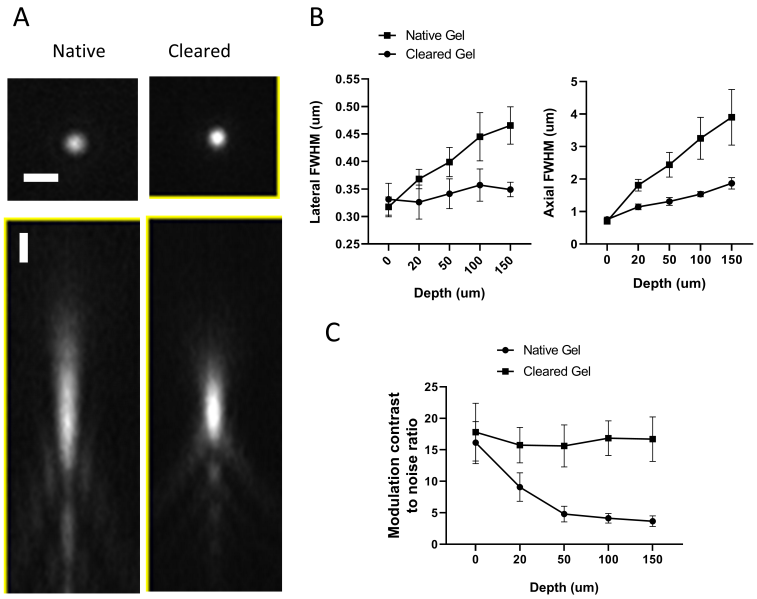

Figure 4.2: Restoration of PSF shapes after the gel infiltration by SeeDBS2 clearing reagent. (A) Representative images of the beads at 50μm away from the glass. (B) PSFs obtained from different focal positions in the cleared gel are quantified to show that the RI mismatch-induced shape alteration is partially recovered (n=5 for each position). (C) The SIM pattern has a better modulation contrast in the cleared gel. SIMcheck is used for the quantitative analysis[9].

tive on the wide-field microscope (Figure 4.3, middle panel). The tissue sectioning was carefully performed to locate a specific group of neurons from dentate gyrus (DG) which project their neuron axons (Mossy fiber) in contact with the pyramidal cells in CA3 of the hippocampus (Figure 4.3, lower panel). This structural arrangement of the neuronal connections is known as an important circuitry for the spatial pattern separation. It is known that the ablation of the expression of NF-κB disrupts the structure and impairs the mouse behavior, suggesting that the NF-κB is involved in the neurogenesis and tissue homeostasis[53].

The future work on this project could be the combination of the optical clearing, immunolabeling and SR-SIM in order to visualize the neuron synapses between the Mossy fiber and the pyramidal neurons. A preliminary study using 3D-SIM has been performed and showed a better signal-to-noise contrast on the thin brain sections, but the fine structures of the neuronal axons were not well preserved in the quick freezing step of sample preparation (data not shown). The fixative perfu-

sion would be a better method to preserve such structures for the superresolution imaging which has been shown to reveal the morphological changes of drug-induced effects on the dendrite plasticity[116].

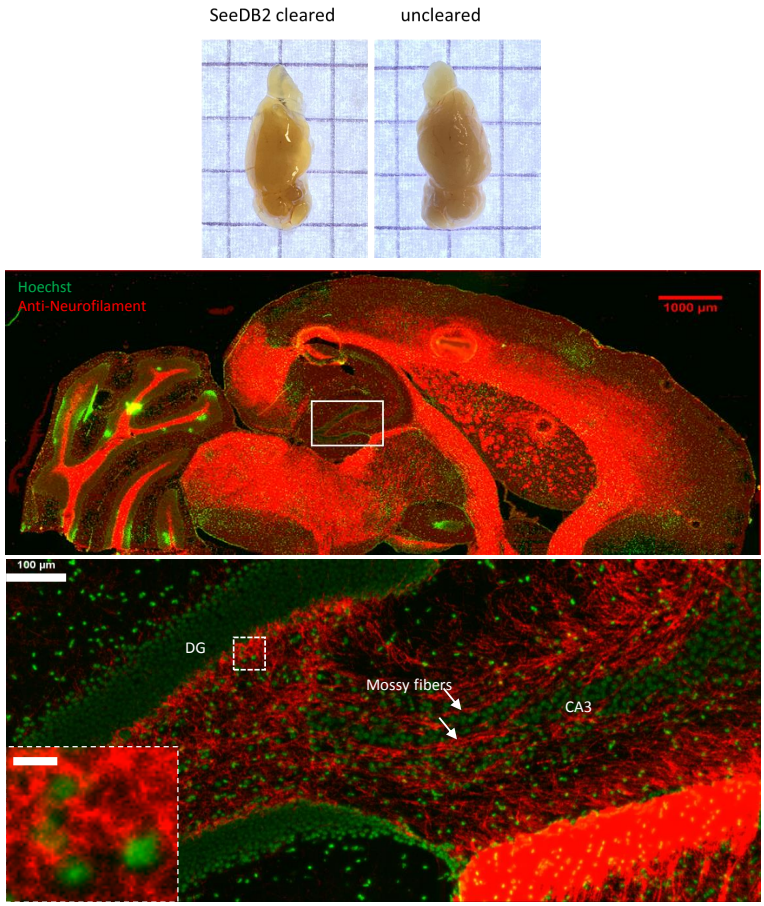

Figure 4.3: (Upper panel) The mouse brain was dissected out and one half was optically cleared, whereas the other half is kept in PBS. The image was taken with the back-illumination through a 5 mm-grid paper. (Middle panel) The stitched image acquired on the wide-field microscope with a 10x objective after immunostaining with anti-neurofilament M and nucleus-stained with Hoechst33342. The region of interest is magnified in the lower panel, where the neurofilament labeling shows the location of the granule cell bodies (inset, scale bar= 10μm) in DG and their axons (Mossy fibers) projection toward the pyramidal cells in CA3 region of hippocampus. DG: dentate gyrus, CA3: Cornu Ammonis 3.

4.2 Actomyosin network in coordinated cell movement

Our skin is the first-level defense because it provides isolation from the outer world of microbes and pathogens. Once the wall of defense is breached, it needs to be repaired by filling up the breakage with the surrounding epithelial cells that move collectively toward the wound. The driving force of this wound healing process is thus of great interest. Since the breakdown of the skin accompanies the out-spilled blood serum, the growth factors, cytokines and coagulant inducers (e.g. thrombin) are postulated as the healing factors. To recapitulate this injury process, the HaCaT keratinocytes are cultivated and allowed to grow into a single layer of cell sheet in analogy to skin formation. The cells then turn into quiescent state under serum deprivation. In this state, the cells have less higher-order structures of the actin filaments (data not shown). However, the cells are reactive again in the coordinated movement[68] and the supracellular actin network is observed when the serum or epithelial growth factors (EGF) is re-supplemented (Figure 4.4). In addition, the adherens junction are also visible as two lines of junction structure which are separated with an intercellular gap of submicron distance. The reorganization of the cytoskeleton and cell junctions are in accordance with the mechanistic prerequisites for the collective migration in the range of millimeter.

The contractile force needed for the cell movement is presumably derived from the myosin-induced filament sliding.[146]. We, therefore, stained the cells with the antibody which is specific for phosphorylated light chain residues on the myosin head (pMyosin). The localization of pMyosin was found on the actin bundles running in the apical part of the cells (Figure 4.5). The contact of myosin head with actin provides the pulling force for the cell movement and via the connection with cadherin junctions the force can be coordinated with the neighboring cells as illustrated in Figure 4.5E. The pre-treatment of EGF receptor inhibitor, Gefitinib, did not block the formation of actomyosin (data not shown) and thus suggests the involvement of EGF in cell proliferation but not in the cytoskeleton reorganization.

In summary, a serum-induced supra-cellular actinomyosin network at the apical side of the cells is highly correlated to the global coordination of epithelial movement. The images reveal a large-scale reorganization of the actomyosin networks which can facilitate the static-to-motile transition of epithelia upon the contact with blood stimuli. The future goal is to understand the spatial organization of

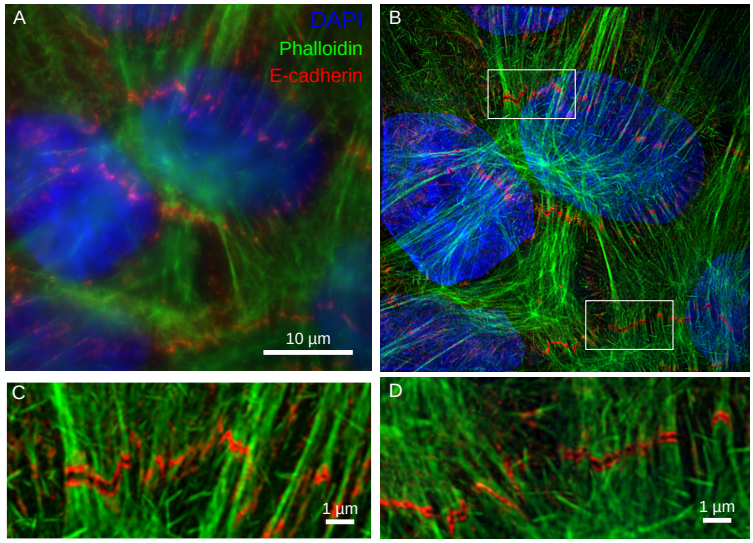

Figure 4.4: The supracellular actin filament network in the HaCaT keratinocytes cultivated in the presence of fetal bovine serum (FBS). Cells were fixed after 8 hs of FBS supplement, immunostained with anti-E-cadherin, Alexa-647 conjugated secondary Ab, then proceeded the labelings of the phalloidin-Alexa488 and DAPI. (A) Wide-field and (B) 3D-SIM images (maximum projection) of the apical part of the cells are compared side-by-side to reveal the resolved structures in the latter image. (C, D) Two boxed area in B are highlighted respectively to show the lining of cell junctions (E-cadherin) between the neighboring cells and the connecting actin bundles on each side of junctions.

the actomyosin network in order to create a model of large-scale cell migration (Figure 4.6). The SR-SIM recording of collective movement in living cells is most preferred.

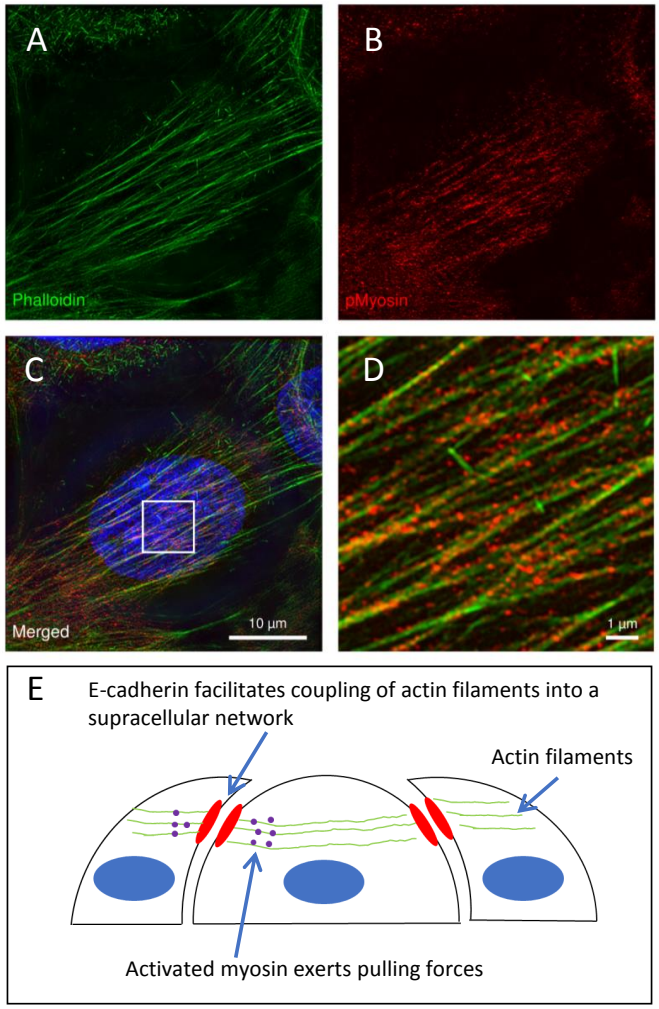

Figure 4.5: Mechanistic force that is formed via actin-myosin interaction exerts coordinated cell movement. (A-C) 3D-SIM reconstructed and z-projected images. Cells were treated as previously described, labeled with phalloidin, phosphorylated myosin (pMyosin) and DAPI. Here it shows that the actin filaments are reorganized into the parallel fibers alongside the pMyosin on the apical side of the nucleus. (D) The cluster of pMyosin is observed to anchor on the actin filaments. (E) A schematic drawing illustrates that that pMyosin exerts contractive forces on the actin filaments, which in turn mediate coordination between the cells through the junctions.

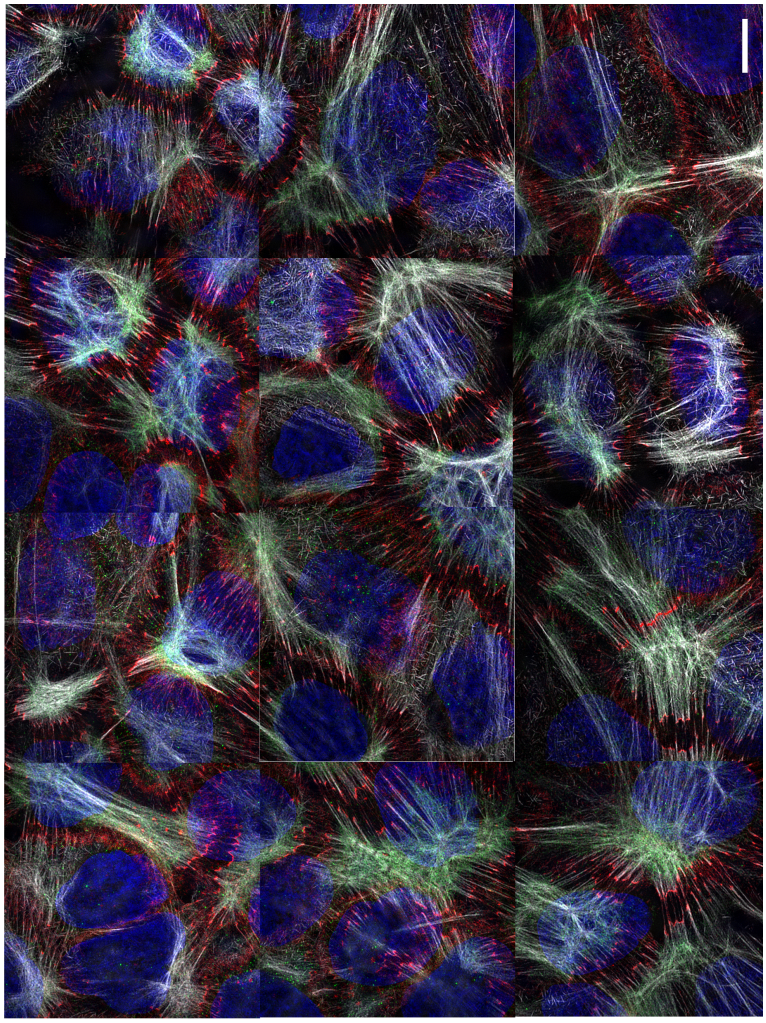

Figure 4.6: Maximum projection of a 3D-SIM stack image of the keratinocyte cell sheet labeled with DAPI (blue), pMyosin (green), E-cadherin (red) and actin filaments (white). Scale bar= 10μm.

Chapter 5

Conclusion

This work demonstrates the use of a combination of different microscopy techniques to study the cell immunity induced by microbial endotoxins. From the visualization of membrane-bound LPS by TIRF, the internalization and the vesicle transportation of LPS/LOS endosomes by deconvolution/confocal microscopy, as well as the inflammasome formation by 3/4D-SIM. Since the announcement of superresolution microscopy in the Nobel Prize of Chemistry in 2014[94][89], optical nanoscopy has been widely applied to biomedical studies[44][114]. To date, the STED and SMLM are well-established, whereas the innovation of SIM method is still thriving and the combination with other optical techniques, such as TIRF, light-sheet microscopy, adaptive optics, two-photon excitation, confocal scanning, etc., further extends its applications to a wider range of biological specimens [153]. For example, non-linear SIM[71][162] can further extend the lateral resolution down to ∼50nm which may allow us to visualize the clustering of TLR4 and its ligands. The use of transgenic fusion protein, SkylanS, may fit for the requirement of additional harmonic responses of the excited photoactivatable proteins. SkylanS[162] can otherwise be used for the fluctuation microscopy (e.g. SOFI), which has advantages of better temporal resolution and quantitative measurement surpassing other SR techniques[22].

The superresolution of a single ASC filament was achieved by SMLM down to its physical size. However, the intricate structure of speck core is still too dense to discern. This can be further resolved by electron microscopy and the use of which

in combination with fluorescence nanoscopy is a perfect tool for studying the inflammasome complexity in 3D. Therefore, more studies on inflammasome structure are expected to come up in the field of correlative microscopy[76]. The visualization of inflammasomes in tissues is also desirable as the ASC specks formed in the keratinocytes of zebrafish have been recently reported[65]. However, zebrafish is an optically accessible organism. To image the mammalian tissues, the optical clearing method can be a critical step for a successful SR-SIM imaging of ASC inflammasomes in non-transparent tissues where light scattering degrades the illumination pattern and increase the background haze. The implementation of two-photon excitation for patterned illumination can also help increase penetration depth and obtain the inherent optical sectioning which reduces the blurred light and the potential artifacts[152]. The use of adaptive optics can be expected to correct the optical aberrations of the fluorescent signals emitted from thick tissues and alleviate the issues[140].

Here I also that the ASC specks could be nice targets for the development of three-dimensional superresolution microscopy in future studies. Nowadays, the cytoskeletons and nuclear pore complex[134] are widely used as gold standard structures for the assessment of spatial and temporal resolution in the innovation of light microscopy technology. However, these structures are constitutively expressed and present in every cell types, they are thus relatively stationary in the range of milliseconds. There is a current demand on the application for the recent development of SIM techniques that have already reached the video-rate recording and on-the-fly display using GPU-acceleration for SIM reconstruction[80]. The advantage of using ASC specks for high-speed imaging is clear that the whole structure starts from nothing to a multiprotein complex in minutes and the speed of filament growth falls exactly into the millisecond scale. However, the entire speck may encompass up to 10 μm in z volume, we also need to increase the acquisition time of the volumetric image stacks. Simultaneous acquisition of multi-focus approaches, such as projection of different z-planes on single camera[2] or image-splitting prism implemented on SIM setups[23] might provide solutions for volumetric imaging at high speed. More insight on the development of inflammasomes can be envisaged as the dynamic processes of ASC filament formation are further unfolded when the combination of these new techniques is achieved. To this perspective, ASC specks are excellent samples with intricate structures for the characterization of the spatiotemporal resolution improvement of the recently advanced superresolution technology.

Bibliography

[1] Ernst Abbe. Beitraege zur theorie des mikroskops und der mikroskopischen-wahrnehmung. *Archive fuer Mikroskopische Anatomie*, IX:413–468, 1873.

[2] Sara Abrahamsson, Hans Blom, Ana Agostinho, Daniel C. Jans, Aurelie Jost, Marcel Müller, Linnea Nilsson, Kristoffer Bernhem, Talley J. Lambert, Rainer Heintzmann, and Hjalmar Brismar. Multifocus structured illumination microscopy for fast volumetric super-resolution imaging. *Biomedical optics express*, 8(9):4135–4140, 2017.

[3] George Biddell Airy. On the diffraction of an object-glass with circular aperture. *Trans. Cambridge Phils. Soc.*, 5:283–291, 1835.

[4] Shizuo Akira and Kiyoshi Takeda. Toll-like receptor signalling. *Nat. Rev. Immunol.*, 4(7):499–511, 2004.

[5] Albert Einstein. Zur quantentheorie der strahlung. *Physikalische Zeitschrift*, 18:121–128, 1917.

[6] Alexander Poltorak, Xiaolong He, Irina Smirnova, Mu-Ya Liu, Christophe Van Huffel, Xin Du, Dale Birdwell, Erica Alejos, Maria Silva, Chris Galanos, Marina Freudenberg, Paola Ricciardi-Castagnoli, Betsy Layton, Bruce Beutler. Defective lps signaling in mice mutations in tlr4 gene. *Science*, 282(5396):2085–2088, 1998.

[7] Ignacio Arganda-Carreras, Rodrigo Fernández-González, Arrate Muñoz-Barrutia, and Carlos Ortiz-De-Solorzano. 3d reconstruction of histological sections: Application to mammary gland tissue. *Microscopy research and technique*, 73(11):1019–1029, 2010.

[8] D. Axelrod. Total internal reflection fluorescence microscopy in cell biology. *Traffic*, 2(11):764–774, 2001.

[9] Graeme Ball, Justin Demmerle, Rainer Kaufmann, Ilan Davis, Ian M. Dobbie, and Lothar Schermelleh. Simcheck: a toolbox for successful super-resolution structured illumination microscopy. *Scientific reports*, 5:15915, 2015.

[10] Niccolò Banterle, Khanh Huy Bui, Edward A. Lemke, and Martin Beck. Fourier ring correlation as a resolution criterion for super-resolution microscopy. *Journal of structural biology*, 183(3):363–367, 2013.

[11] Tessa Bergsbaken, Susan L. Fink, and Brad T. Cookson. Pyroptosis: host cell death and inflammation. *Nature reviews. Microbiology*, 7(2):99–109, 2009.

[12] Carlos Morales Betanzos, Maria Gonzalez-Moa, Stephen Albert Johnston, and Sergei A. Svarovsky. Facile labeling of lipoglycans with quantum dots. *Biochemical and biophysical research communications*, 380(1):1–4, 2009.

[13] E. Betzig. Proposed method for molecular optical imaging. *Optics letters*, 20(3):237–239, 1995.

[14] Eric Betzig, George H. Patterson, Rachid Sougrat, O. Wolf Lindwasser, Scott Olenych, Juan S. Bonifacino, Michael W. Davidson, Jennifer Lippincott-Schwartz, and Harald F. Hess. Imaging intracellular fluorescent proteins at nanometer resolution. *Science (New York, N.Y.)*, 313(5793):1642–1645, 2006.

[15] Jun Cheng, Andrea L. Waite, Eric R. Tkaczyk, Kevin Ke, Neil Richards, Alan J. Hunt, and Deborah L. Gumucio. Kinetic properties of asc protein aggregation in epithelial cells. *Journal of cellular physiology*, 222(3):738–747, 2010.

[16] Jonathan Cohen. The immunopathogenesis of sepsis. *Nature*, 420(6917):885–891, 2002.

[17] Paula J. Cranfill, Brittney R. Sell, Michelle A. Baird, John R. Allen, Zeno Lavagnino, H. Martijn de Gruiter, Gert-Jan Kremers, Michael W. Davidson, Alessandro Ustione, and David W. Piston. Quantitative assessment of fluorescent proteins. *Nature methods*, 13(7):557–562, 2016.

[18] Christoph Cremer and Barry R. Masters. Resolution enhancement techniques in microscopy. *The European Physical Journal H*, 38(3):281–344, 2013.

[19] Daniele D'Alonzo, Manuela Cipolletti, Giulia Tarantino, Marcello Ziaco, Giuseppina Pieretti, Alfonso Iadonisi, Giovanni Palumbo, Alberto Alfano, Mariateresa Giuliano, Mario de Rosa, Chiara Schiraldi, Marcella Cammarota, Michelangelo Parrilli, Emiliano Bedini, and Maria M. Corsaro. A semisynthetic approach to new immunoadjuvant candidates: Site-selective chemical manipulation of escherichia coli monophosphoryl lipid a. *Chemistry (Weinheim an der Bergstrasse, Germany)*, 22(31):11053–11063, 2016.

[20] Justin Demmerle, Cassandravictoria Innocent, Alison J. North, Graeme Ball, Marcel Müller, Ezequiel Miron, Atsushi Matsuda, Ian M. Dobbie, Yolanda Markaki, and Lothar Schermelleh. Strategic and practical guidelines for successful structured illumination microscopy. *Nature Protocols*, 12(5):988–1010, 2017.

[21] Graham T. Dempsey, Joshua C. Vaughan, Kok Hao Chen, Mark Bates, and Xiaowei Zhuang. Evaluation of fluorophores for optimal performance in localization-based super-resolution imaging. *Nature methods*, 8(12):1027–1036, 2011.

[22] Thomas Dertinger, Ryan Colyer, Robert Vogel, Jörg Enderlein, and Shimon Weiss. Achieving increased resolution and more pixels with superresolution optical fluctuation imaging (sofi). *Optics express*, 18(18):18875–18885, 2010.

[23] Adrien Descloux, Marcel Müller, Vytautas Navikas, Andreas Markwirth, Robin van den Eynde, Tomas Lukes, Wolfgang Hübner, Theo Lasser, Aleksandra Radenovic, Peter Dedecker, and Thomas Huser. *High speed multiplane super-resolution structured illumination microscopy of living cells using an image-splitting prism.* 2019.

[24] Mathias S. Dick, Lorenzo Sborgi, Sebastian Rühl, Sebastian Hiller, and Petr Broz. Asc filament formation serves as a signal amplification mechanism for inflammasomes. *Nature communications*, 7:11929, 2016.

[25] Xiaofan Du, Jing Wang, Quan Zhou, Luwei Zhang, Sijia Wang, Zhenxi Zhang, and Cuiping Yao. Advanced physical techniques for gene delivery based on membrane perforation. *Drug delivery*, 25(1):1516–1525, 2018.

[26] Vincent Duheron, Mathieu Moreau, Bertrand Collin, Wahib Sali, Claire Bernhard, Christine Goze, Thomas Gautier, Jean-Paul Pais de Barros, Valérie Deckert, François Brunotte, Laurent Lagrost, and Franck Denat. Dual labeling of lipopolysaccharides for spect-ct imaging and fluorescence microscopy. *ACS chemical biology*, 9(3):656–662, 2014.

[27] T. Fernandes-Alnemri, J. Wu, J-W Yu, P. Datta, B. Miller, W. Jankowski, S. Rosenberg, J. Zhang, and E. S. Alnemri. The pyroptosome: a supramolecular assembly of asc dimers mediating inflammatory cell death via caspase-1 activation. *Cell death and differentiation*, 14(9):1590–1604, 2007.

[28] Reto Fiolka, Lin Shao, E. Hesper Rego, Michael W. Davidson, and Mats G. L. Gustafsson. Time-lapse two-color 3d imaging of live cells with doubled resolution using structured illumination. *Proceedings of the National Academy of Sciences of the United States of America*, 109(14):5311–5315, 2012.

[29] Katherine A. Fitzgerald, Daniel C. Rowe, Betsy J. Barnes, Daniel R. Caffrey, Alberto Visintin, Eicke Latz, Brian Monks, Paula M. Pitha, and Douglas T. Golenbock. Lps-tlr4 signaling to irf-3/7 and nf-kappab involves the toll adapters tram and trif. *The Journal of experimental medicine*, 198(7):1043–1055, 2003.

[30] Nicholas J. Gay, Monique Gangloff, and Luke A. J. O'Neill. What the myddosome structure tells us about the initiation of innate immunity. *Trends in immunology*, 32(3):104–109, 2011.

[31] Nicholas J. Gay, Martyn F. Symmons, Monique Gangloff, and Clare E. Bryant. Assembly and localization of toll-like receptor signalling complexes. *Nature reviews. Immunology*, 14(8):546–558, 2014.

[32] Jin Gohda, Takayuki Matsumura, and Jun-ichiro Inoue. Cutting edge: Tnfr-associated factor (traf) 6 is essential for myd88-dependent pathway but not toll/il-1 receptor domain-containing adaptor-inducing ifn-beta (trif)-dependent pathway in tlr signaling. *Journal of immunology (Baltimore, Md. : 1950)*, 173(5):2913–2917, 2004.

[33] M. Gossen, S. Freundlieb, G. Bender, G. Müller, W. Hillen, and H. Bujard. Transcriptional activation by tetracyclines in mammalian cells. *Science (New York, N.Y.)*, 268(5218):1766–1769, 1995.

[34] Alexei Grichine, Alexandre Haefele, Simon Pascal, Alain Duperray, Richard Michel, Chantal Andraud, and Olivier Maury. Millisecond lifetime imaging with a europium complex using a commercial confocal microscope under one or two-photon excitation. *Chem. Sci.*, 5(9):3475–3485, 2014.

[35] Yuting Guo, Di Li, Siwei Zhang, Yanrui Yang, Jia-Jia Liu, Xinyu Wang, Chong Liu, Daniel E. Milkie, Regan P. Moore, U. Serdar Tulu, Daniel P. Kiehart, Junjie Hu, Jennifer Lippincott-Schwartz, Eric Betzig, and Dong Li. Visualizing intracellular organelle and cytoskeletal interactions at nanoscale resolution on millisecond timescales. *Cell*, 175(5):1430–1442.e17, 2018.

[36] Zhiqian Guo, Gun-Hee Kim, Juyoung Yoon, and Injae Shin. Synthesis of a highly zn2+-selective cyanine-based probe and its use for tracing endogenous zinc ions in cells and organisms. *Nature Protocols*, 9(6):1245–1254, 2014.

[37] Zhiqian Guo, Sookil Park, Juyoung Yoon, and Injae Shin. Recent progress in the development of near-infrared fluorescent probes for bioimaging applications. *Chem. Soc. Rev.*, 43(1):16–29, 2014.

[38] M. G. Gustafsson. Surpassing the lateral resolution limit by a factor of two using structured illumination microscopy. *Journal of microscopy*, 198(Pt 2):82–87, 2000.

[39] Mats G. L. Gustafsson, Lin Shao, Peter M. Carlton, C. J. Rachel Wang, Inna N. Golubovskaya, W. Zacheus Cande, David A. Agard, and John W. Sedat. Three-dimensional resolution doubling in wide-field fluorescence microscopy by structured illumination. *Biophysical journal*, 94(12):4957–4970, 2008.

[40] Kelly M. Hatfield, Raymund B. Dantes, James Baggs, Mathew R. P. Sapiano, Anthony E. Fiore, John A. Jernigan, and Lauren Epstein. Assessing variability in hospital-level mortality among u.s. medicare beneficiaries with hospitalizations for severe sepsis and septic shock. *Critical care medicine*, 46(11):1753–1760, 2018.

[41] Kristin L. Hazelwood, Scott G. Olenych, John D. Griffin, Judith A. Cathcart, and Michael W. Davidson. Entering the portal: Understanding the digital image recorded through a microscope. In Spencer L. Shorte and Friedrich Frischknecht, editors, *Imaging Cellular and Molecular Biological Functions*, volume 361 of *Principles and Practice*, pages 3–43. Springer Berlin Heidelberg, Berlin, Heidelberg, 2007.

[42] Rainer Heintzmann and Christoph G. Cremer. Laterally modulated excitation microscopy: improvement of resolution by using a diffraction grating. In Irving J. Bigio, Herbert Schneckenburger, Jan Slavik, Katarina Svanberg, and Pierre M. Viallet, editors, *Optical Biopsies and Microscopic Techniques III*, SPIE Proceedings, pages 185–196. SPIE, 1999.

[43] Rainer Heintzmann and Gabriella Ficz. Breaking the resolution limit in light microscopy. *Briefings in functional genomics & proteomics*, 5(4):289–301, 2006.

[44] Rainer Heintzmann and Thomas Huser. Super-resolution structured illumination microscopy. *Chemical Reviews*, 117(23):13890–13908, 2017.

[45] S. W. Hell and J. Wichmann. Breaking the diffraction resolution limit by stimulated emission: stimulated-emission-depletion fluorescence microscopy. *Optics letters*, 19(11):780–782, 1994.

[46] Stefan W. Hell. Far-field optical nanoscopy. *Science (New York, N.Y.)*, 316(5828):1153–1158, 2007.

[47] Samuel T. Hess, Thanu P. K. Girirajan, and Michael D. Mason. Ultra-high resolution imaging by fluorescence photoactivation localization microscopy. *Biophysical journal*, 91(11):4258–4272, 2006.

[48] Michael Hofmann, Christian Eggeling, Stefan Jakobs, and Stefan W. Hell. Breaking the diffraction barrier in fluorescence microscopy at low light intensities by using reversibly photoswitchable proteins. *Proceedings of the National Academy of Sciences of the United States of America*, 102(49):17565–17569, 2005.

[49] Patrick D. Hsu, Eric S. Lander, and Feng Zhang. Development and applications of crispr-cas9 for genome engineering. *Cell*, 157(6):1262–1278, 2014.

[50] Bo Huang, Wenqin Wang, Mark Bates, and Xiaowei Zhuang. Three-dimensional super-resolution imaging by stochastic optical reconstruction microscopy. *Science (New York, N.Y.)*, 319(5864):810–813, 2008.

[51] Harald Husebye, Øyvind Halaas, Harald Stenmark, Gro Tunheim, Øystein Sandanger, Bjarne Bogen, Andreas Brech, Eicke Latz, and Terje Espevik. Endocytic pathways regulate toll-like receptor 4 signaling and link innate and adaptive immunity. *The EMBO Journal*, 25(4):683–692, 2006.

[52] Erik Huss and Annika Moberg. The nobel prize in chemistry 2008- press release.

[53] Yvonne Imielski, Jens C. Schwamborn, Patrick Lüningschrör, Peter Heimann, Magdalena Holzberg, Hendrikje Werner, Oliver Leske, Andreas W. Püschel, Sylvie Memet, Rolf Heumann, Alain Israel, Christian Kaltschmidt, and Barbara Kaltschmidt. Regrowing the adult brain: Nf-kb controls functional circuit formation and tissue homeostasis in the dentate gyrus. *PloS one*, 7(2):e30838, 2012.

[54] Zhengfan Jiang, Tak W. Mak, Ganes Sen, and Xiaoxia Li. Toll-like receptor 3-mediated activation of nf-kappab and irf3 diverges at toll-il-1 receptor domain-containing adapter inducing ifn-beta. *Proceedings of the National Academy of Sciences of the United States of America*, 101(10):3533–3538, 2004.

[55] John V Frangioni. In vivo near-infrared fluorescence imaging. *Curr. Opin. Chem. Biol.*, 7(5):626–634, 2003.

[56] Sara A. Jones, Sang-Hee Shim, Jiang He, and Xiaowei Zhuang. Fast, three-dimensional super-resolution imaging of live cells. *Nature methods*, 8(6):499–508, 2011.

[57] Jonathan C. Kagan, Venkat Giri Magupalli, and Hao Wu. Smocs: supramolecular organizing centres that control innate immunity. *Nature reviews. Immunology*, 14(12):821–826, 2014.

[58] Jonathan C. Kagan, Tian Su, Tiffany Horng, Amy Chow, Shizuo Akira, and Ruslan Medzhitov. Tram couples endocytosis of toll-like receptor 4 to the induction of interferon-beta. *Nature immunology*, 9(4):361–368, 2008.

[59] T. Kawai, O. Takeuchi, T. Fujita, J. Inoue, P. F. Mühlradt, S. Sato, K. Hoshino, and S. Akira. Lipopolysaccharide stimulates the myd88-independent pathway and results in activation of ifn-regulatory factor 3 and the expression of a subset of lipopolysaccharide-inducible genes. *Journal of immunology (Baltimore, Md. : 1950)*, 167(10):5887–5894, 2001.

[60] Meng-Tsen Ke and Takeshi Imai. Optical clearing and index matching of tissue samples for high-resolution fluorescence imaging using seedb2. *BIO-PROTOCOL*, 8(20), 2018.

[61] Meng-Tsen Ke, Yasuhiro Nakai, Satoshi Fujimoto, Rie Takayama, Shuhei Yoshida, Tomoya S. Kitajima, Makoto Sato, and Takeshi Imai. Super-resolution mapping of neuronal circuitry with an index-optimized clearing agent. *Cell reports*, 14(11):2718–2732, 2016.

[62] Antje Keppler, Susanne Gendreizig, Thomas Gronemeyer, Horst Pick, Horst Vogel, and Kai Johnsson. A general method for the covalent labeling of fusion proteins with small molecules in vivo. *Nature biotechnology*, 21(1):86–89, 2003.

[63] Dionne C. G. Klein, Astrid Skjesol, Esther D. Kers-Rebel, Tatyana Sherstova, Bjørnar Sporsheim, Kjartan W. Egeberg, Bjørn T. Stokke, Terje Espevik, and Harald Husebye. Cd14, tlr4 and tram show different trafficking dynamics during lps stimulation. *Traffic*, 16(7):677–690, 2015.

[64] Carmen L. Krüger, Marie-Theres Zeuner, Graeme S. Cottrell, Darius Widera, and Mike Heilemann. Quantitative single-molecule imaging of tlr4 reveals ligand-specific receptor dimerization. *Science signaling*, 10(503), 2017.

[65] Paola Kuri, Nicole L. Schieber, Thomas Thumberger, Joachim Wittbrodt, Yannick Schwab, and Maria Leptin. Dynamics of in vivo asc speck formation. *The Journal of cell biology*, 216(9):2891–2909, 2017.

[66] Joseph R. Lakowicz. *Principles of Fluorescence Spectroscopy*. Springer US, Boston, MA, 2006.

[67] Mohamed Lamkanfi and Vishva M. Dixit. The inflammasome turns 15. *Nature*, 548:534 EP –, 2017.

[68] Emma Lång, Anna Połeć, Anna Lång, Marijke Valk, Pernille Blicher, Alexander D. Rowe, Kim A. Tønseth, Catherine J. Jackson, Tor P. Utheim, Liesbeth M. C. Janssen, Jens Eriksson, and Stig Ove Bøe. Coordinated collective migration and asymmetric cell division in confluent human keratinocytes without wounding. *Nature communications*, 9(1):3665, 2018.

[69] Eicke Latz, Alberto Visintin, Egil Lien, Kate A. Fitzgerald, Brian G. Monks, Evelyn A. Kurt-Jones, Douglas T. Golenbock, and Terje Espevik. Lipopolysaccharide rapidly traffics to and from the golgi apparatus with the toll-like receptor 4-md-2-cd14 complex in a process that is distinct from the initiation of signal transduction. *Journal of Biological Chemistry*, 277(49):47834–47843, 2002.

[70] Eicke Latz, T. Sam Xiao, and Andrea Stutz. Activation and regulation of the inflammasomes. *Nature reviews. Immunology*, 13(6):397–411, 2013.

[71] Dong Li, Lin Shao, Bi-Chang Chen, Xi Zhang, Mingshu Zhang, Brian Moses, Daniel E. Milkie, Jordan R. Beach, John A. Hammer, Mithun Pasham, Tomas Kirchhausen, Michelle A. Baird, Michael W. Davidson, Pingyong Xu, and Eric Betzig. Advanced imaging. extended-resolution structured illumination imaging of endocytic and cytoskeletal dynamics. *Science (New York, N.Y.)*, 349(6251):aab3500, 2015.

[72] Su-Chang Lin, Yu-Chih Lo, and Hao Wu. Helical assembly in the myd88-irak4-irak2 complex in tlr/il-1r signalling. *Nature*, 465(7300):885–890, 2010.

[73] Jennifer Lippincott-Schwartz and George H. Patterson. Photoactivatable fluorescent proteins for diffraction-limited and super-resolution imaging. *Trends in cell biology*, 19(11):555–565, 2009.

[74] H. Loppnow, P. Libby, M. Freudenberg, J. H. Krauss, J. Weckesser, and H. Mayer. Cytokine induction by lipopolysaccharide (lps) corresponds to lethal toxicity and is inhibited by nontoxic rhodobacter capsulatus lps. *Infection and Immunity*, 58(11):3743–3750, 1990.

[75] Georgyi V. Los, Lance P. Encell, Mark G. McDougall, Danette D. Hartzell, Natasha Karassina, Chad Zimprich, Monika G. Wood, Randy Learish, Rachel Friedman Ohana, Marjeta Urh, Dan Simpson, Jacqui Mendez, Kris Zimmerman, Paul Otto, Gediminas Vidugiris, Ji Zhu, Aldis Darzins, Dieter H. Klaubert, Robert F. Bulleit, and Keith V. Wood. Halotag: a novel protein labeling technology for cell imaging and protein analysis. *ACS Chemical Biology*, 3(6):373–382, 2008.

[76] Céline Loussert Fonta and Bruno M. Humbel. Correlative microscopy. *Archives of biochemistry and biophysics*, 581:98–110, 2015.

[77] Alvin Lu, Venkat Giri Magupalli, Jianbin Ruan, Qian Yin, Maninjay K. Atianand, Matthijn R. Vos, Gunnar F. Schröder, Katherine A. Fitzgerald, Hao Wu, and Edward H. Egelman. Unified polymerization mechanism for the assembly of asc-dependent inflammasomes. *Cell*, 156(6):1193–1206, 2014.

[78] L. B. Lucy. An iterative technique for the rectification of observed distributions. *The Astronomical Journal*, 79:745, 1974.

[79] Carlo Manzo and Maria F. Garcia-Parajo. A review of progress in single particle tracking: from methods to biophysical insights. *Reports on progress in physics. Physical Society (Great Britain)*, 78(12):124601, 2015.

[80] Andreas Markwirth, Mario Lachetta, Viola Mönkemöller, Rainer Heintzmann, Wolfgang Hübner, Thomas Huser, and Marcel Müller. Video-rate multi-color structured illumination microscopy with simultaneous real-time reconstruction. *Nature communications*, 10(1):4315, 2019.

[81] W. T. Mason. *Fluorescent and luminescent probes for biological activity: A practical guide to technology for quantitative real-time analysis*. Biological techniques. Academic Press, San Diego, Calif, 2nd ed. edition, 2010.

[82] J. Masumoto, S. Taniguchi, K. Ayukawa, H. Sarvotham, T. Kishino, N. Niikawa, E. Hidaka, T. Katsuyama, T. Higuchi, and J. Sagara. Asc, a novel 22-kda protein, aggregates during apoptosis of human promyelocytic leukemia hl-60 cells. *The Journal of biological chemistry*, 274(48):33835–33838, 1999.

[83] Xiaoqing Meng, Yueting Yang, Lihua Zhou, li Zhang, Yalin Lv, Sanpeng Li, Yayun Wu, Mingbin Zheng, Wenjun Li, Guanhui Gao, Guanjun Deng, Tao Jiang, Dapeng Ni, Ping Gong, and Lintao Cai. Dual-responsive molecular probe for tumor targeted imaging and photodynamic therapy. *Theranostics*, 7(7):1781–1794, 2017.

[84] Londiwe S. Mgcina, Ian A. Dubery, and Lizelle A. Piater. Comparative conventional- and quantum dot-labeling strategies for lps binding site detection in arabidopsis thaliana mesophyll protoplasts. *Frontiers in plant science*, 6:335, 2015.

[85] M. Minsky. Memoir on inventing the confocal scanning microscope. *Scanning*, 10(4):128–138, 1988.

[86] Tom Monie. *The Innate Immune System: A Compositional and Functional Perspective*. Elsevier Ltd, Place of publication not identified and s.l., 2017.

[87] Marcel Müller, Viola Mönkemöller, Simon Hennig, Wolfgang Hübner, and Thomas Huser. Open-source image reconstruction of super-resolution structured illumination microscopy data in imagej. *Nature communications*, 7:10980, 2016.

[88] Leila Nahidiazar, Alexandra V. Agronskaia, Jorrit Broertjes, Bram van den Broek, and Kees Jalink. Optimizing imaging conditions for demanding multi-color super resolution localization microscopy. *PloS one*, 11(7):e0158884, 2016.

[89] Jessica Nannini and Mans Ehrenberg. The nobel prize in chemistry 2014-press release: for the development of super-resolved fluorescence microscopy.

[90] Jan Neumann, Kira Ziegler, Márton Gelléri, Janine Fröhlich-Nowoisky, Fobang Liu, Iris Bellinghausen, Detlef Schuppan, Udo Birk, Ulrich Pöschl, Christoph Cremer, and Kurt Lucas. Nanoscale distribution of tlr4 on primary human macrophages stimulated with lps and ati. *Nanoscale*, 11(19):9769–9779, 2019.

[91] Robert P. J. Nieuwenhuizen, Keith A. Lidke, Mark Bates, Daniela Leyton Puig, David Grünwald, Sjoerd Stallinga, and Bernd Rieger. Measuring image resolution in optical nanoscopy. *Nature methods*, 10(6):557–562, 2013.

[92] Costyl N. Njiojob, Eric A. Owens, Lakshminarayana Narayana, Hoon Hyun, Hak Soo Choi, and Maged Henary. Tailored near-infrared contrast agents for image guided surgery. *Journal of Medicinal Chemistry*, 58(6):2845–2854, 2015.

[93] Steven M. Opal. Endotoxins and other sepsis triggers. *Contributions to nephrology*, 167:14–24, 2010.

[94] Michel Orrit. Celebrating optical nanoscopy. *Nature Photonics*, 8(12):887–888, 2014.

[95] Beom Seok Park, Dong Hyun Song, Ho Min Kim, Byong-Seok Choi, Hayyoung Lee, and Jie-Oh Lee. The structural basis of lipopolysaccharide recognition by the tlr4-md-2 complex. *Nature*, 458(7242):1191–1195, 2009.

[96] Simon Pascal, Sandrine Denis-Quanquin, Florence Appaix, Alain Duperray, Alexei Grichine, Boris Le Guennic, Denis Jacquemin, Jérôme Cuny, San-Hui Chi, Joseph W. Perry, Boudewijn van der Sanden, Cyrille Monnereau, Chantal Andraud, and Olivier Maury. Keto-polymethines: a versatile class of dyes with outstanding spectroscopic properties for in cellulo and in vivo two-photon microscopy imaging. *Chemical science*, 8(1):381–394, 2017.

[97] Simon Pascal, Alexandre Haefele, Cyrille Monnereau, Azzam Charaf-Eddin, Denis Jacquemin, Boris Le Guennic, Chantal Andraud, and Olivier Maury.

Expanding the polymethine paradigm: evidence for the contribution of a bis-dipolar electronic structure. *The journal of physical chemistry. A*, 118(23):4038–4047, 2014.

[98] James B. Pawley, editor. *Handbook Of Biological Confocal Microscopy*. Springer US, Boston, MA, 2006.

[99] Xiaojun Peng, Fengling Song, Erhu Lu, Yanan Wang, Wei Zhou, Jiangli Fan, and Yunling Gao. Heptamethine cyanine dyes with a large stokes shift and strong fluorescence: a paradigm for excited-state intramolecular charge transfer. *Journal of the American Chemical Society*, 127(12):4170–4171, 2005.

[100] Victor Perez, Bo-Jui Chang, and Ernst Hans Karl Stelzer. Optimal 2d-sim reconstruction by two filtering steps with richardson-lucy deconvolution. *Scientific reports*, 6:37149, 2016.

[101] Francesco Peri and Matteo Piazza. Therapeutic targeting of innate immunity with toll-like receptor 4 (tlr4) antagonists. *Biotechnology advances*, 30(1):251–260, 2012.

[102] Antonio Z. Politi, Yin Cai, Nike Walther, M. Julius Hossain, Birgit Koch, Malte Wachsmuth, and Jan Ellenberg. Quantitative mapping of fluorescently tagged cellular proteins using fcs-calibrated four-dimensional imaging. *Nature Protocols*, 13(6):1445–1464, 2018.

[103] Daniela Puzzo, Jole Fiorito, Rosita Purgatorio, Walter Gulisano, Agostino Palmeri, Ottavio Arancio, and Russell Nicholls. Molecular mechanisms of learning and memory**the authors declare no competing financial interests. In *Genes, Environment and Alzheimer's Disease*, pages 1–27. Elsevier, 2016.

[104] F. Ann Ran, Patrick D. Hsu, Jason Wright, Vineeta Agarwala, David A. Scott, and Feng Zhang. Genome engineering using the crispr-cas9 system. *Nature Protocols*, 8(11):2281–2308, 2013.

[105] L. Rayleigh. On the theory of optical images, with special reference to the microscope. *The London, Edinburgh, and Dublin Philosophical Magazine and Journal of*, XV:167–195, 1896.

[106] Konrad Reinhart, Ron Daniels, Niranjan Kissoon, Flavia R. Machado, Raymond D. Schachter, and Simon Finfer. Recognizing sepsis as a global health priority - a who resolution. *The New England journal of medicine*, 377(5):414–417, 2017.

[107] Malte Renz. Fluorescence microscopy-a historical and technical perspective. *Cytometry. Part A : the journal of the International Society for Analytical Cytology*, 83(9):767–779, 2013.

[108] Douglas S. Richardson and Jeff W. Lichtman. Clarifying tissue clearing. *Cell*, 162(2):246–257, 2015.

[109] William Hadley Richardson. Bayesian-based iterative method of image restoration*. *Journal of the Optical Society of America*, 62(1):55, 1972.

[110] Charles V. Rosadini and Jonathan C. Kagan. Early innate immune responses to bacterial lps. *Curr. Opin. Immunol.*, 44:14–19, 2017.

[111] Michael J. Rust, Mark Bates, and Xiaowei Zhuang. Sub-diffraction-limit imaging by stochastic optical reconstruction microscopy (storm). *Nature methods*, 3(10):793–795, 2006.

[112] Je-Kyung Ryu, Soo Jin Kim, Sang-Hyun Rah, Ji In Kang, Hi Eun Jung, Dongsun Lee, Heung Kyu Lee, Jie-Oh Lee, Beom Seok Park, Tae-Young Yoon, and Ho Min Kim. Reconstruction of lps transfer cascade reveals structural determinants within lbp, cd14, and tlr4-md2 for efficient lps recognition and transfer. *Immunity*, 46(1):38–50, 2017.

[113] Ali Can Sahillioglu, Fidan Sumbul, Nesrin Ozoren, and Turkan Haliloglu. Structural and dynamics aspects of asc speck assembly. *Structure (London, England : 1993)*, 22(12):1722–1734, 2014.

[114] Steffen J. Sahl, Stefan W. Hell, and Stefan Jakobs. Fluorescence nanoscopy in cell biology. *Nature reviews. Molecular cell biology*, 18(11):685–701, 2017.

[115] Samuel D. Wright, Robert A. Ramos, Peter S. Tobias, Richard J. Ulevitch, John C. Mathison. Cd14, a receptor for complexes of lipopolysaccharide (lps) and lps. *Science*, 249(4975):1431–1433, 1990.

[116] Kazuaki Sawada, Ryosuke Kawakami, Ryuichi Shigemoto, and Tomomi Nemoto. Super-resolution structural analysis of dendritic spines using three-dimensional structured illumination microscopy in cleared mouse brain slices. *The European journal of neuroscience*, 47(9):1033–1042, 2018.

[117] Lorenzo Sborgi, Francesco Ravotti, Venkata P. Dandey, Mathias S. Dick, Adam Mazur, Sina Reckel, Mohamed Chami, Sebastian Scherer, Matthias Huber, Anja Böckmann, Edward H. Egelman, Henning Stahlberg, Petr Broz,

Beat H. Meier, and Sebastian Hiller. Structure and assembly of the mouse asc inflammasome by combined nmr spectroscopy and cryo-electron microscopy. *Proceedings of the National Academy of Sciences of the United States of America*, 112(43):13237–13242, 2015.

[118] Lothar Schermelleh, Peter M. Carlton, Sebastian Haase, Lin Shao, Lukman Winoto, Peter Kner, Brian Burke, M. Cristina Cardoso, David A. Agard, Mats G. L. Gustafsson, Heinrich Leonhardt, and John W. Sedat. Subdiffraction multicolor imaging of the nuclear periphery with 3d structured illumination microscopy. *Science (New York, N.Y.)*, 320(5881):1332–1336, 2008.

[119] Lothar Schermelleh, Rainer Heintzmann, and Heinrich Leonhardt. A guide to super-resolution fluorescence microscopy. *The Journal of cell biology*, 190(2):165–175, 2010.

[120] Florian I. Schmidt, Alvin Lu, Jeff W. Chen, Jianbin Ruan, Catherine Tang, Hao Wu, and Hidde L. Ploegh. A single domain antibody fragment that recognizes the adaptor asc defines the role of asc domains in inflammasome assembly. *The Journal of experimental medicine*, 213(5):771–790, 2016.

[121] Katharina S. Schneider, Christina J. Groß, Roland F. Dreier, Benedikt S. Saller, Ritu Mishra, Oliver Gorka, Rosalie Heilig, Etienne Meunier, Mathias S. Dick, Tamara Ćiković, Jan Sodenkamp, Guillaume Médard, Ronald Naumann, Jürgen Ruland, Bernhard Kuster, Petr Broz, and Olaf Groß. The inflammasome drives gsdmd-independent secondary pyroptosis and il-1 release in the absence of caspase-1 protease activity. *Cell reports*, 21(13):3846–3859, 2017.

[122] Humayun Sharif, Li Wang, Wei Li Wang, Venkat Giri Magupalli, Liudmila Andreeva, Qi Qiao, Arthur V. Hauenstein, Zhaolong Wu, Gabriel Núñez, Youdong Mao, and Hao Wu. Structural mechanism for nek7-licensed activation of nlrp3 inflammasome. *Nature*, 570(7761):338–343, 2019.

[123] Deepika Sharma and Thirumala-Devi Kanneganti. The cell biology of inflammasomes: Mechanisms of inflammasome activation and regulation. *The Journal of cell biology*, 213(6):617–629, 2016.

[124] Zhenhua Shen, Bijeta Prasai, Yuko Nakamura, Hisataka Kobayashi, Milcah S. Jackson, and Robin L. McCarley. A near-infrared, wavelength-shiftable, turn-on fluorescent probe for the detection and imaging of cancer tumor cells. *ACS Chemical Biology*, 12(4):1121–1132, 2017.

[125] Ludovico Silvestri, Irene Costantini, Leonardo Sacconi, and Francesco Saverio Pavone. Clearing of fixed tissue: a review from a microscopist's perspective. *Journal of biomedical optics*, 21(8):081205, 2016.

[126] Christoph Sommer, Christoph Straehle, Ullrich Kothe, and Fred A. Hamprecht. Ilastik: Interactive learning and segmentation toolkit. In *2011 IEEE International Symposium on Biomedical Imaging: From Nano to Macro*, pages 230–233. IEEE, 3/30/2011 - 4/2/2011.

[127] C. Sparrow. On the spectroscopic resolving power. *Astrophysical Journal*, 44:76–86, 1916.

[128] Florian Ströhl and Clemens F. Kaminski. Frontiers in structured illumination microscopy. *Optica*, 3(6):667, 2016.

[129] Chunlong Sun, Peng Wang, Lushen Li, Gaoxin Zhou, Xi Zong, Bing Hu, Rui Zhang, Jin Cai, Junqing Chen, and Min Ji. A new near-infrared neutral ph fluorescent probe for monitoring minor ph changes and its application in imaging of hepg2 cells. *Applied Biochemistry and Biotechnology*, 172(2):1036–1044, 2014.

[130] Yunhao Tan and Jonathan C. Kagan. A cross-disciplinary perspective on the innate immune responses to bacterial lipopolysaccharide. *Molecular cell*, 54(2):212–223, 2014.

[131] Yunhao Tan and Jonathan C. Kagan. Microbe-inducible trafficking pathways that control toll-like receptor signaling. *Traffic*, 18(1):6–17, 2017.

[132] Yunhao Tan, Ivan Zanoni, Thomas W. Cullen, Andrew L. Goodman, and Jonathan C. Kagan. Mechanisms of toll-like receptor 4 endocytosis reveal a common immune-evasion strategy used by pathogenic and commensal bacteria. *Immunity*, 43(5):909–922, 2015.

[133] Natsuko Tanimura, Shinichiroh Saitoh, Fumi Matsumoto, Sachiko Akashi-Takamura, and Kensuke Miyake. Roles for lps-dependent interaction and relocation of tlr4 and tram in trif-signaling. *Biochem. Biophys. Res. Commun.*, 368(1):94–99, 2008.

[134] Jervis Vermal Thevathasan, Maurice Kahnwald, Konstanty Cieśliński, Philipp Hoess, Sudheer Kumar Peneti, Manuel Reitberger, Daniel Heid, Krishna Chaitanya Kasuba, Sarah Janice Hoerner, Yiming Li, Yu-Le Wu,

Markus Mund, Ulf Matti, Pedro Matos Pereira, Ricardo Henriques, Bianca Nijmeijer, Moritz Kueblbeck, Vilma Jimenez Sabinina, Jan Ellenberg, and Jonas Ries. Nuclear pores as versatile reference standards for quantitative superresolution microscopy. *Nature methods*, 16(10):1045–1053, 2019.

[135] Nathalie Thieblemont, Rolf Thieringer, and Samuel D. Wright. Innate immune recognition of bacterial lipopolysaccharide: Dependence on interactions with membrane lipids and endocytic movement. *Immunity*, 8(6):771–777, 1998.

[136] Makio Tokunaga, Naoko Imamoto, and Kumiko Sakata-Sogawa. Highly inclined thin illumination enables clear single-molecule imaging in cells. *Nature methods*, 5(2):159–161, 2008.

[137] Kathy Triantafilou, Martha Triantafilou, and Nelson Fernandez. Lipopolysaccharide (lps) labeled with alexa 488 hydrazide as a novel probe for lps binding studies. *Cytometry*, 41(4):316–320, 2000.

[138] A. Troelstra, P. Antal-Szalmas, L. Graaf-Miltenburg, A. Weersink, J. Verhoef, K. van Kessel, and Van Strijp. Saturable cd14-dependent binding of fluorescein-labeled lipopolysaccharide to human monocytes. *Infect. Immun.*, 65(6):2272–2277, 1997.

[139] Taka A. Tsunoyama, Yusuke Watanabe, Junri Goto, Kazuma Naito, Rinshi S. Kasai, Kenichi G. N. Suzuki, Takahiro K. Fujiwara, and Akihiro Kusumi. Super-long single-molecule tracking reveals dynamic-anchorage-induced integrin function. *Nature chemical biology*, 14(5):497–506, 2018.

[140] Raphaël Turcotte, Yajie Liang, Masashi Tanimoto, Qinrong Zhang, Ziwei Li, Minoru Koyama, Eric Betzig, and Na Ji. Dynamic super-resolution structured illumination imaging in the living brain. *Proceedings of the National Academy of Sciences of the United States of America*, 116(19):9586–9591, 2019.

[141] Bernard Valeur. *Molecular Fluorescence*. Wiley, 2001.

[142] Sebastian van de Linde, Anna Löschberger, Teresa Klein, Meike Heidbreder, Steve Wolter, Mike Heilemann, and Markus Sauer. Direct stochastic optical reconstruction microscopy with standard fluorescent probes. *Nature Protocols*, 6(7):991–1009, 2011.

[143] J. Vangindertael, R. Camacho, W. Sempels, H. Mizuno, P. Dedecker, and K. P. F. Janssen. An introduction to optical super-resolution microscopy for the adventurous biologist. *Methods and applications in fluorescence*, 6(2):022003, 2018.

[144] Vasselon T., E. Hailman, R. Thieringer, and P. A. Detmers. Internalization of monomeric lipopolysaccharide occurs after transfer out of cell surface cd14. *J. Exp. Med.*, 190(4):509–521, 1999.

[145] Alex von Diezmann, Yoav Shechtman, and W. E. Moerner. Three-dimensional localization of single molecules for super-resolution imaging and single-particle tracking. *Chemical Reviews*, 117(11):7244–7275, 2017.

[146] Shenshen Wang and Peter G. Wolynes. Active contractility in actomyosin networks. *Proceedings of the National Academy of Sciences of the United States of America*, 109(17):6446–6451, 2012.

[147] Tung-Cheng Wang, Florent Cochet, Fabio Alessandro Facchini, Lenny Zaffaroni, Christelle Serba, Simon Pascal, Chantal Andraud, Andrea Sala, Flaviana Di Lorenzo, Olivier Maury, Thomas Huser, and Francesco Peri. Synthesis of the new cyanine-labeled bacterial lipooligosaccharides for intracellular imaging and in vitro microscopy studies. *Bioconjugate chemistry*, 30(6):1649–1657, 2019.

[148] Chris Whitfield and M. Stephen Trent. Biosynthesis and export of bacterial lipopolysaccharides. *Annual review of biochemistry*, 83:99–128, 2014.

[149] Norbert Wiener. *Extrapolation, interpolation, and smoothing of stationary time series: With engineering applications.* Technology Press of the Massachusetts Institute of Technology, Cambridge, 1960.

[150] Charles S. William and Orville A. Becklund. *Introduction to the Optical Transfer Function.* Wiley-Interscience, New York, 2002.

[151] T. Wilson. Resolution and optical sectioning in the confocal microscope. *Journal of microscopy*, 244(2):113–121, 2011.

[152] Peter W. Winter, Andrew G. York, Damian Dalle Nogare, Maria Ingaramo, Ryan Christensen, Ajay Chitnis, George H. Patterson, and Hari Shroff. Two-photon instant structured illumination microscopy improves the depth penetration of super-resolution imaging in thick scattering samples. *Optica*, 1(3):181–191, 2014.

[153] Yicong Wu and Hari Shroff. Faster, sharper, and deeper: structured illumination microscopy for biological imaging. *Nature methods*, 15(12):1011–1019, 2018.

[154] Qiang Yang, Liangcai Cao, Hua Zhang, Hao Zhang, and Guofan Jin. Method of lateral image reconstruction in structured illumination microscopy with super resolution. *Journal of Innovative Optical Health Sciences*, 09(03):1630002, 2016.

[155] Swee Kuan Yen, Dominik Jańczewski, Jeeva Lavanya Lakshmi, Surani Bin Dolmanan, Sudhiranjan Tripathy, Vincent H. B. Ho, Vimalan Vijayaragavan, Anushya Hariharan, Parasuraman Padmanabhan, Kishore K. Bhakoo, Thankiah Sudhaharan, Sohail Ahmed, Yong Zhang, and Subramanian Tamil Selvan. Design and synthesis of polymer-functionalized nir fluorescent dyes–magnetic nanoparticles for bioimaging. *ACS Nano*, 7(8):6796–6805, 2013.

[156] Bo Yu and Samuel D. Wright. Catalytic properties of lipopolysaccharide (lps) binding protein. *Journal of Biological Chemistry*, 271(8):4100–4105, 1996.

[157] Lin Yuan, Weiying Lin, Kaibo Zheng, Longwei He, and Weimin Huang. Far-red to near infrared analyte-responsive fluorescent probes based on organic fluorophore platforms for fluorescence imaging. *Chem. Soc. Rev.*, 42(2):622–661, 2013.

[158] Ivan Zanoni, Caterina Bodio, Achille Broggi, Renato Ostuni, Michele Caccia, Maddalena Collini, Aparna Venkatesh, Roberto Spreafico, Giusy Capuano, and Francesca Granucci. Similarities and differences of innate immune responses elicited by smooth and rough lps. *Immunol. Lett.*, 142(1-2):41–47, 2012.

[159] Ivan Zanoni, Renato Ostuni, Lorri R. Marek, Simona Barresi, Roman Barbalat, Gregory M. Barton, Francesca Granucci, and Jonathan C. Kagan. Cd14 controls the lps-induced endocytosis of toll-like receptor 4. *Cell*, 147(4):868–880, 2011.

[160] Marie-Theres Zeuner, Carmen L. Krüger, Katharina Volk, Karen Bieback, Graeme S. Cottrell, Mike Heilemann, and Darius Widera. Biased signalling is an essential feature of tlr4 in glioma cells. *Biochimica et biophysica acta*, 1863(12):3084–3095, 2016.

[161] Liman Zhang, Shuobing Chen, Jianbin Ruan, Jiayi Wu, Alexander B. Tong, Qian Yin, Yang Li, Liron David, Alvin Lu, Wei Li Wang, Carolyn Marks, Qi Ouyang, Xinzheng Zhang, Youdong Mao, and Hao Wu. Cryo-em structure of the activated naip2-nlrc4 inflammasome reveals nucleated polymerization. *Science (New York, N.Y.)*, 350(6259):404–409, 2015.

[162] Xi Zhang, Xuanze Chen, Zhiping Zeng, Mingshu Zhang, Yujie Sun, Peng Xi, Jianxin Peng, and Pingyong Xu. Development of a reversibly switchable fluorescent protein for super-resolution optical fluctuation imaging (sofi). *ACS Nano*, 9(3):2659–2667, 2015.

[163] Mingming Zhu, Chuanxing Shi, Xitao Xu, Zhiqian Guo, and Weihong Zhu. Near-infrared cyanine-based sensor for fe 3+ with high sensitivity: its intracellular imaging application in colorectal cancer cells. *RSC Advances*, 6(103):100759–100764, 2016.

BIBLIOGRAPHY

Appendix A

Materials and methods

3D-SIM microscope

Delta Vision OMX (Optical Microscope eXperimental) Blaze-V4 (GE Healthcare, USA) is used to acquire wide-field, TIRF, and 3D-SIM images. It is equipped with five laser lines (405, 488, 514, 568, 642nm) for excitation and the emitted fluorescence can be collected with up to four detection channels (Blue: 463/31; Green: 528/48; Orange: 609/37; Red: 683/40), each of which is detected by an independent scientific CMOS cameras (customized PCO Edge). For the SIM imaging, the Olympus Plan-Apo N 60x/1.42 oil objective is mainly used. The excitation pathway begins from the joining of all excitation lines into a single beam path that is either blocked by a safety shutter or directed into one of the two optical fibers. One is used in SIM imaging, the other is used in wide-field and TIRF illumination.

In SIM mode (Figure A.1), the laser light guided from the fiber end is first passed through the grating to create diffraction rays (-1, 0, -1) used for 3-beam interference. The two side-rays (-1, 1) are phase-delayed by individually passing through a pair of glass plates to create the additional phase shifts relative to the central beam (0-order) but keep the beam paths stay in the default positions without lateral shifts. For calibration, one side-ray instead of two is adjusted with the phase delay device to find the best contrast of the peak-to-trough in the focal plane, so called "Top-phase" alignment of the 3D pattern. A few sets of galvanometer mirrors

then project the diffraction rays into three different angular orientations on the back aperture of the objective. All the interference beams are kept constant in s-polarization from the polarization-maintained optical fiber to the objective back aperture in order to get the best modulation contrast of the 3-beam interference. A total of 15 image frames are recorded in a single z-slice and the Nanomover stage drives the sample up or down to record other z positions in the entire 3D volume in the step size of 125nm to fulfill the Nyquist theorem. The acquired images are sent into a separated computer for SIM reconstruction. The system's built-in software, softworx, is used to generate the 3D-SIM images. fairSIM is also used to extract 2D-SIM images from the 3D raw data obtained from OMX[87]. In addition, the refraction index of the oil applied on the microscope objective needs to be optimized to individual specimens, it typically ranges from 1.512 to 1.524, depending on the sample medium, focus depth and the recorded wavelengths.

As for the TIRF illumination modes, a high NA objective (Olympus Apo N 60x/1.49 oil) is used and with the aid of another optical fiber that leads (not shown in Figure A.1) the combined laser beams into the Ring TIRF module where the incident angle of the excitation light can be adjusted by laterally shifting the focus beam laterally on the pupil plane to reach HILO or TIRF angles. A set of galvanometer scanning mirrors is exploited in this module to illuminate the sample with tunable incident angles while rapidly rotates the focus beam around the pupil center to create a homogeneous TIRF illumination in all directions. Single-molecule detection is recorded by TIRF mode and the trajectories of single fluorophores were analyzed by Trackmate plugin in Fiji.

Deconvolution microscope

Although the OMX is also capable of deconvolution imaging, the DeltaVision Elite microscope (GE Healthcare, USA) is preferred for the deconvolution tasks, because the latter has an incubation chamber to maintain 37°C in which the living cells can be kept longer for the time-lapse recording. The system is built upon the Olympus microscope stand and thus equipped with various objectives, for example, the silicon (Olympus UPlansSApo 60x/1.3 Sil), water objectives (Olympus UPLanSApo 60x/1.20 W) and the same oil objective used on OMX. The OTFs required for deconvolution are chosen from the list of system database accordingly. The z volume is recorded generally in z-step of 250nm. The raw images are acquired by a charge-couple device (CCD) camera (Coolsnap, Photometrics) with

the corresponding filtersets.

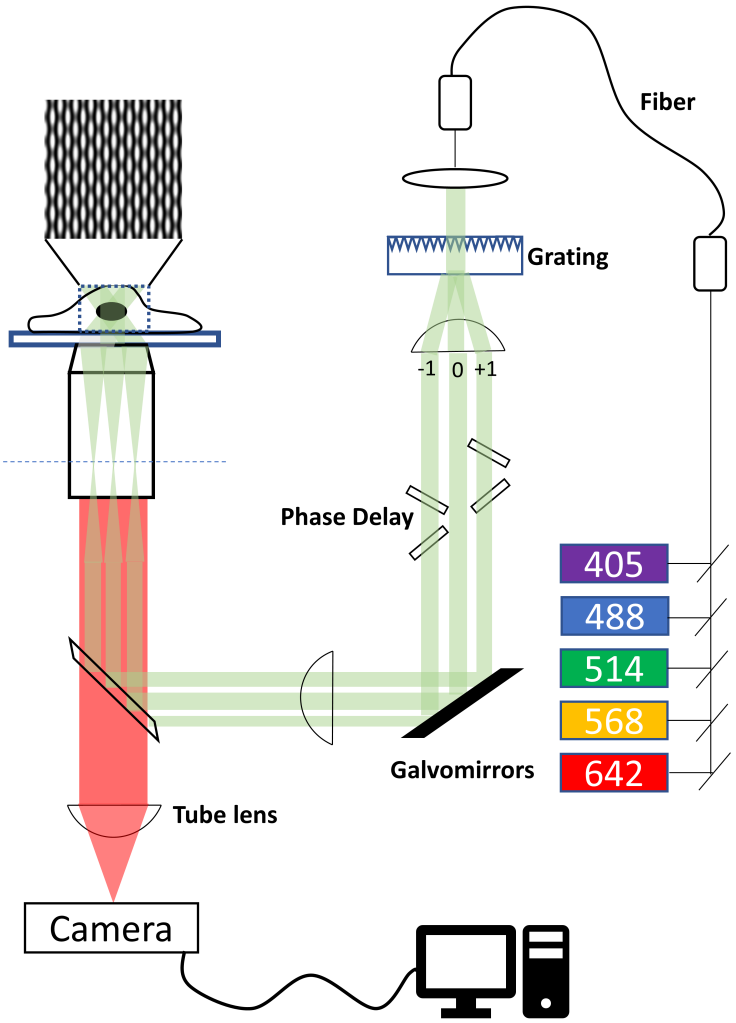

Figure A.1: Schematic architecture of the OMX 3D-SIM system. The exact microscope setup has to be referred to technical support of GE healthcare.

LPS imaging

HEK-293 and U2OS cells were cultured in DMEM supplemented with 10% FBS. 20,000 cells of U2OS or the doubled number of HEK cells were grown on the 8-well imaging slides (either ibidi or Labtek) overnight. The slide has a bottom-glass (No. 1.5H, high precision) of 170 $\pm$5 nm glass thickness which is essential for superresolution imaging on the inverted microscope setup. Note that the HEK cells tend to easily detach from the glass surface, therefore the coating of 0.01% poly-L-lysine is additionally applied on the chamber slide and incubated for 30 min prior to cell seeding. For the visualization of fluorescent endotoxins, the cells were transfected with hCD14 plasmid (a kind gift of Prof. Dr. Rudi Beyaert, VIB, Gent) via CaCl2 precipitation or polyethylenimine methods.

For fluorescent LPS imaging, cells were treated with 1mg/mL of LPS-Alexa488 or 568 (Molecular Probes) in the growth medium at 48 hours post-transfection. LPS-Cy5 is gifted from Dr. Mojca Bencina (Chemistry institute, Slovenia). The hTLR4-Venus (a kind gift from Prof. Dr. Roman Jerala, Chemistry Institute, Slovenia) is used in cotransfection with CD14 plasmid. Dextran and Mitotracker (Molecular Probe) were used according to manufacture's instruction. The cells were fixed with 4% PFA after 5-30 min of fluorescent LPS incubation, followed by 3 rounds of PBS wash and kept in 4°C.

LOS imaging

Details of experiments conducted in the study using LOS-Cy7N can be found in [147].

Lipid A imaging

HEK-blue cells were kindly provided by Prof. Dr. Francesco Peri (University of Milano-Bicocca, Italy) and J774 macrophages were received from Dr. Juan Mwereque (BiomaGUNE, Spain). Cells were cultured in the same condition as previously described but without the plasmid transfection. The synthesis of LAMP and LADP, NBD conjugation and purification were all done in the collaboration with Prof. Dr. Antonio Molinaro (University of Naples Federico II, Italy). The

treatment of both fluorescent lipid A is followed the same procedures as the fluorescent LPS. All images were recorded in the same acquisition parameters as z stack image sets, deconvoluted and superimposed in maximal projection to reveal all the binding of different ligands in single cells. The range of image intensity was readjusted equally (gray value 77 to 1000) to minimize the biased presentation.

Inflammasome imaging

All the mouse bone marrow-derived macrophage (BMDM) cell lines used in the inflammasome study were obtained from Prof. Dr. Roman Jerala (Chemistry Institute, Slovenia), most of them were newly created by Petra Susjan. They were stable cell lines individually expressing the ASC^{FL}-GFP, ASC^{FL}-tagRFP, NLRP3-SkylanS, ASC^{FL}-GFP/NLRP3-tagRFP in WT or P3KO background, ASC^{PYD}-GFP. Note that the NLRP3 expression is engineered to be induced by doxycycline. Some of the cell lines were constructed directly from the wild-type BMDM cells by retrovirus transduction and examined their inflammatory cytokine secretion after several rounds of antibiotic selections. Single clones were also obtained by the limited dilution approach or by the cell sorting.

On the day of cell seeding, $1.5x10^5$ per well of the imaging slides were primed with 50ng/ml LPS overnight. 0.5μg/ml doxycylcine was additionally supplemented if the expression of inducible NLRP3 is required. The induction of inflammasome formation is triggered by 10 μM nigericin in HEPES buffer and then the cells were immediately brought onto the microscope stage for imaging. Cell pre-treatment with the caspase-1 inhibitor, 100 μM acYVAD, prior to nigericin induction is optionally performed in order to suppress the pyroptopic cell death if a prolonged observation is expected. A non-treatment of nigericin was also performed to assess the autoactivation of the macrophages and self-formation of the inflammasomes, which were normally examined in less than 1% of the total cell population.

PSF measurement in gel

0.1μm TetraSpeck microspheres (ThermoFisher)were embedded in 2% agarose in the imaging chamber, and then permeated with the clearing agent, SeeDB2S, using the published protocol in *Ke et al.*[61], but leave the gel with final SeeDB2S infiltration overnight. The PSF of beads were acquired in z volume (5-10 μm)

recorded by 642nm, which has deeper transmission into the gel with less scattering. Axial position of the bottom glass surface where many beads deposit is defined as 0 μm, and then use the Nanomover stage to find other beads in the positions away from the glass surface. The FWHM was determined by Gaussian fitting using Fiji plugin MetroloJ. Sample size was 10 in each group and plotted with standard deviation as error bars. The oil with RI of 1.520 is used for imaging with oil objective, whereas silicone oil (RI=1.40) and water (RI=1.33) were used for respective immersion objectives.

Optical clearing of mouse brain

Mouse brains were kindly provided by Prof. Dr. Christian Kaltschmidt, they were dissected by the certified technician and fixed with 4% PFA at room temperature. The clearing protocol of SeeDBS2 is used[60]. Briefly, one half of the fixed brain was incubated with 2% saponin in PBS. Afterwards the reagent was replaced subsequently with 18.5, 28.1, 56.2% (w/w) iohexol in the presence of 2% saponin. Finally, the tissue was incubated and kept with SeeDB2S (70.4% (w/w) iohexol in 10mM Tris-HCl (pH=7.6), 0.267mM EDTA). All incubation steps took overnights at room temperature.

Cryosection and tissue staining

The dissected mouse brain were immediately embedded in OCT held in a cryomold. Subsequently, the cryomold is submerged into isopentane acclimated with liquid nitrogen to form a freezing block. The cryosections were sliced in 20 μm from this block using a cyrostate (Leica Biosystems). The tissue sections collected on the glass slides were post-fixed by 4 %PFA for 30min, rinsed with PBS and air-dried before stored in the freezer. Immunostaining of the sectioned brain tissues was performed in the same procedures as mentioned in the cell staining of inflammasomes. The primary neurofilament M antibody (1:00) is kindly provided by Prof. Dr. Christian Kaltschmidt. After secondary antibody labeling (1:400), the tissues were stained briefly with 5 μg/ml Hoechst 33342 (Merck) for 5 min before they were mounted with Vectashield (Vectorlabs).

Antibody labeling of ASC specks for dSTORM imaging: All procedures are conducted in the imaging chambers. ASC^{FL}-GFP cells are first cultivated and

treated to form the specks as described above. They are fixed in 4% PFA and washed with PBS. The cells are then permeabilized with 0.5% Triton-X100 for 3 min and followed by PBS washing and blocking with 3% bovine serum albumin in PBS for 30 min. Immunolabeling of ASC specks is conducted with the mouse anti-ASC antibody (1:200, BioLegend, USA) for 2 hrs at room temperature and PBS washes. Afterward, the cells are stained with 1:400 Alexa 647-conjugated anti-mouse IgG secondary antibody for another 2 hrs, followed by PBS washes and kept in PBS before imaging. Post-fixation can be optionally applied after the antibody staining. Shortly before dSTORM measurement, the oxygen scavenger buffer (0.05 g/ml glucose, 0.06 M Tris pH=8, 0.06 M NaCl, 2.4 mM cyclo-octa-tetradene, 0.84 % (v/v)β-mercaptoethanol, 1.2 μg/mL catalase, 0.06 mg/mL glucose oxidase) is used to fill up the imaging well which is then sealed with a piece of glass lid.

Actomyosin imaging

The cell samples were directly received from Dr. Emma Lang and Dr. Stig Ove Boe (Oslo University Hospital). The preparation is described in the corresponding figure legends.

APPENDIX A. MATERIALS AND METHODS

Appendix B

Publication

1. **Tung-Cheng Wang**, Florent Cochet, Fabio Alessandro Facchini, Lenny Zaffaroni, Christelle Serba, Simon Pascal, Chantal Andraud, Flaviana Di Lorenzo, Olivier Maury, Thomas Huser, Francesco Peri. (2019) Synthesis of new cyanine-labeled bacterial lipooligosaccharides for intracellular imaging and in vitro microscopy studies. Bioconjugate Chemistry 30 (6): 1649-1657.

2. Loic Reymond, Johannes Ziegler, Christian Knapp, **Tung-Cheng Wang**, Thomas Huser, Verena Ruprecht, Stefan Wieser. (2019) SIMPLE: Structured illumination based point localization with enhanced precision. Optics Express 27 (17): 24578-24590.

Appendix C

Acknowledgment

Four years of my doctorate have been gone so fast, especially with so many helpers working closely every day that I would like here to express my gratitude to you all. Of course, the first is my doctor-father Prof. Dr. Thomas Huser, who granted me this once-in-a-lifetime opportunity to work and strengthen my techniques and knowledge on superresolution microscopy. This is a turning point of life to come to Germany for me and my family. You are always with a smile when I prompt you with questions on the doorway. I truly learned how to be soooooooo... way positive in any circumstances.

I also like to thank all colleagues in our working group. Dr. Wolfgang Huebner, thanks for your guidance on the OMX and the permission to use the luxurious yet imperfect imaging facility. We surely discussed more than just science and I'm very impressed by your never-ending knowledge of history, politics, culture and far more complaints!

My office roommates, Anders and Kati, are particularly mentioned here, who show the patience and tolerance when I talked in German, you two are more than just colleagues but true friends. I'd like to additionally thank Anders for the dSTORM measurement and alluring me to join the after-work activities and I do enjoy many nights of beer tasting and bouldering. To sweet Kati, we had countless conversations over the east-Asian culture, languages and stories of my personal experience. I learned as such as you did from me, hope it's useful for your brilliant

future.

Special thanks to Stefan Bergmann, Alice, Luis, Alex, Mario for sharing information during coffee breaks, and you guys also make me feel young again. Thanks to Christian and Henning that I received the warmest welcome upon arrival and useful consultant about plans of graduation. Big thanks to Reinhild who helped me not only on the documents but also sincere advice on children and career planning. Gerd, Stefan Woermer and Mark, thank you for professional support to my study.

Many thanks to Christian and Sherry for proof-read this dissertation and fruitful discussion. I thank Dr. Marcel Mueller and Andreas to improve my understanding of SIM as well.

Petra Susjan, thank you for your amazing support with cell culture and pushing me forward on imaging, the inflammasome study came late but it truly amazed us all. Look forward to seeing our publication someday.

I owe the biggest gratitude to my family, especially to my parents in Taiwan. My wife Sophie, our lovely and naughty daughter Lollo, who gives joy to my life every day. Thank you both for invaluable love and keeping me busy for survival!

Erklärung

Hier erkläre ich,

1. dass mir die geltende Promotionsordung der Fakultät für Physik bekannt ist,
2. dass ich die vorliegende Dissertation selbst angefertigt habe (Selbständigkeitserklärung), dabei keine Textabschnitte von Dritten oder eigener Prünfungsarbeiten ohne Kennzeichnung übernohmmen und alle benutzten Hilfsmittel und Quellen in der Arbeit angegeben habe,
3. dass Dritte weder unmittelbar noch mittelbar geldwerte Leistungen von mir für Vermittlungstätigkeiten oder für Arbeiten erhalten haben, die im Zusammenhang mit dem Zustandekommen oder dem Inhalt der Dissertation stehen und
4. dass ich die Dissertation oder wesentliche Teile davon nicht als Prüfungsarbeit für eine staatliche oder andere wissenschaftliche Prüfung eingereicht habe.

Bielefeld, den 13.03.2020